



# Caractérisation des processus élémentaires de croissance des cristaux de carbure de silicium non désorienté

Martin Seiss

## ► To cite this version:

Martin Seiss. Caractérisation des processus élémentaires de croissance des cristaux de carbure de silicium non désorienté. Autre. Université de Grenoble, 2013. Français. NNT : 2013GRENI046 . tel-00965640

**HAL Id: tel-00965640**

**<https://theses.hal.science/tel-00965640>**

Submitted on 25 Mar 2014

**HAL** is a multi-disciplinary open access archive for the deposit and dissemination of scientific research documents, whether they are published or not. The documents may come from teaching and research institutions in France or abroad, or from public or private research centers.

L'archive ouverte pluridisciplinaire **HAL**, est destinée au dépôt et à la diffusion de documents scientifiques de niveau recherche, publiés ou non, émanant des établissements d'enseignement et de recherche français ou étrangers, des laboratoires publics ou privés.

## THÈSE

Pour obtenir le grade de

## DOCTEUR DE L'UNIVERSITÉ DE GRENOBLE

Spécialité : **Matériaux, Mécanique, Génie civil, Electrochimie**

Arrêté ministériel : 7 août 2006

Présentée par

**Martin Seiss**

Thèse dirigée par **Thierry Ouisse**

préparée au sein **Laboratoire des Matériaux et du Génie Physique**  
et de **l'IMEP-2**

# Characterisation of the elementary growth processes of silicon carbide on-axis crystals

Thèse soutenue publiquement le **3 décembre 2013**,  
devant le jury composé de :

**Dominique Planson**

Professeur, INSA Lyon, Président

**Gabriel Ferro**

Directeur de recherche CNRS, UCB Lyon, Rapporteur

**Peder Bergman**

Professeur, IFM, Université de Linköping, Rapporteur

**Didier Chaussende**

CR1 CNRS, LMGP, Examineur

**Andreas Danilewsky**

Chercheur, Institut für Geowissenschaften, Université de Fribourg, Examineur

**Thierry Ouisse**

Professeur des Universités, LMGP, Directeur de thèse





Wolfgang Pauli

Das Volumen des Festkörpers wurde von Gott geschaffen,  
seine Oberfläche aber wurde vom Teufel gemacht.

God created the volume, whereas the surface was a work of the Devil.



# Remerciements

Ce travail de thèse a été réalisé au Laboratoire des Matériaux et du Génie Physique à Grenoble. Je remercie son directeur Bernard Chenevier pour m'avoir accueilli au sein du laboratoire.

Je tiens à remercier vivement mon directeur de thèse Thierry Ouisse. Son enthousiasme scientifique m'a inspiré et motivé pendant ces trois années. Merci beaucoup pour ta patience !

Un grand merci à Didier Chaussende pour les discussions utiles et les propositions constructives.

Je remercie Béatrice Doisneau qui m'a aidé au MEB et qui a effectué les observations MET.

Merci également à Odette Chaix pour l'introduction à la spectroscopie Raman et son aide.

Je remercie Etienne Pernot qui m'a montré la diffraction Laue et Hervé Roussel qui a effectué les caractérisations par diffraction des rayons X. Merci aussi à Patrick Chaudouet pour les mesures MEB au début de cette thèse. Je remercie Joseph La-Manna pour l'aide aux travaux mécaniques. Merci à Roland Madar, Marc Audier et Michel Boudard pour les discussions scientifiques.

Je remercie sincèrement Mélanie Lagrange pour la correction des chapitres en français et pour les pauses café amusantes. Merci également à Daniel Langley qui m'a aidé pour tout ce qui concerne l'anglais (malgré le fait qu'il ne parle que l'anglais australien). Merci à Elisabeth Payrer pour les bons moments !

Enfin, merci à tous ceux qui m'ont aidé autrement ou avec qui j'ai passé de bons moments : Julien Lefebure, Kanaparin Ariyawong, Sophie Guillemain, Pauline Serre, Renaud Viennet, Louis Fradetal, Ionela Iliesu et Lijie He.



# Contents

<b>Abbreviations and Symbols</b>	<b>v</b>
<b>Introduction</b>	<b>1</b>
<b>1 Fundamentals</b>	<b>5</b>
1.1 Introduction to SiC . . . . .	5
1.1.1 History of SiC . . . . .	5
1.1.2 Applications of SiC . . . . .	6
1.2 Polytypism and crystallography . . . . .	8
1.3 Defects . . . . .	12
1.3.1 Perfect dislocations . . . . .	13
1.3.2 Partial dislocations and stacking faults . . . . .	14
1.3.3 Micropipes . . . . .	16
1.4 Growth of SiC crystals . . . . .	18
1.4.1 Polytype growth conditions . . . . .	18
1.4.2 Physical vapour transport deposition . . . . .	20
1.4.3 The Burton Cabrera Frank theory . . . . .	21
<b>2 On-axis growth of SiC</b>	<b>31</b>
2.1 Experimental setup and growth conditions . . . . .	31
2.1.1 Growth reactor . . . . .	31
2.1.2 Seed preparation and growth conditions . . . . .	33
2.1.3 Sample Characterization . . . . .	35
2.2 Growth rate limiting step . . . . .	37
2.3 Nucleation . . . . .	40
2.3.1 Experimental details . . . . .	40
2.3.2 Observed Nuclei . . . . .	41
2.3.3 Nuclei distribution . . . . .	44
2.3.4 Estimating the diffusion length from the nuclei density . . . . .	47
2.4 Conclusion on the on-axis growth of SiC . . . . .	49



## Contents

<b>3</b>	<b>Spiral phenomena</b>	<b>51</b>
3.1	Observed spirals . . . . .	51
3.1.1	Spiral types . . . . .	51
3.1.2	The shape of the spirals . . . . .	59
3.2	Growth rate of micropipes . . . . .	65
3.3	Spiral growth modes . . . . .	68
3.3.1	Experimental details and analysis . . . . .	68
3.3.2	Results and discussion . . . . .	74
3.4	Spiral step dissociation . . . . .	85
3.4.1	Experimental . . . . .	86
3.4.2	Results . . . . .	86
3.4.3	Discussion . . . . .	90
3.5	Conclusion on the growth spirals . . . . .	99
	<b>Conclusion</b>	<b>103</b>
<b>A</b>	<b>Appendix</b>	<b>107</b>
A.	Differential interference contrast (DIC) microscopy . . . . .	107
B.	Atomic force microscopy (AFM) . . . . .	108
C.	Raman spectroscopy . . . . .	110
D.	Field emission gun scanning electron microscopy (FEG-SEM) . . . . .	112
E.	High resolution transmission electron microscopy (HRTEM) . . . . .	113
F.	X-ray diffraction . . . . .	115
G.	Laue diffraction . . . . .	116
	<b>Bibliography</b>	<b>119</b>
	<b>Résumé français</b>	<b>141</b>
	Introduction . . . . .	141
	Chapitre 1 . . . . .	144
	Chapitre 2 . . . . .	150
	Chapitre 3 . . . . .	153
	Conclusion . . . . .	158
	<b>Abstract</b>	<b>162</b>





# Abbreviations and Symbols

## Abbreviations

<b>AFM</b>	atomic force microscopy
<b>CVD</b>	chemical vapour deposition
<b>DIC</b>	differential interference contrast
<b>fcc</b>	face centred cubic
<b>GaN</b>	gallium nitride
<b>IGBT</b>	Insulated Gate Bipolar Transistor
<b>In<sub>x</sub>Ga<sub>1-x</sub>N</b>	indium gallium nitride
<b>JFET</b>	junction gate field-effect transistor
<b>KH<sub>2</sub>PO<sub>4</sub></b>	potassium dihydrogen phosphate (KDP)
<b>KOH</b>	potassium hydroxide
<b>LED</b>	light emitting diode
<b>MOSFET</b>	metal-oxide-semiconductor field-effect transistor
<b>PVT</b>	physical vapour transport deposition
<b>FEG-SEM</b>	field emission gun scanning electron microscopy
<b>FIB</b>	focused ion beam
<b>REM</b>	reflection electron microscopy
<b>SiC</b>	silicon carbide
<b>SOI</b>	silicon on insulator
<b>STM</b>	scanning tunnelling microscopy
<b>TEM</b>	transmission electron microscopy

## Latin symbols

$a$	first neighbour distance of atoms on a step
$\vec{b}$	Burgers vector
$c_c$	adatom concentration at the edge of a curved step
$c_{eq}$	equilibrium concentration at the edge
$c_m$	surface concentration caused by the vapour flux
$c_s$	concentration profile on terrace

$D$	diffusion coefficient
$D_{AB}$	diffusion coefficient of species A into B
$D_{BA}$	diffusion coefficient of species B into A
$E$	Young's modulus
$E_{el}$	elastic strain energy of a dislocation
$F_{net}$	net force between a micropipe and a dislocation
$\Delta H$	enthalpy of crystallization
$G$	shear modulus
$g(x)$	mean square displacement
$H_m$	Mohs hardness
$J_A$	flux of crystallizing species from powder
$j_{des}$	desorption flux
$j_{net}$	net flux of adatoms on terrace
$j_s$	surface diffusion flux
$j_v$	vapour flux
$k_B$	Boltzmann constant
$m$	mass
$n_s$	number of adatoms
$p$	pressure
$P$	perimeter
$p_A$	partial pressure of species A
$p_B$	partial pressure of species B
$p_\infty$	equilibrium vapour pressure
$R$	crystal growth rate
$R_m$	growth rate of a micropipe
$r_0$	tube radius of a micropipe
$T$	temperature
$T_m$	melting temperature
$u$	number of next neighbouring atoms in the crystal
$v$	advance rate of a step
$v_{adv}$	advective velocity
$w$	number of next neighbouring atoms on a growing face
$W_{int}$	elastic energy of a step
$x_0$	terrace width of a group of dislocations

## Greek symbols

$\alpha$	Jackson factor
$\tilde{\beta}$	step stiffness
$\epsilon$	strain
$\gamma$	surface energy
$\kappa$	specific edge energy
$\Lambda$	terrace width
$\lambda_s$	surface diffusion length
$\mu_s$	chemical potential of the solid phase
$\mu_v$	chemical potential of the vapour phase
$\Delta\mu$	difference in the chemical potential between vapour phase and crystal
$\nu$	Poisson ratio
$\rho$	radius of curvature
$\rho_c$	critical radius of a nucleus
$\sigma$	supersaturation
$\sigma_c$	characteristic supersaturation dividing parabolic from linear growth law
$\tau$	mean residence time on surface



# Introduction

Semiconductors are an integral component of many products in our daily life. Today's modern technology, such as computers and smartphones, would be unimaginable without powerful and highly developed chips all of which need semiconductors. Silicon is undisputed the leading semiconductor currently used. The advantage of silicon is, that its growth process and material characteristics are known in-depth. Another benefit of silicon is its abundance and that it has its own native insulator with truly exceptional properties (silicon dioxide). Furthermore, large wafers of high quality can be grown cost-efficiently. However, silicon is not the semiconductor of choice for all applications, in high temperature and high power electronics wide band gap semiconductors, such as silicon carbide (SiC), are needed.

Contrary to silicon, the growth of silicon carbide crystals with large diameter, low defect density and high crystalline quality is still a challenging subject. The hard to handle polytype stability should be mentioned in this context. Although there are, and there have been, great efforts and successes in improving the crystal growth process, *e.g.* the drastic reduction of micropipes [1], there is still little knowledge on the fundamental processes taking place during growth. Yet, these processes might be the key to growing good SiC crystals.

This thesis will shed some light on the fundamental mechanisms taking place in the initial growth of on-axis silicon carbide crystals from the vapour phase. The growth proceeds via the incorporation of adatoms on spirals covering the surface. F.C. Frank was the first who proposed the existence of spirals in 1949 in order to explain the unexpected high growth rate at low supersaturations [2]. Shortly afterwards, the presence of growth spirals was confirmed for several materials, including also SiC [3][4]. Burton, Frank and Cabrera were the first who described the spiral growth mathematically [5]. Their theory, nowadays usually called BCF theory, is still one of the most important works concerning the spiral growth. Nevertheless, there have been some refinements of the basic theory. Cabrera and Levine, for example, determined the terrace width on spirals more precisely than Burton, Cabrera and Frank [6]. Another refinement is the introduction of the back stress effect, which takes the overlap of diffusion fields into account [7].

After Frank published his ideas on growth spirals, the research on them was a really hot topic. The number of publications related to these growth spirals was



## Introduction

highest during the fifties of the twentieth century, with a continuous decrease afterwards. Currently, only few articles are published per year although there are still many open questions concerning the spiral growth. The invention of atomic force microscopy and scanning tunnelling microscopy in the eighties gave the opportunity to have new views on the surface structure of materials. Moreover, the increase of the computer performance in the last few decades allowed simulations even without a supercomputer. The combination of both, detailed surface characterization and simulations related to these experimental findings, offers a possibility to understand the fundamental processes on crystal surfaces during growth as it was for example done by Redinger *et al.* in the case of step edge barriers of spirals and mounds on Pt(111) surfaces [8]. Other authors focused either on simulations [9] or experimental work [10] on the spiral growth.

At the *Laboratoire des matériaux et génie physique* we are in the fortunate position, to grow and characterize our own crystals. In addition, with the simulation programs created in our laboratory, we are able to tackle the surface growth mechanism of SiC.

The structure of this thesis is as follows. In the first chapter, a short overview on the history and possible applications of SiC is given. Then, material related properties, such as polytypism and defects, are discussed. Moreover, the theory of Burton, Cabrera and Frank is introduced and the basic equations, necessary for the understanding of the following chapters, are derived. These equations relate the growth rate of the crystals as a function of the spiral terrace width and supersaturation.

The second chapter deals with the description of the experimental setup and preliminary experiments related to the on-axis growth of SiC, the crystal growth conditions and characterization procedures are also specified. The experimental results presented in this chapter are fundamental to the further spiral analysis in the next chapter. The limiting step of the crystal growth, which is either the vapour phase transport or processes on the crystal surface, is determined. Furthermore, the randomly occurring nucleation on the spiral terraces is studied.

The third chapter is dedicated to the spiral growth on SiC. The formation of spiral patterns on the surface is examined in the first section, followed by the discussion of the spiral shapes. The growth modes of single and double spirals are then analysed in detail. Spiral profiles from the samples are linked to simulations allowing thus conclusions on the growth mechanism. The variation of the terrace width with the growth rate, and hence supersaturation, is also studied in this context. This has never been done before on SiC and reveals interesting results. The final part of this chapter is about a novel spiral step structure. We will show

that spiral steps can dissociate under specific growth conditions. The possible origin of the dissociation is discussed.

Finally, a conclusion summarizes the results of this thesis. Furthermore, some propositions on further work are given.



# 1 Fundamentals

In this chapter the history of silicon carbide (SiC) and its applications are presented briefly. Then the crystallographic properties and the most important defects related to this thesis are discussed. Finally, the growth process of SiC crystals is described. The main equations necessary for the discussion of the experimental results are also derived in this last section.

## 1.1 Introduction to SiC

### 1.1.1 History of SiC

Silicon carbide was first described in 1824 by Jöns Jacob Berzelius. He was probably the first person who synthesized SiC and who proposed the existence of bonds between silicon and carbon [11]. On earth, SiC very rarely occurs in nature and is only found in meteorites - which explains its late discovery. The first SiC crystals in nature were found by Henri Moissan in a meteorite in 1905 [12]. Therefore natural SiC is also called *Moissanite*.

Edward Goodrich Acheson was the first to succeed in synthesizing SiC in a large quantity (1890) [13]. He developed a process, called the Acheson process, in which a mixture of carbon (coke) and silica or quartz sand is heated above 2000 °C in an electric furnace. Small SiC crystals are obtained by this method. In fact, Acheson first believed that he had synthesized a new compound based on carbon and aluminium as he used aluminium silicate as source material. Therefore he called the obtained crystals *Carborundum*, named after Corundum ( $\text{Al}_2\text{O}_3$ ) and carbon. The term Carborundum is still sometimes used today.

The interest in electronic applications of SiC arose in 1907 as H.J. Round noticed that light was emitted by a SiC crystal when he applied 10 V to it [14]. Actually, Round had made the first light emitting diode (LED). H. Baumhauer discovered in 1912 that SiC exists in many different structures and introduced the term polytypism for this phenomenon [15]. In 1949 F.C. Frank proposed the spiral mechanism of crystal growth at low supersaturations [2] and it was shown shortly after by S. Amelinckx [4] and A.R. Verma [3] that crystal growth on on-axis  $\alpha$ -SiC

## 1 Fundamentals

proceeds by this mechanism.

Due to its high hardness of  $H_M = 9.08$  (Mohs hardness scale, for comparison diamond has a  $H_M = 10$ ) [16], SiC was used as abrasive from its discovery on. SiC was not interesting as a semiconductor because of its low crystalline quality until the middle of the 20th century. Then, J.A. Lely succeeded in growing SiC crystals from the vapour phase (1955) [17]. The development of this technique was a milestone in SiC growth and it is still used in a modified way to grow SiC crystals with very low defect densities. Therefore it is referred to as the Lely method. However, it is not suitable for industrial production due to a low yield ( $\approx 3\%$ ) [18]. As the interest in SiC rose, the first conference on SiC was held in Boston 1958.

Tairov and Tsetkov developed the seeded sublimation growth technique, also known as modified Lely method, in 1978 [19]. Due to the high yield of this method ( $\approx 90\%$ ), it is now the industry standard for growing SiC crystals [18].

In 1989 the Cree company brought the first commercial blue LED on the market - two years after Cree was founded [20]. Cree is also one of the most important manufacturer of SiC wafers. The availability of SiC wafers extended the research efforts and industrial applications. While many SiC devices were demonstrated in research during the last 20 years, e.g. different types of diodes and transistors [21], the only available SiC devices on the market today are the Schottky diode and MOSFET [22][23][20].

### 1.1.2 Applications of SiC

There are many different applications of silicon carbide: as an abrasive, ceramic plates in bulletproof vests, brake discs in cars, jewellery and last but not least electronic circuit elements. Here, the focus is on the latter, the use as an electronic device. The reference material for all semiconductors is silicon as it is the basis of almost all semiconductor devices and therefore it is compared with SiC below.

The availability of silicon as well as the research efforts and successes of this material led to its widespread use in semiconductor industries. However, there are some cases in which materials with different properties are desired and this is where SiC comes into play. The wide band gap of SiC makes it a promising material for high temperature semiconductors. In literature [21] the definition of high temperature is  $\approx 150^\circ\text{C}$ , the upper limit at which standard silicon devices still work properly. Advanced technologies, such as silicon on insulator (SOI), make temperatures up to  $300^\circ\text{C}$  possible for silicon based devices [24]. With increasing temperature the number of thermally generated carriers in a semiconductor rises which in turn degrade the semiconducting properties. Fig. 1.1 shows the intrinsic carrier concentration for several semiconductors. At  $300^\circ\text{C}$  this concentration is

more than ten orders of magnitude larger for silicon compared to 6H silicon carbide. Currently, gallium nitride (GaN) is the most important competitor of SiC in the field of high-temperature applications, but GaN crystals contain even more defects than SiC [21].

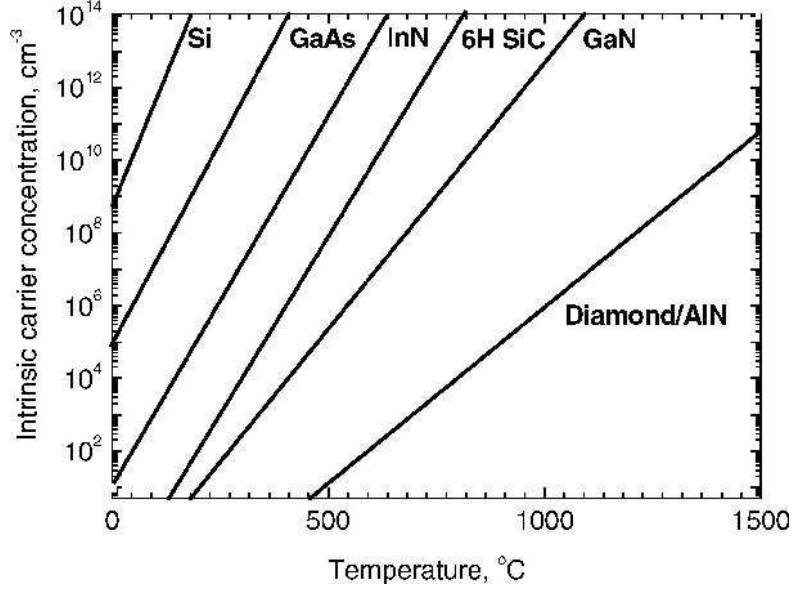


**Figure 1.1:** Intrinsic carrier concentration as function of temperature of several semiconductors. Image taken from [25].

Due to its physical properties (see Tab. 1.1), SiC is a promising material for high temperature, power and frequency applications. Yet, there are currently not many SiC based devices available. One of these devices is the Schottky diode which can withstand reverse voltages above 200 V. Other available SiC devices are metal-oxide-semiconductor field-effect transistor (MOSFET) and junction gate field-effect transistor (JFET). The device characteristics are very similar and the main difference in design is that the MOSFET has an insulating oxide between gate and channel. While Cree is producing SiC MOSFETs, Infineon focuses on JFETs as they are expecting a higher failure risk for MOSFETs due to the additional oxide layer [26]. Cree is also manufacturing LEDs based on SiC. Since SiC has an indirect band gap, a pure SiC LED is not favourable. Other materials with direct band gap and thus brighter emission, such as GaN and indium gallium nitride ( $\text{In}_x\text{Ga}_{1-x}\text{N}$ ), are preferred for this application. However, there are currently no GaN wafers available and therefore SiC wafers are used as substrates due to the similar lattice constants.

**Table 1.1:** Electrical properties of certain SiC polytypes [16][27][28].

	Si	GaN	3C SiC	4H SiC	6H SiC
band gap at 300 K [eV]	1.11	3.4	2.3	3.2	3
breakdown field [MV/cm]	0.25	3.3	2.12	2.2	2.5
saturated electron drift velocity [ $10^7$ cm/s]	1	2.7	2.5	2	2
electron mobility at 300 K [ $\text{cm}^2/\text{Vs}$ ]	1100	900	750	800	370
hole mobility at 300 K [ $\text{cm}^2/\text{Vs}$ ]	480	—	40	115	90
thermal conductivity [W/cm K]	1.5	1.3	5	4.9	4.9

## 1.2 Polytypism and crystallography

The basic unit of all SiC crystals is a tetrahedron consisting of either  $\text{SiC}_4$  or  $\text{CSi}_4$  (there is no difference between these two configurations when considering the full lattice). Fig. 1.2(a) shows such a tetrahedron and also the same tetrahedron turned by  $60^\circ$  (Fig. 1.2(b)). Although it seems that there is no big difference between these two tetrahedrons at first sight, these two configurations have an enormous effect on the crystalline structure. Comparing the position of the central atoms in both tetrahedrons one can notice that in case (a) the central atom is rather on the left while it is rather on the right in case (b). The perpendicular bondings of the central atoms are thus pointing towards two different atomic sites in the crystal. Stacking these tetrahedrons in a certain repeating sequence results in different crystal structures. Baumhauer was the first who described this phenomenon and introduced the term polytypism [15].

The tetrahedrons are stacked in the c-direction of the crystal. This results in an alternating sequence of silicon and carbon layers. The succeeding stacking of one silicon and one carbon layer is referred to as a bilayer. Polytypes are defined by the periodic stacking of these bilayers and accordingly the orientation of the tetrahedrons. A tetrahedron always shares its corners with other tetrahedrons restricting thus the possibilities for stacking. A common way to illustrate the stacking of the different polytypes is shown in Fig. 1.3 where the atoms on the (110) plane (hexagonal:  $(11\bar{2}0)$ ) are regarded. In principle, there are three possible positions for the atoms in the lattice: A, B and C. Due to the corner sharing of the tetrahedrons it is not possible that two bilayers with atoms on the same lattice position are stacked (e.g. first and second bilayer on A position). The 3C SiC, also  $\beta$ -SiC, is the simplest polytype as there is only one type of tetrahedron (Fig. 1.3). For the other polytypes a zigzag structure is visible that is related to the rotation of the tetrahedrons (illustrated in Fig. 1.2(c)).

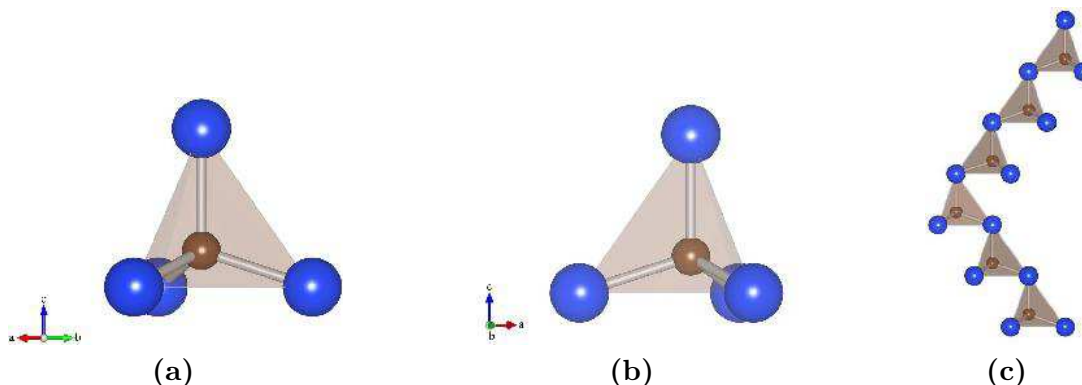


**Figure 1.2:** Illustration of a SiC tetrahedron (a). The carbon atom (brown) is coordinated with four silicon atoms (blue). Turning the tetrahedron by  $60^\circ$  (b) results in a different orientation that make the occurrence of different stacking in the crystal possible as illustrated in (c) for 6H SiC.

Due to the large number of SiC polytypes a notation is necessary to differentiate between them. However, since the discovery of the polytypism of SiC many notations have been proposed [16]. Here, the most important notations are presented. The most popular one is the Ramsdell notation. It consists of a number in the beginning that corresponds to the number of bilayers in a unit cell, followed by the letter H, C or R. H indicates that the lattice symmetry is hexagonal, C cubic and R rhombohedral. So 6H, for instance, means that there are six bilayers and the symmetry is hexagonal. Another possibility to describe the polytypes is the ABC notation. As previously mentioned, the letters A, B and C are related to atomic positions in the crystal lattice. In order to determine the ABC notation, one has to look at the stacking in the  $(11\bar{2}0)$  plane as illustrated in Fig. 1.3. The atomic positions of the bilayers in a unit cell then give the name. For example, 6H corresponds to ABC ACB. In some publications also the position of the carbon atoms are added in this notation. The carbon layer below the silicon A position is called  $\alpha$ , below B  $\beta$  and below C  $\gamma$ . Consequently, 6H e.g. would be noted as  $A\beta B\gamma C\alpha A\gamma C\beta B\alpha$  [29].

The use of the Jagodzinski notation is less common. The relative stacking of two succeeding bilayers is compared and if the stacking continues in the same direction the first bilayer is called c, that is derived from cubic. Otherwise, i.e. the stacking direction changes, h for hexagonal is used. Brackets around a stacking sequence followed by a subscripted number indicate a repeating sequence in an unit cell. For 6H e.g. it follows the notation  $(hcc)_2$  (Fig. 1.3). All notations presented here are summarized for the most common polytypes in Tab. 1.2.



## 1 Fundamentals

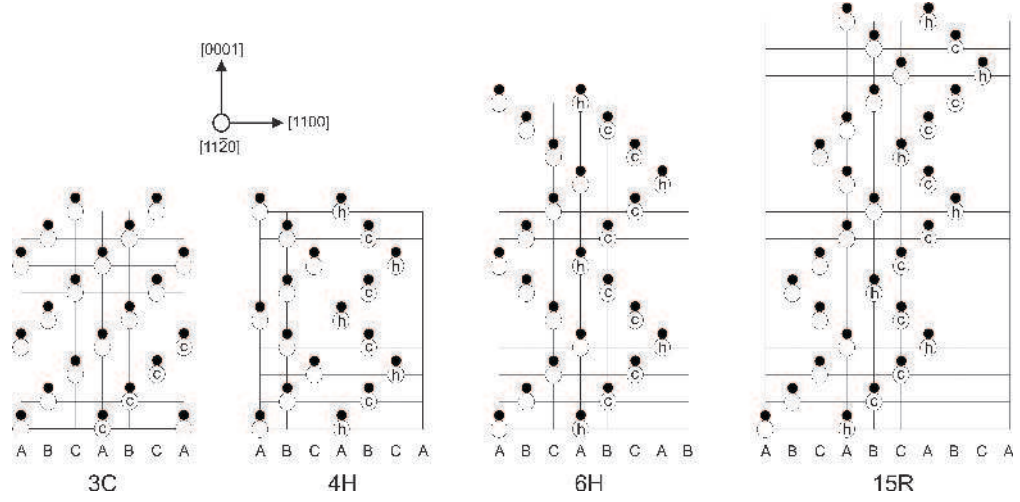


**Figure 1.3:** Stackings of the most widespread polytypes of SiC. The white circles correspond to silicon and the black filled circles to carbon atoms.

**Table 1.2:** Most common notations for certain SiC polytypes.

Ramsdell	ABC short	ABC long	Jagodzinski
3C	ABC	$A\beta B\gamma C\alpha$	c
4H	AB CB	$A\beta B\gamma C\beta B\alpha$	$(hc)_2$
6H	ABC ACB	$A\beta B\gamma C\alpha A\gamma C\beta B\alpha$	$(hcc)_2$
15R	ABCAC BCABA CABCB	$A\beta B\gamma C\alpha A\gamma C\beta B\gamma C\alpha A\beta B\alpha A\gamma C\alpha A\beta B\gamma C\beta B$	$(hcchc)_3$

The stacking of the atoms can actually be observed by transmission electron microscopy (TEM). Fig. 1.4 shows an image taken by TEM of the 15R polytype. The contrast difference is caused by the different orientation of the tetrahedrons and thus the typical zigzag-structure of SiC can be seen.

It is evident that the polytypism also affects the electronic and crystallographic structure of SiC. The smallest indirect band-gap varies from 2.3 eV (3C) to 3.2 eV (4H), while the direct band-gaps are much larger, e.g. 6.0 eV for 3C and 4.6 eV for 6H SiC [16]. Further electronic properties are listed in Tab. 1.1. Due to the different stackings the unit cell is also different for each polytype. The crystal system is either cubic, hexagonal or rhombohedral. Lattice parameters and space group for the here discussed polytypes are summarized in Tab. 1.3.

The difference in electronegativity of silicon (1.90 eV) and carbon (2.55 eV) induces polarity into SiC crystals. It follows that the  $\{0001\}$  planes are polar as they are either terminated by silicon ( $(0001)$  plane) or carbon atoms ( $(000\bar{1})$  plane)

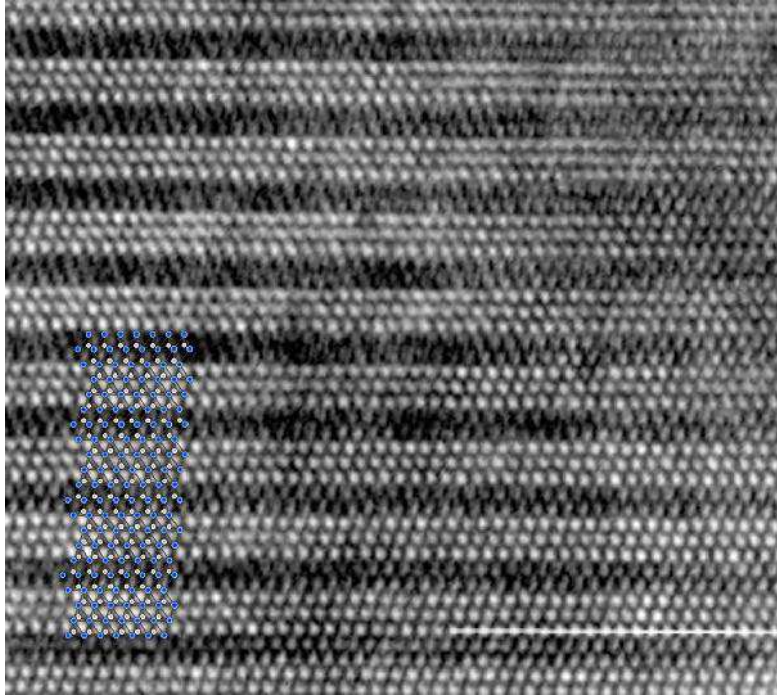


**Figure 1.4:** The stacking of the 15R polytype observed by TEM. The circles on the left illustrate the stacking of the tetrahedrons.

as illustrated in Fig. 1.5. On-axis, i.e. oriented along the c-axis, crystal surfaces are therefore further specified by Si-face (silicon terminated surface) or C-face (carbon terminated surface). Pearson *et al.* calculated the surface energies for 3C SiC and they found  $\gamma = 2.2 \text{ J/m}^2$  for Si-face and  $0.3 \text{ J/m}^2$  for C-face [30]. This energy difference has a strong effect on the crystal growth as it will be shown later.

The faces of a crystal can be determined for example by potassium hydroxide (KOH) etching [31]. Due to the differing surface energies, the etch rate is higher on a C-face than on a Si-face resulting in etch pits only on the latter.

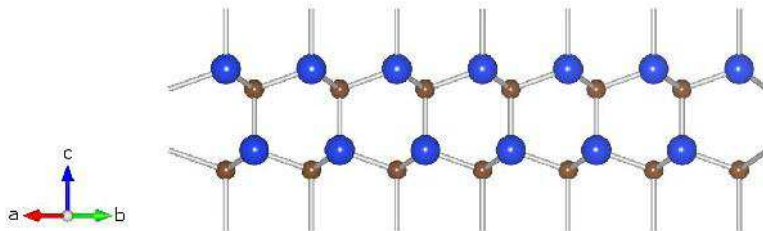


**Figure 1.5:** The surfaces of on-axis SiC crystals are either silicon (blue spheres) or carbon (brown spheres) terminated thus inducing polarity to the crystal. The silicon face is the  $(0001)$  plane and the carbon face the  $(000\bar{1})$  plane.

**Table 1.3:** Crystallographic properties of certain SiC polytypes [16].

polytype	c [ $\text{\AA}$ ]	a [ $\text{\AA}$ ]	space group
3C	—	4.36	$F\bar{4}m$
4H	10.08	3.08	$P6_3mc$
6H	15.12	3.08	$P6_3mc$
15R	37.80	3.08	$R3m$

### 1.3 Defects

Crystals are never perfect, neither those grown in nature nor those grown in laboratories. In SiC many different defects are observed and it is still a key problem to reduce the number of defects in order to obtain high quality wafers for industrial applications. As there is in general a large variety of defects, they are usually classified according to their dimensionality in 0D, 1D, 2D and 3D. Point defects, such as vacancies or (self-)interstitials, are 0D (zero dimensional) defects since they only affect a point in the crystal lattice. Dislocations are linear defects (1D) and may propagate through the whole crystal. Stacking faults, inversion domain boundaries, twins and many other defects belong to the planar (2D) defects category. The last group of defects contains those that affect a volumetric zone in the crystal, e.g. inclusions. Fig. 1.6 shows an overview of typical defects in a simple cubic crystal. In the following the focus is on defects relevant for this work.

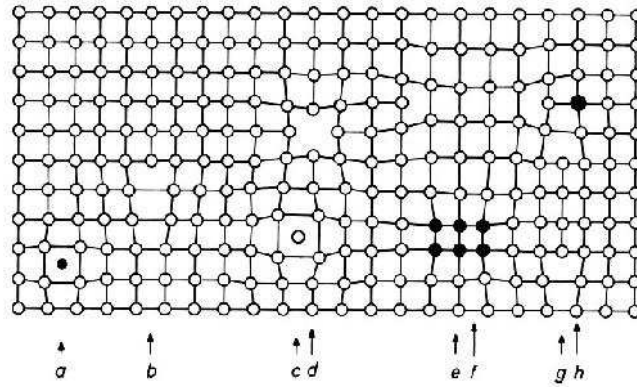


**Figure 1.6:** Typical defects in crystals: a) interstitial impurity atom, b) edge dislocation, c) self interstitial atom, d) vacancy, e) precipitate of impurity atoms, f) vacancy type of dislocation loop, g) interstitial type dislocation loop, h) substitutional impurity atom. Image taken from [32].

### 1.3.1 Perfect dislocations

In 1926 Frenkel introduced an equation to calculate the critical shear stress in a crystal, i.e. the force necessary to plastically deform a crystal. In order to derive this equation he supposed two rows of atoms that glide in opposite directions due to shear stress. However, in experiments the observed values of the critical shear stress were many orders of magnitudes lower. This difference was attributed to the presence of dislocations in 1934 independently by Orowan, Polanyi and Taylor [33].

There are three types of dislocations:

- edge dislocations
- screw dislocations
- mixed dislocations

If a half-plane of atoms is introduced in or removed from a perfect crystal, an **edge dislocation** is created (Fig. 1.7 (a) and (b)). Adding an extra half-plane in ABCD results in a disturbance of nearby planes in the crystal for the most part along the DC line.

Any type of dislocation can be described by its dislocation line and Burgers vector. In the case of the edge dislocation the end of the extra half-plane is the dislocation line. The Burgers vector  $\vec{b}$  defines the magnitude and direction of the lattice distortion caused by the dislocation. The most likely Burgers vector is the shortest lattice vector in a crystal. Fig. 1.8(a) and (b) show how the Burgers vector of an edge dislocation can be determined. In the plane perpendicular to the line of the edge dislocation a circuit is done around the centre; in the given example this is the circuit MNOPQ. The Burgers circuit is always performed clockwise when looking on the dislocation line. Performing the same circuit in a perfect crystal reveals that point M and Q are not at the same crystal position as for the crystal containing a dislocation. The Burgers vector is thus defined by the vector from Q to M. This vector is always perpendicular to the dislocation line for edge dislocations.

A **screw dislocation** can be illustrated by the slip of one part of a perfect crystal as shown in Fig. 1.7(c). Looking, as for the edge dislocation, along the dislocation line and performing the Burgers circuit round the screw dislocation and again the same circuit in a perfect crystal reveals the Burgers vector. In the given example in Fig. 1.8(c) and (d) the Burgers vector points again from Q to M but it is parallel to the dislocation line, as it is always the case for a screw dislocation.

**Mixed dislocations** have both an edge and screw component.

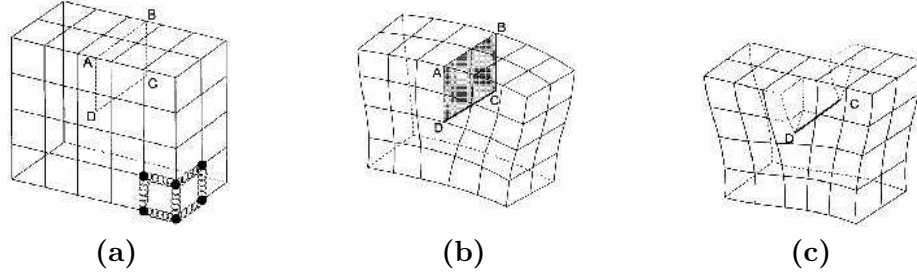


**Figure 1.7:** Visualisation of dislocations. (a) A perfect simple cubic crystal. In the lower right atoms are represented by black filled circles and the bondings between them by springs. (b) Introducing a half-plane in ABCD results in an edge dislocation. (c) A partial slip of the crystal creates a screw dislocation. Image taken from [33].

### 1.3.2 Partial dislocations and stacking faults

Partial dislocations possess a Burgers vector smaller than the shortest lattice vector and thus the motion of such a dislocation always leaves an imperfect crystal behind. The most known partial dislocations are the Frank and the Shockley partial dislocations. In literature they are often referred to as a Frank and Shockley partial.

The Frank partial is formed if a close packed  $\{111\}$  layer is inserted in or removed from a face centred cubic (fcc) crystal, as illustrated in Fig. 1.9. It is an edge dislocation that is *sessile*, meaning that the dislocation only propagates if stress is applied or if the temperature is high enough for climbing.

The Shockley partial is of more interest for SiC as it is the most common type of partial dislocation observed in this material. Fig. 1.10 illustrates the slipping process in a fcc crystal. If an atom slips from one B to another B position it is energetically more favourable to slip first to a C position than slipping directly to B. This can be proven by Frank's rule. The elastic strain energy of a dislocation can be approximated by [33]

$$E_{el} = \alpha G b^2 \quad (1.1)$$

where  $\alpha \approx 0.5 - 1.0$ ,  $G$  is the shear modulus and  $b$  the magnitude of the Burgers vector. Consequently, the elastic strain energy is directly proportional to the square magnitude of the Burgers vector. According to Frank's rule, a dislocation will decompose into two dislocations if [33]

$$(b_2^2 + b_3^2) < b_1^2.$$

Applying Frank's rule to Fig. 1.10 it follows that the creation of two Shockley partials of the type  $\vec{b} = 1/6\langle 121 \rangle$  is more favourable than one perfect dislocation

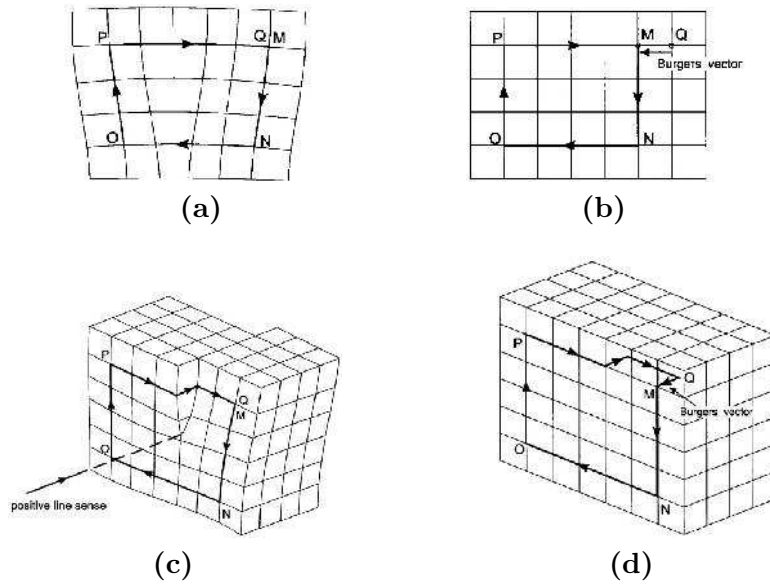


**Figure 1.8:** How to determine the Burgers vector for edge and screw dislocations. (a) Burgers circuit round an edge dislocation. (b) Same circuit in a perfect crystal. The difference in the path of both circuits gives the Burgers vector. (c) Burgers circuit round a screw dislocation and (d) same circuit in a perfect crystal. The path between start and end defines the vector. Image taken from [33].

with  $\vec{b} = 1/2\langle 110 \rangle^1$ . Contrary to Frank partials, Shockley partials are *glissile* as they can slip easily.

Dislocations with the same sign repel each other in order to reduce their total

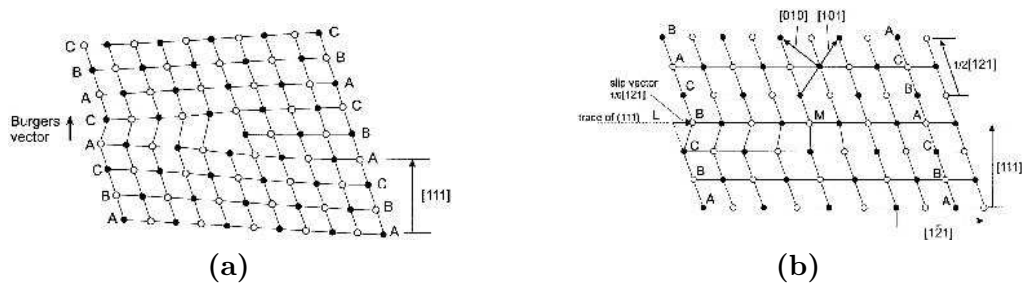


**Figure 1.9:** (a) Removing (partially) a close packed layer in a fcc crystal results here in the formation of  $\frac{1}{3}[111]$  Frank partial dislocation. (b) The slip of A atoms to B positions on the line LM creates a Shockley partial dislocation with  $\vec{b} = 1/6[1\bar{2}1]$ . Image taken from [33].

<sup>1</sup>Can be shown by entering the vectors in Franks rule:  $2a^2/36(1^2+1^2+2^2) < a^2/4(1^2+1^2+0)$

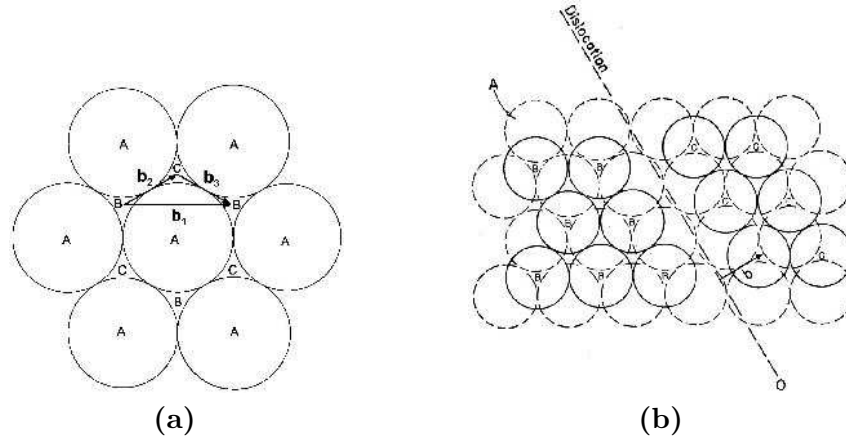


**Figure 1.10:** The images show the (111) plane of a fcc crystal. (a) A Shockley partial can be created if a (111) plane partially slips e.g. from a B to C position. (b) Illustration of a stacking fault caused by a Shockley partial. Images taken from [33] and [34].

elastic energy. Shockley partials also repel each other, creating thus a faulted region in-between them. Due to the deviation from the perfect crystal stacking in this region the crystal energy is increased by the stacking fault energy. The equilibrium of stacking fault energy and elastic interaction of the partials determines the size of the faulted region.

### 1.3.3 Micropipes

Micropipes are screw dislocations with a large Burgers vector and an empty core. This empty core forms if [35]

$$|\vec{b}| > 40\pi\gamma/G \quad (1.2)$$

where  $|\vec{b}|$  is the magnitude of the burgers vector,  $\gamma$  the surface energy inside the tube and  $G$  the shear modulus. In the case of SiC it follows that  $b > 1.7 \text{ nm}$  for  $\gamma_{Si} = 2.2 \text{ J/m}^2$  [30]<sup>1</sup> and  $G = 160 \text{ GPa}$  [36]. Assuming that  $|\vec{b}| = n \cdot c$ , where  $n$  is a positive integer and  $c$  the lattice constant, it follows that the core of a dislocation in 6H SiC is closed if  $|\vec{b}| = 1.5 \text{ nm}$ , that is an elementary dislocation ( $n = 1$ ), and open if  $|\vec{b}| \geq 3 \text{ nm}$ .

The large Burgers vector of micropipes entails a high strain energy especially in the core. This strain energy is reduced by diffusion or sublimation of atoms along

<sup>1</sup>Here, the surface energy of the tube is approximated by the surface energy of the (111) Si-face surface energy.

the core of the dislocation where the strain energy is largest. The tube radius  $r_0$  of a micropipe can be calculated by [35]

$$r_0 = Gb^2/8\pi^2\gamma \quad (1.3)$$

Consequently, the larger the Burgers vector the larger the radius of the core will be. Fig. 1.11 shows a micropipe observed by atomic force microscopy (AFM) on a C-face 6H SiC sample. The core radius of this micropipe is 370 nm. Using the previous equation, it follows that the c-component magnitude of the Burgers vector is 7.4 nm (assuming that  $G=160$  GPa [36] and  $\gamma_C=0.3$  J/m<sup>2</sup> [30]). The magnitude can be verified by counting the number of branches around the core and measuring their step height (that is the same for all branches). Ten branches can be observed and their step height is 0.75 nm (half the c lattice constant of 6H SiC). The c-component of a micropipe must always be an integer multiple of the c lattice constant. Thus it follows that the magnitude of the c-component is  $(2 \cdot 0.75 \text{ nm}) \cdot 5 = 7.5 \text{ nm}$ , that is the same as for the calculated value.

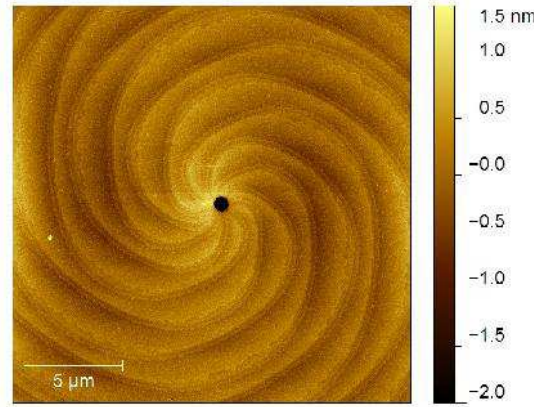


**Figure 1.11:** Micropipe observed by AFM. The radius of the core is 370 nm.

For application of SiC in semiconductor industries it is of utmost importance to reduce the micropipe density in substrates. Micropipes were found to drastically reduce the breakdown voltage of SiC pn-junctions [37]. There was enormous progress in the reduction of micropipes in SiC wafers in the last two decades as shown in Fig. 1.12 and nowadays micropipes are no longer a major issue in SiC growth.



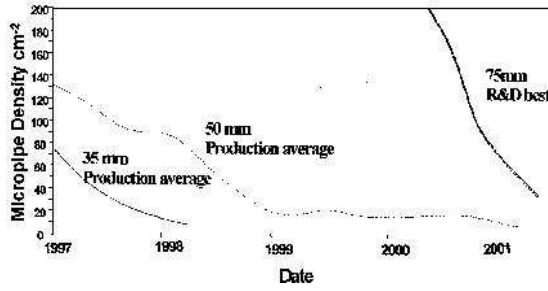


**Figure 1.12:** Evolution of the micropipe density of Cree wafers. Image taken from [38].

## 1.4 Growth of SiC crystals

### 1.4.1 Polytype growth conditions

The main challenge for the growth of SiC crystals is that the stoichiometric compound does not melt. From the phase diagram in Fig. 1.13 it is evident that SiC decomposes at 2680 °C directly into vapour and graphite. It is worth noting that this temperature is higher in other publications, e.g. 2800 °C in [39]. Also the phase diagrams in other publications, *e.g.* [40], are not identical above  $\approx 2000$  °C to the one shown here. Nevertheless, there is a small non-stoichiometric region, that is similar in all publications, where a liquid of Si and C can be obtained. It is indeed possible to grow SiC crystals in this region, yet this is a challenging subject. The difficulty of handling the liquid at this temperature due to the corrosive silicon melt and the morphological instabilities formed during growth have to be mentioned in this context [41].

Hence, it is clear why the growth from the vapour phase is the most widespread growth process for SiC. From the phase diagram the necessary growth conditions of the different polytypes cannot be deduced. The diagrams of Knippenberg and Inomata shown in Fig. 1.14 might be helpful in this case, as they indicate in which temperature ranges the different polytypes occur. Both authors agree that at elevated temperatures, i.e. 1800 °C and 1600 °C respectively, hexagonal and rhombohedral phases can be formed. However, according to Knippenberg 3C SiC grows at non-equilibrium conditions, whereas Inomata makes no special remarks about this polytype. In the latter diagram, two dashed lines are visible. They indicate the boundaries between 15R and 6H. The left dashed line was obtained by growth from the liquid phase whereas the right line is derived from sublimation growth. The region *L.P* denotes to long stacking sequence polytypes. Unfortunately the original publications of both diagrams lack important information, such as number of samples analysed and growth method. Nonetheless, these diagrams

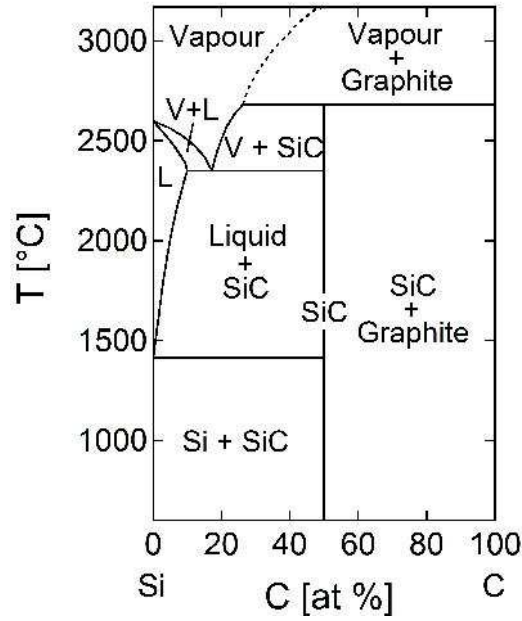


**Figure 1.13:** Phase diagram of SiC at atmospheric pressure. V denotes vapour and L liquid. Retraced image from [42].

might be used as starting point for the SiC growth but one has to keep in mind that the growth of the different polytypes is influenced by many other parameters besides temperature, for example seed polarity and polytype [43], supersaturation [44] and impurities [45].

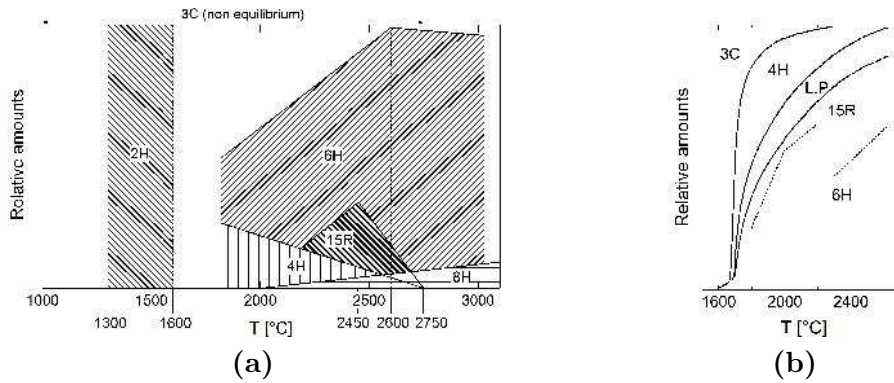


**Figure 1.14:** Two diagrams showing temperature ranges for growing different polytypes. Both authors agree that the hexagonal and rhombohedral polytypes occur mixed. But in (a) 3C is formed in non-equilibrium conditions contrary to (b) where nothing is remarked in addition. Images retraced from [46] and [47].

### 1.4.2 Physical vapour transport deposition

The modified Lely method is the most widespread technique for growing bulk SiC crystals. In the original growth method developed by Lely [17], SiC lumps are stuffed between two concentric graphite tubes. Then the inner tube is removed and a porous layer of SiC remains on the inner wall of the second tube. After closing the tube with a graphite cover, the crucible is heated up to  $\approx 2500^\circ\text{C}$  in argon atmosphere. The SiC powder that is in direct contact to the inner wall sublimates and nucleation starts on the inner surface of the powder where the temperature is lower (Fig. 1.15(a)). By this method small platelets with a thickness of a few millimetres and a diameter of about 1 cm can be obtained [27]. The quality of these platelets is high, i.e. low defect density and high polytype purity. This method is difficult to handle as the powder can easily crumble if the crucible is not inserted carefully into the oven or during heating due to thermal expansion. This could be avoided by introducing a porous graphite cylinder and filling the SiC lumps between this cylinder and the crucible. But a major problem remains: there is no focused growth as the nucleation occurs randomly.

Although there were some improvements of the Lely method, the actual breakthrough of the sublimation growth came with the modified Lely method by Tairov and Tsvetkov [19] and its further improvement. In literature this method is also called seeded sublimation growth technique or more commonly physical vapour transport deposition (PVT). The design of the growth furnace is similar to the Lely method. The polycrystalline SiC source is in-between the graphite crucible and porous graphite cylinder and the seed is attached to the lid of the crucible (inside the porous cylinder). Due to a temperature gradient between the bottom (high temperature) and the top (low temperature) as illustrated in Fig. 1.15(c), the SiC vapour is diffusing to and depositing on the seed on the lid. Parasitic nucleation on the porous graphite cylinder is thus suppressed. This technique was further improved and nowadays the geometry shown in Fig. 1.15(b) is principally used. The powder source is at the bottom of the crucible while the seed is attached to the lid. Typically, SiC growth is performed in argon environment with a pressure of  $10^{-4}$  to 1 bar and temperature in the range of 1800 to  $2600^\circ\text{C}$  [27]. The polytype can be, to a certain extent, controlled by the seed (polytype and polarity) and the temperature.

During the growth process the SiC powder is sublimating. Diffusion, due to the temperature gradient, and advection cause the transport of the gaseous species (Si, SiC,  $\text{SiC}_2$ ,...) towards the seed. Then the absorbed species are incorporated into the crystal resulting in the growth of the crystal. We will see that the growth rate is determined by the temperature gradient between source and seed, pressure and

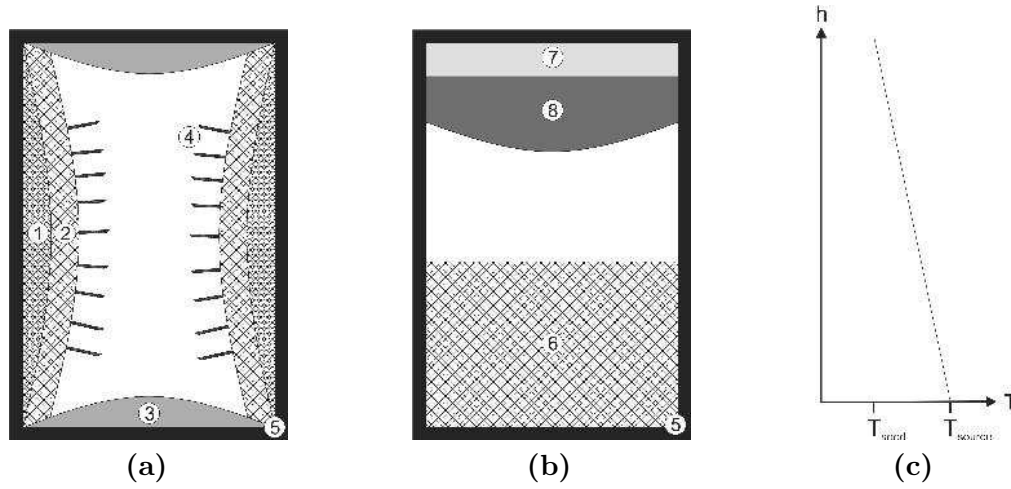


**Figure 1.15:** (a) The original Lely method and (b) the modified Lely method or physical vapour transport (PVT) technique: (1) carbon from decomposed SiC, (2) SiC lumps, (3) deposited SiC on graphite walls, (4) SiC platelets, (5) graphite crucible, (6) powder source, (7) seed, (8) grown crystal. (c) Temperature gradient of the PVT technique. Images redrawn from [27] [18] [19].

the seed to source distance .

### 1.4.3 The Burton Cabrera Frank theory

In 1949 Frank [2] proposed that crystal growth can proceed by a spiral mechanism. Up to that time it was assumed that 2D nucleation is necessary to grow crystals. Frank noticed that the growth rate is much higher below the critical supersaturation for 2D nucleation than expected and attributed this to the presence of screw dislocations. At the emergence point on the crystal surface a step with kink sites is created. This step winds up around the core forming thus a growth spiral as shown in Fig. 1.16.

Two years later Burton, Cabrera and Frank showed theoretically how the growth rate and terrace width of growth spirals can be derived [5]. This is now known as BCF theory. In the following a simplified approach is used to derive the basic equations. For simplicity it is assumed that the adatom incorporation into the edge is not limiting the crystal growth and that there is no Ehrlich-Schwoebel effect. The interested reader is referred to the textbook of Markov [48] for a full derivation of the BCF theory.

## 1 Fundamentals

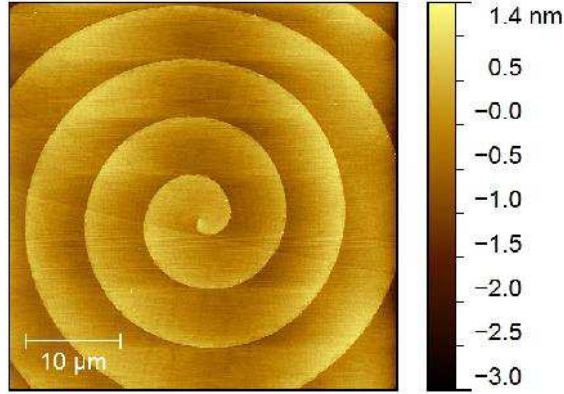


**Figure 1.16:** 6H SiC growth spiral.

### The net flux on the crystal surface

The aim of this section is to obtain an equation for the crystal growth rate as a function of the terrace width. The growth rate will depend on the lateral advance of the spiral steps that is in turn controlled by the net flux of adatoms toward the step. Thus the first step of this derivation is to obtain an expression for the net flux on a terrace.

The flux in a small segment  $dx$  on the crystal surface is defined by the incoming and leaving fluxes. Here, only one dimensional diffusion is assumed. The incoming flux consists of the entering surface flux  $j_s(x + dx)$  and the vapour flux  $j_v$ . The adatoms are diffusing on the surface for a time  $\tau$ , which is the mean residence time. If the adatoms are not incorporated into the crystal within this residence time, they re-evaporate and cause the flux  $j_{des}$ . In addition, there is flux  $j_s(x)$  leaving the segment  $dx$ . Fig. 1.17 illustrates all the introduced fluxes.

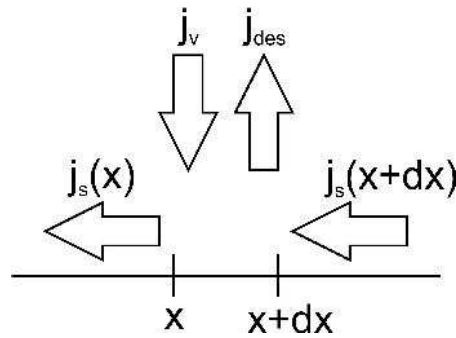


**Figure 1.17:** The fluxes in a segment  $dx$  on the crystal surface.

## 1.4 Growth of SiC crystals

From flux conservation the following equation can be set up:

$$j_s(x) - j_v dx = j_s(x + dx) - j_{des} dx \quad (1.4)$$

Without steps and equilibrium the vapour flux would result in a concentration  $c_m$  of adatoms on the surface. The lifetime of these adatoms is limited by the mean residence time  $\tau$ . Thus the concentration  $c_m$  can be defined by

$$c_m = j_v \tau. \quad (1.5)$$

The concentration profile on a spiral terrace is described by  $c_s$ . At the terrace edge, *i.e.*  $x = \pm\Lambda/2$ , the concentration corresponds to the equilibrium concentration  $c_{eq}$ .

The flux of the re-evaporating atoms depends on the surface concentration of adatoms and also on the mean time of residence:

$$j_{des} = \frac{c_s}{\tau} \quad (1.6)$$

The diffusion of the adatoms on the crystal surface is controlled by the concentration gradient. Applying Fick's first law gives

$$j_s(x) = -D \frac{dc_s}{dx} \quad (1.7)$$

where  $D$  is the surface diffusion constant.

Inserting the previously defined fluxes in Eq. 1.4 results, after rearranging, in:

$$-D \frac{d^2 c_s}{dx^2} = \frac{1}{\tau} (c_m - c_s) \quad (1.8)$$

The surface diffusion length is defined as [48]

$$\lambda_s = \sqrt{D\tau}. \quad (1.9)$$

With the latter equation and Eq. 1.8 a differential equation for the surface concentration can be set up:

$$\lambda_s^2 \frac{d^2 (c_s - c_m)}{dx^2} - (c_s - c_m) = 0 \quad (1.10)$$

The boundary condition for this equation is that at the edges the surface concentration assumes the equilibrium value; *i.e.*  $c_s(x = \pm\Lambda/2) = c_{eq}$ .

## 1 Fundamentals

Solving the differential equation with the approach  $(c_s - c_m) = A \exp(Kx)$  results in

$$(c_s - c_m) = A \exp(x/\lambda_s) + B \exp(-x/\lambda_s). \quad (1.11)$$

Due to the symmetric boundary condition it follows that both constants A and B are equal. Making further use of the relation  $\cosh(x) = \exp(x) + \exp(-x)$  the differential equation becomes

$$(c_s - c_m) = A \cosh(x/\lambda_s). \quad (1.12)$$

The boundary condition leads to an expression for the constant A:

$$A = \frac{c_{eq} - c_m}{\cosh\left(\frac{\Lambda}{2\lambda_s}\right)} \quad (1.13)$$

Thus the concentration on the surface is

$$c_s = c_m + (c_{eq} - c_m) \frac{\cosh(x/\lambda_s)}{\cosh(\Lambda/2\lambda_s)}. \quad (1.14)$$

Fig. 1.18 illustrates the concentration on a terrace. If the surface diffusion length is smaller than the half terrace width, a maximum builds up at the terrace centre. The overlapping of the diffusion fields, i.e.  $\lambda_s > \Lambda/2$ , results in a lowered maximum concentration. In this case, not only atoms close to the edge are incorporated into the crystal but also those far away. As a consequence, the maximum concentration is reduced.

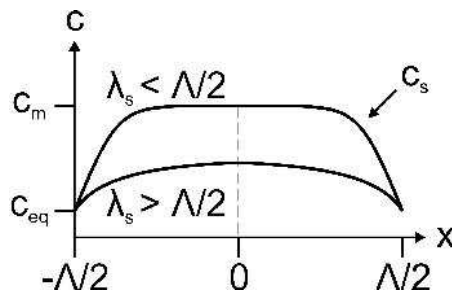


**Figure 1.18:** The concentration profile on a spiral terrace.

The advance of a step is driven by the net flux of adatoms towards this step. The net flux per unit surface  $j_{net}$  can be considered to be the difference between the adatoms arriving on the surface from the vapour phase and the adatoms re-evaporating from the terrace. The latter depends on the supersaturation function

$c_s$ . Hence, the equation

$$j_{net} = j_v - \frac{1}{\Lambda} \int_{-\Lambda/2}^{\Lambda/2} \frac{c_s}{\tau} dx \quad (1.15)$$

can be set up for the net flux. The net flux can then be, after solving the integral and using the relation  $\sinh(x_1) - \sinh(x_2) = 2 \sinh\left(\frac{x_1-x_2}{2}\right) \cosh\left(\frac{x_1+x_2}{2}\right)$ , expressed by

$$j_{net} = \frac{2\lambda_s}{\tau\Lambda} (c_m - c_{eq}) \tanh\left(\frac{\Lambda}{2\lambda_s}\right). \quad (1.16)$$

However, this equation is only valid for a straight step. If a step is curved this flux is modified.

### Surface concentration with Ehrlich-Schwoebel barrier

The surface concentration on terrace is changed if the Ehrlich-Schwoebel effect is present [49][50]. The incorporation of adatoms from an upper terrace in a lower edge can be impeded or even totally suppressed by this effect. In chapter 2.3.3 the Ehrlich-Schwoebel effect is discussed in detail. Here, we focus on its influence on the surface concentration profile.

Assuming that the incorporation of adatoms from an upper terrace is not possible due to a large Ehrlich-Schwoebel barrier the boundary condition of the differential equation 1.10 at the descending edge changes to  $dc_s/dx|_{x=\Lambda/2} = 0$ . The solution of the surface concentration is then:

$$c_s = c_{eq} + (c_{eq} - c_m) - (c_{eq} - c_m) \cosh\left(\frac{\Lambda + 2x}{2\lambda_s}\right) + (c_{eq} - c_m) \sinh\left(\frac{\Lambda + 2x}{2\lambda_s}\right) \tanh\left(\frac{\Lambda}{\lambda_s}\right) \quad (1.17)$$

Fig. 1.19 shows a comparison of the concentration profile on a terrace with and without Ehrlich-Schwoebel effect for  $\lambda_s < \Lambda/2$ . At the descending edge ( $\Lambda/2$ ) the concentration approaches  $c_{eq}$  without and  $c_{max}$  with ES barrier. The net flux can be calculated in an analogous manner as for a terrace without ES barrier. The focus here is on the principle derivation of the BCF theory and therefore the ES effect is neglected in the following.



## 1 Fundamentals

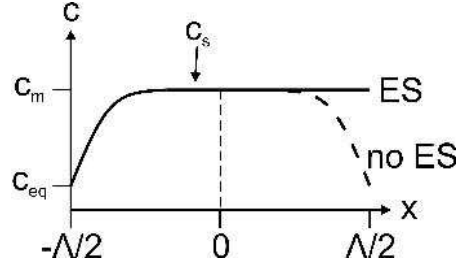


**Figure 1.19:** The concentration profile on terrace with (solid) and without (dashed) Ehrlich-Schwoebel (ES) effect for  $\lambda_s < \Lambda/2$ .

### The Gibbs-Thomson effect

The Gibbs-Thomson effect describes the fact that the chemical potential of a straight step is not the same as for a curved one. As spiral steps are curved, this effect has to be taken into consideration for the step advance. It results in a modification of the equilibrium concentration  $c_{eq}$  appearing in Eq. 1.16.

First, a two dimensional nucleus with the shape of a disc on a substrate of the same nature is assumed. The radius of this disc is  $\rho$  and its height corresponds to one mono-atomic layer  $a$ . If new atoms are incorporated at the disk edge, the radius increases by  $dr$  (Fig. 1.20) and the perimeter changes by  $dP = 2\pi d\rho$ .

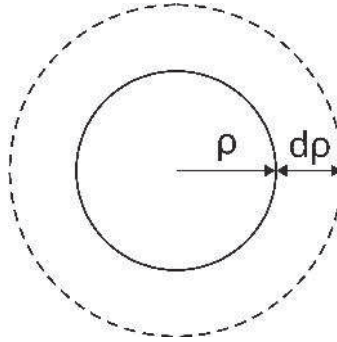


**Figure 1.20:** A two dimensional disc with radius  $\rho$  expands by  $d\rho$ .

The area occupied by the atoms of the disc  $n_s$  is equal to the disc area, i.e.  $n_s a^2 = \rho^2 \pi$ . If a new layer is formed around the disc with  $dn_s$  atoms it follows that

$$dn_s a^2 = 2\pi \rho d\rho = \rho dP. \quad (1.18)$$

The latter equation can be multiplied by the specific edge energy  $\varkappa$  on both sides in order to get an expression in terms of energy. The work  $\mu_v - \mu_s$ , which is the driving force, to transfer the atoms  $dn_s$  from the gas phase to the nucleus is

## 1.4 Growth of SiC crystals

compensating the increase of the edge energy and hence it follows that

$$(\mu_v - \mu_s)dn_s = \frac{\varkappa a^2}{\rho}dn_s. \quad (1.19)$$

The definition of the driving force reads [48]

$$\Delta\mu = k_B T \ln \left( \frac{c_c}{c_{eq}} \right) \quad (1.20)$$

where  $T$  is the temperature,  $k_B$  the Boltzmann constant,  $c_c$  the concentration of adatoms at the edge of a curved and  $c_{eq}$  the one of a straight step. Equating  $\Delta\mu$  from Eq. 1.20 in Eq. 1.19 results, after rearranging, in

$$c_c = c_{eq} \exp \left( \frac{\varkappa a^2}{\rho k_B T} \right) \simeq c_{eq} \left( 1 + \frac{\varkappa a^2}{\rho k_B T} \right). \quad (1.21)$$

The larger the radius  $\rho$  becomes, the more the concentrations at the edge of a curved and a straight step approach. This agrees with the fact that a step becomes almost straight for a large radius.

Now, the concentration on a terrace with curved steps is regarded. The difference between the concentration on the middle of the terrace  $c_m$  and the concentration on the edge  $c_{edge}$  is

$$\Delta c = c_m - c_{edge} = c_m - c_{eq} \left( 1 + \frac{\varkappa a^2}{\rho k_B T} \right) \quad (1.22)$$

Eq. 1.21 was used to replace  $c_{edge}$  in this equation.

By adding and immediately subtracting  $c_{eq}$  from Eq. 1.22, this equation can be transformed to

$$\Delta c = (c_m - c_{eq}) \left( 1 + \frac{c_{eq}}{c_m - c_{eq}} \frac{\varkappa a^2}{\rho k_B T} \right). \quad (1.23)$$

If  $\Delta c$  is equal to zero, the disc is in equilibrium with the vapour phase. From this condition the critical radius  $\rho_c$  can be derived:

$$\rho_c = \frac{c_{eq}}{c_m - c_{eq}} \frac{\varkappa a^2}{k_B T} \quad (1.24)$$

Above this critical radius, a nucleus is stable and should continue to grow. If the radius of the nucleus is lower than the critical one, it might decay.

Eq. 1.23 can be simplified to

$$\Delta c = (c_m - c_{eq}) \left( 1 + \frac{\rho_c}{\rho} \right) \quad (1.25)$$

## 1 Fundamentals

by introducing the critical radius from Eq. 1.24.

The expression  $c_m - c_{eq}$  in Eq. 1.16 can be substituted by  $\Delta c$  from Eq. 1.25 and hence the net flux towards a curved step changes to

$$j_{net} = \frac{2\lambda_s}{\tau\Lambda} \sigma c_c \tanh\left(\frac{\Lambda}{2\lambda_s}\right) \left(1 - \frac{\rho_c}{\rho}\right) \quad (1.26)$$

where  $\sigma = (c_m - c_{eq})/c_{eq}$  is the supersaturation.

### The growth rate

The advance of a step is determined by the net flux on the terrace:

$$v = a^2 j_{net} \Lambda \quad (1.27)$$

With the previously obtained equation for the net flux (Eq. 1.26) the velocity of the step can be expressed by

$$v = \frac{2a^2}{\tau} \lambda_s \sigma c_{eq} \tanh\left(\frac{\Lambda}{2\lambda_s}\right) \left(1 - \frac{\rho_c}{\rho}\right) = v_s \left(1 - \frac{\rho_c}{\rho}\right) \quad (1.28)$$

where  $v_s$  is the rate of advance of a straight step. This equation approximates the spiral shape by concentric circular clusters with constant terrace width.

In the following derivation of the growth rate, the effect of the step curvature on the step advance is neglected. The effect of the curvature decreases with  $1/\rho$  and therefore steps far away from the step can be treated like straight parallel steps. If the spiral density is low, this is a reasonable approximation.

The crystal growth rate depends on the step density  $a/\Lambda$  and the step advance rate [48]:

$$R = \frac{a}{\Lambda} v = 2 \frac{a^3}{\tau} \frac{\lambda_s}{\Lambda} \sigma c_{eq} \tanh\left(\frac{\Lambda}{2\lambda_s}\right) \quad (1.29)$$

The advance rate of a straight step is used in the latter equation. In order to simplify this equation, an expression for the terrace width is derived.

Assuming that the spiral is of the Archimedean type, the shape is described by [48]

$$\rho = 2\rho_c \varphi \quad (1.30)$$

where  $\varphi$  is the rotation angle of the spiral.

The distance between two successive steps, or the terrace width, is

$$\Lambda = r(\varphi + 2\pi) - r(\varphi) = 2\rho_c[(\varphi + 2\pi) - \varphi] = 4\pi\rho_c. \quad (1.31)$$

#### 1.4 Growth of SiC crystals

Cabrera and Levine determined the terrace width more precisely to be [6]

$$\Lambda = 19\rho_c = \frac{19\kappa a^2}{\sigma k_B T}. \quad (1.32)$$

Two limiting cases for the growth rate can be distinguished. The first one is that the surface diffusion length is much smaller than the spiral terrace width  $\lambda_s \ll \Lambda$ . By inserting  $\Lambda$  from Eq. 1.32 and  $\rho_c$  from Eq. 1.24 in Eq. 1.29 the parabolic growth law of Burton, Cabrera and Frank is obtained [5]:

$$R = C \frac{2\lambda_s k_B T}{19\kappa a^2} \sigma^2 = C \frac{\sigma^2}{\sigma_c} \quad (1.33)$$

or equivalently

$$R = C \frac{4\lambda_s^2}{\Lambda^2} \sigma_c. \quad (1.34)$$

where  $C = a^3 c_c \tau$  is a constant and  $\sigma_c = 19\kappa a^2 / (2\lambda_s k_B T)$  the critical supersaturation. Above this supersaturation the derived law is no longer valid.

Then, the diffusion length is much larger than the terrace width ( $\lambda_s \gg \Lambda$ ) and the growth rate becomes

$$R = C\sigma = C \frac{2\lambda_s}{\Lambda} \sigma_c. \quad (1.35)$$

Fig. 1.21 illustrates the two growth laws.

The supersaturation cannot be determined during the vapour growth of SiC. However, the equations of BCF allow to determine the relative supersaturation by measuring the spiral terrace widths and crystal growth rates.

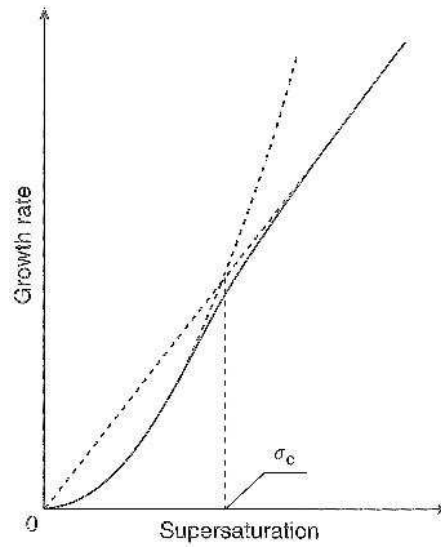


**Figure 1.21:** At low supersaturation the growth rate of a spiral is a parabolic function of the supersaturation. Above the characteristic supersaturation  $\sigma_c$  the growth rate increases linear with the supersaturation. Image taken from [48].

## 2 On-axis growth of SiC

In this chapter some aspects of the on-axis SiC growth are studied. First of all, the experimental setup and the growth parameters are discussed. Then we will show, that the PVT growth of SiC crystals is limited by the vapour phase transport. Finally, the randomly occurring nucleation on the sample surfaces is analysed. Growth spirals are excluded in this chapter as they are discussed in detail in chapter 3.

### 2.1 Experimental setup and growth conditions

The aim of this thesis is to understand the fundamental processes on the crystal surface during the PVT growth of SiC. This requires not only a knowledge of the theoretical processes but also of the experimental growth conditions and the analysis of the surfaces. Therefore, the experimental setup is presented in this section followed by the description of the chosen growth conditions. Furthermore the procedure for surface analysis is shown. The characterization tools themselves are briefly described in the appendix.

#### 2.1.1 Growth reactor

A home-made PVT reactor was used to grow SiC single crystals. The setup is shown schematically in Fig. 2.1. Inside a quartz tube, a graphite crucible is heated inductively. The quartz tube is double walled and cooled with water. The rotary vane pump can be connected to the tube via an angle valve (V1). The needle valve V2 is used for controlling the pump down rate. On top of the reactor a pyrometer reads the temperature at the graphite crucible through a window. The pressure is measured by the capacitance manometer P1 for  $p > 1$  mbar and by the cold cathode pirani gauge P2 for  $p < 1$  mbar. For safety reasons a relief valve (V5) is installed. Argon gas can be inserted into the reactor via valve V3.

The geometry of the crucible, shown in Fig.2.2, was developed and optimized in previous work in the laboratory [51] [52] and is still issue of other theses in this laboratory. The structure of the crucible reminds of a Matryoshka doll as there are several stacked parts inside. Fig.2.3 shows a photo with all the graphite parts used.

## 2 On-axis growth of SiC

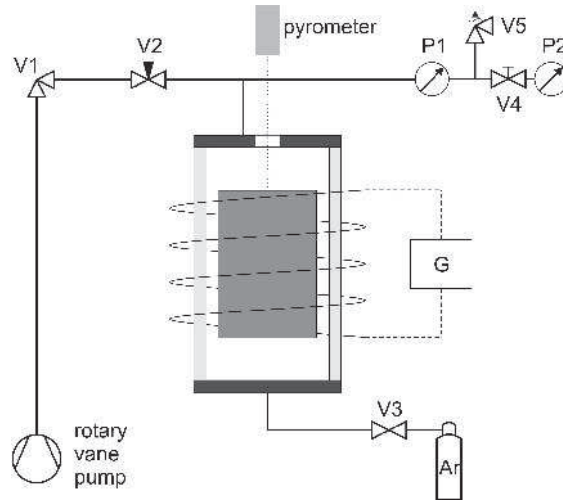


**Figure 2.1:** Schematic drawing of the basic PVT setup.

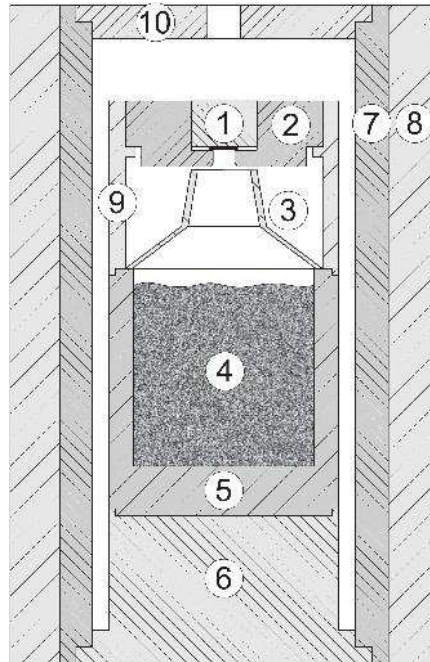


**Figure 2.2:** A schematic section of the used crucible.(1) plug to fix substrate and avoid its evaporation; the small black rectangle below is the substrate (2) sample holder (3) cone to confine the flux towards the substrate (4) SiC powder (5) crucible (6) base (7) heating element (8) thermal insulation (9) spacer (10) top cover.

## 2.1 Experimental setup and growth conditions



**Figure 2.3:** The crucible Matryoshka. The parts shown are (from left to right): Thermal insulation, heating element with top cover, powder crucible on base, spacer, cone, sample holder and plug.

SiC powder is filled in a crucible and a piece of silicon (mass about 0.6 g) is placed on top. This is necessary to avoid the graphitization of the seed that occurs due to the silicon loss during heating up. Graphitization causes the generation of additional defects and is suppressed by introducing excess silicon in the crucible.

The flux of the sublimating SiC towards the substrate is confined by a cone. The spacer around the cone sustains the sample holder. A widespread method to fix the substrate is to glue it on the sample holder. In the setup used for this thesis a non-gluing method is used. The sample is placed on a hole in the holder (part 2 in Fig. 2.2). This hole is slightly smaller than the seed and thus prevents it from falling on the powder. A plug above the seed fixes its position and also suppresses its evaporation. There are important advantages of this non-glueing method. The introduction of stress during heating due to different expansion coefficients of substrate and sample holder is avoided. Furthermore the sample cannot drop off as it is sometimes the case for glued seeds. In addition, for short time experiments the sample holder and the cone can be re-used. Finally, parasitic nucleation around the seed can be reduced.

The heating element, a solid graphite cylinder, is placed around powder source and sample holder. An outer graphite foam tube acts as thermal insulation. All parts of the crucible are made of graphite to avoid incorporation of impurities in the growing crystal.

### 2.1.2 Seed preparation and growth conditions

For the growth of SiC crystals 6H and 4H on-axis substrates, epi-ready polished by Novasic and cut to  $0.9\text{ cm}^2$  squares, have been used. The polytype of the substrates was confirmed by Raman spectroscopy. The defect densities of the substrates were determined by KOH etching to be in the range of  $2.9 \cdot 10^4\text{ cm}^{-2}$  to  $3.1 \cdot 10^4\text{ cm}^{-2}$  (Fig. 2.4). The crystal face, C or Si, was chosen depending on the aim of the experiment.

The growth process was similar for all experiments and is exemplary shown in



## 2 On-axis growth of SiC

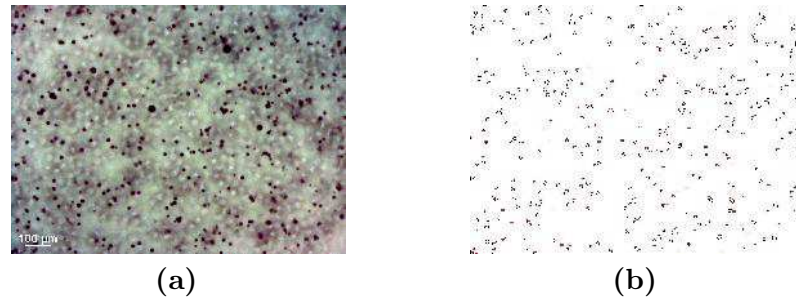


**Figure 2.4:** In order to determine the defect density of the substrates, they were etched 5 minutes in KOH at 550 °C. (a) Surface of an etched substrate. (b) After image processing with *ImageJ* the defects were counted.

Fig. 2.5. There are four stages of the growth process:

1. manual heat up
2. temperature ramp
3. deposition
4. cooling

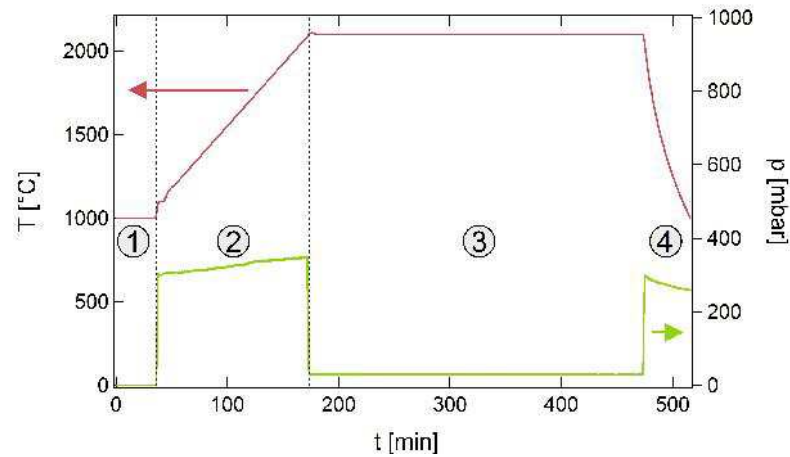


**Figure 2.5:** Recorded data of a typical growth process. (1) Manual heating until the pyrometer starts temperature reading (2) Automatic heat ramp (3) Deposition (4) Cool down.

In the first step, the power in the induction coil was increased in small intervals until the pyrometer started reading temperature ( $T \geq 1000^\circ\text{C}$ ). Then the ramp pressure was set by inserting argon while the temperature was kept stable at  $1100^\circ\text{C}$ . This pressure was always larger than the deposition pressure in order to

## 2.1 Experimental setup and growth conditions

avoid crystal growth at non-stable conditions. As the growth is limited by vapour transport (see chapter 2.2), a high pressure in the reactor suppresses crystal growth. For experiments with deposition pressures lower than 250 mbar, the ramp pressure was set to 300 mbar. Above deposition pressures of 250 mbar, the ramp pressure was always 100 mbar higher than the deposition pressure. During the heat ramp the pressure increases due to outgassing of the graphite parts and the powder. The heating rate was  $7.5^{\circ}\text{C}/\text{min}$  for all experiments.

When the deposition temperature of  $2100^{\circ}\text{C}$  was reached, the pressure in the reactor was adjusted by pumping down. Both, pressure and temperature, remained constant during deposition. Fig. 2.6 shows a picture of the crucible during crystal growth at  $2100^{\circ}\text{C}$ . The deposition time on Si-face substrates was always 2 hours contrary to the C-face where the time was different for each experiment. This was necessary in order to avoid the overgrowth of simple spirals by micropipes (see chapter 3.2).

After deposition, the power in the induction coils was turned off and the pressure was increased again by inserting argon to stop the growth process. The pressure was the same as in the beginning of stage two. The decrease in pressure is caused by the cooling of the gas.

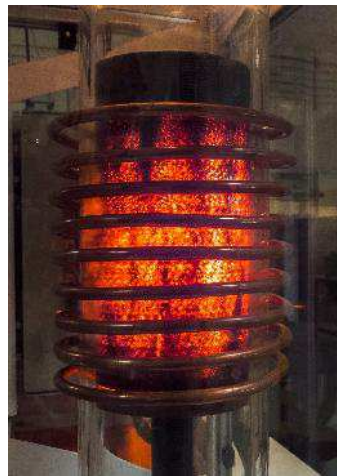


**Figure 2.6:** The crucible at  $2100^{\circ}\text{C}$ .

### 2.1.3 Sample Characterization

The surfaces of the grown crystal were first analysed by an optical *Leica DM LM* and a differential interference contrast (DIC) *Zeiss Axioskop 40* microscope. A map of each sample is stitched from images taken at lowest magnification (Fig. 2.7). Growth spirals were identified by DIC microscopy and their positions marked

## 2 On-axis growth of SiC

on the stitched map. Then images of the same spirals were taken by a *Veeco dimension 3100* atomic force microscope (AFM) in contact or tapping mode. The spiral polytype was verified by a *Jobin-Yvon/Horiba LabRam* Raman spectrometer with a laser operating at 514 nm. Fig. 2.8 shows a typical Raman spectrogram. A dial gauge was used to measure the crystal thickness. All these techniques are non-destructive.

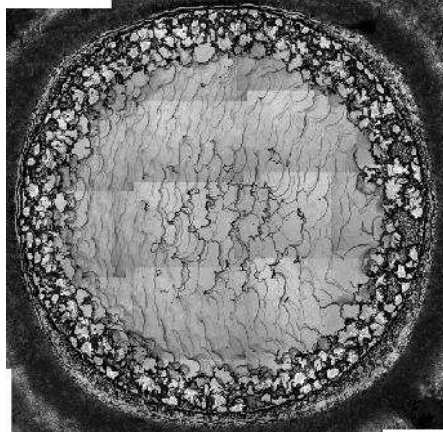


**Figure 2.7:** Map created from several optical images.

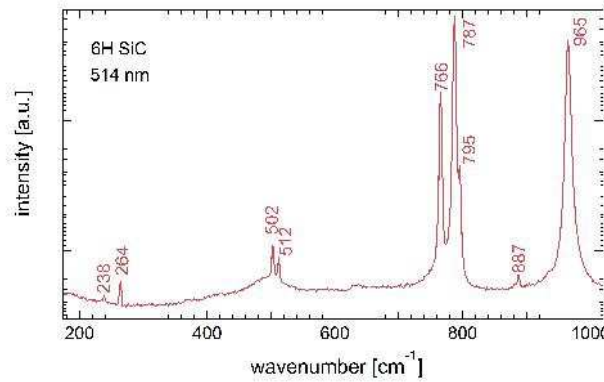


**Figure 2.8:** Example of a 6H SiC Raman spectrogram.

In some cases the samples were additionally analysed by field emission gun scanning electron microscopy (FEG-SEM), transmission electron microscopy (TEM) or Laue diffraction. However, FEG-SEM and TEM are both destructive methods and thus only employed after full characterization of the sample. The FEG-SEM deposits a carbon layer on the surface that could not be removed (Fig. 2.9). TEM analysis either requires the deposition of a protection layer if the sample is prepared by focused ion beam (FIB) or cutting and thinning. In both cases further

## 2.2 Growth rate limiting step

characterization of the surface is not possible. Laue diffraction was performed before TEM analysis to determine the orientation of the crystal. The analytic methods and tools are described in short in the appendix.

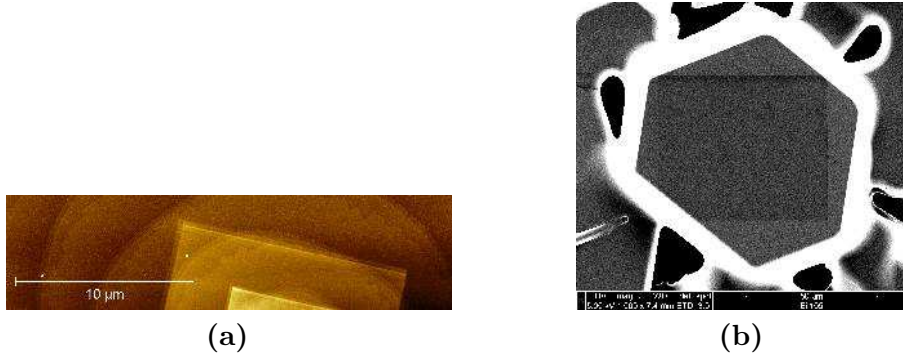


**Figure 2.9:** Taking a picture by FEG-SEM creates a non-removable carbon layer on the surface. (a) detail of an AFM image showing the carbon layer deposited by FEG-SEM (bright areas). (b) Re-scanning the same area with a lower magnification also reveals a deposited carbon layer in the FEG-SEM. Note that the images are not showing the same spiral.

## 2.2 Growth rate limiting step

### Introduction

The growth rate of crystals grown in the vapour phase can be, in principle, limited by two processes. The first might be the transport of the vapour phase. The solid phase is sublimating and diffusing to the seed surface. The phase transition, from solid to vapour, is accompanied by a change in volume causing the advective flow. Due to the concentration gradient of the sublimating species Fickian diffusion is taking place.

The second limiting process may be the surface diffusion and incorporation of the adsorbed species on the crystal surface. If the crystal growth rate is limited by the incorporation of the atoms, the surface concentration of adatoms is constant. Thus, the arriving flux is not of importance for the growth rate.

In this section the growth rate limiting step of the PVT technique is determined.

## 2 On-axis growth of SiC

### Experimental details

The growth process is the same as described in chapter 2.1.2. As substrates 6H on-axis SiC with Si- and C-face were used. The C-face substrates are cut from two different wafers. The growth rate was controlled by the argon pressure set in the reactor. The range of this pressure was 10 - 400 mbar. The growth rate was determined by measuring the crystal thickness with a dial gauge.

### Results and discussion

Fig. 2.10 shows a plot of the growth rate versus pressure. For the growth on the C-face two different substrates were used, indicated by open triangles and squares. The power exponent of the fitted Si-face data is -0.83. Consequently, the growth rate is almost inversely proportional to the pressure in the reactor. The deviation of the C-face data to the Si-face fit is small and thus it can be concluded that the growth on both faces follows the same law. The inset illustrates the PVT growth process and the concentration of adatoms on a terrace for  $\lambda_s \ll \Lambda$  and without Ehrlich-Schwoebel effect.

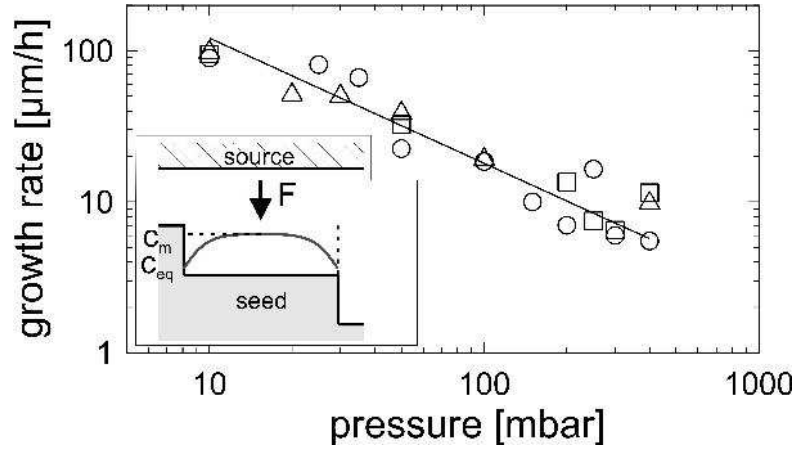


**Figure 2.10:** The growth rate is almost inversely proportional to the pressure for Si- (open circles) and C-face (open triangles and squares). The exponent of the fit (black line) is -0.83 and thus close to -1.

Following the derivation of E. Kaldis and M. Piechotka it can be shown that the Fickian diffusion and advective flow in the vapour phase limit the growth rate [53].

A vapour phase with two components in an one-dimensional system is assumed. The first component A is the crystallizing species and second component B the inert gas. The flux  $J_A$  of the crystallizing species from the powder source to the

## 2.2 Growth rate limiting step

seed consists of an advective and diffusive flow [53]:

$$J_A = \frac{v_{adv} p_A}{k_B T} - \frac{D_{AB}}{k_B T} \frac{dp_A}{dx} \quad (2.1)$$

In this equation  $v_{adv}$  is the advective velocity,  $p_A$  the partial pressure of species A and  $D_{AB}$  the diffusion coefficient of species A into B. Assuming that the growth rate is not limited by surface processes on the seed,  $J_A$  is directly proportional to the growth rate of the crystal.

The diffusion coefficient can be approximated by [53]

$$D_{AB} = D_0 \left( \frac{T}{T_0} \right)^n \frac{p_0}{p} \quad (2.2)$$

where  $D_0$  is the diffusion coefficient at a temperature  $T_0$  and a pressure  $p_0$ . Neglecting the advective flow in Eq. 2.1 results thus in an inversely proportional dependence of  $J_A$  on  $p$ . A more rigorous analysis can also be conducted as follows.

The inert gas flux  $J_B$ , which is zero in total, can be defined by [53]:

$$J_B = \frac{v_{adv} p_B}{k_B T} - \frac{D_{BA}}{k_B T} \frac{dp_B}{dx} = 0 \quad (2.3)$$

Here,  $p_B$  is the partial pressure of the inert gas and  $D_{BA}$  the diffusion coefficient of species B into A.

The total pressure in the reactor is the sum of both partial pressures  $p = p_A + p_B$ . Assuming that the sublimating species A is not changing the total pressure it follows that  $dp/dx \approx 0$ . Adding both fluxes  $J_A$  and  $J_B$  up the following equation is obtained:

$$J_A + J_B = \frac{v_{adv}}{k_B T} (p_A + p_B) - \frac{D_{AB}}{k_B T} \frac{dp_A}{dx} - \frac{D_{BA}}{k_B T} \frac{dp_B}{dx} \quad (2.4)$$

Since  $J_B = 0$  and  $d(p_A + p_B)/dx \approx 0$  the advective velocity can be expressed by

$$v_{adv} = \frac{J_A k_B T}{p}. \quad (2.5)$$

Substituting  $v_{adv}$  in Eq. 2.1 by the one from Eq. 2.5 results in:

$$J_A = - \left( \frac{p D_{AB}}{k_B T} \frac{1}{p - p_A} \right) \frac{dp_A}{dx} \quad (2.6)$$

Since the diffusion constant is inversely proportional to the pressure, the principle dependency reads  $J_A \propto 1/(p - p_A)$ . The deviation of the fit parameter in Fig. 2.10

## 2 On-axis growth of SiC

can be consequently explained by the advective flow. This advective flow has also been observed by other authors for the PVT growth [54] [55]. In this derivation convection was neglected but nevertheless it should be mentioned that this effect is also affecting the power exponent. Obviously, convection is dependent on the crucible geometry. In the literature, however, the deviation of the fit exponent from -1 is usually only explained by the advective flow.

To conclude, the growth rate is limited by the vapour phase transport and not by the incorporation of the adatoms on the crystal surface. The kink density, and consequently defect density, of the crystal is sufficiently high not to lower the growth rate.

## 2.3 Nucleation

Nucleation is a well known growth mechanism that takes place above the critical supersaturation. During the PVT growth of SiC, nucleation is randomly observed. In general, this is an unwanted growth process as it is assumed that nucleation induces stacking faults. Righi *et al.*, for example, performed ab initio calculations and concluded that the cubic phase is favored during layer-by-layer growth independently of the substrate polytype [56]. Yet, this chapter shows that interesting phenomena can be observed by analyzing the nuclei on the crystal surfaces.

### 2.3.1 Experimental details

During the surface characterization of the samples grown for the spiral analysis in chapter 3.3, nucleation was occasionally observed on both Si- and C-face. One sample per face was selected for the analysis. The Si-face crystal was grown for two hours at 250 mbar and the C-face crystal for four hours at 400 mbar. The polytype was in both cases 6H. Images of spiral surfaces were taken by AFM.

Only nuclei exceeding a critical size were considered in the following analysis. On the C-face, this length was defined to be  $\gtrsim 1.5 \mu\text{m}$ . Nuclei whose diameter correspond to this value show second layer nucleation and are thus assumed to be the first nuclei formed. The critical length on the Si-face was  $\gtrsim 0.9 \mu\text{m}$ . The shape of nuclei of this size is dendritic while smaller ones only show rudimentary formation of dendrites.

In order to estimate the surface diffusion length the distance of the nuclei to their next neighbour was measured. Furthermore, the relative position of the nuclei on the terrace was measured. This gives information of the general nuclei distribution on the terraces. Fig. 2.11 illustrates the measured quantities.



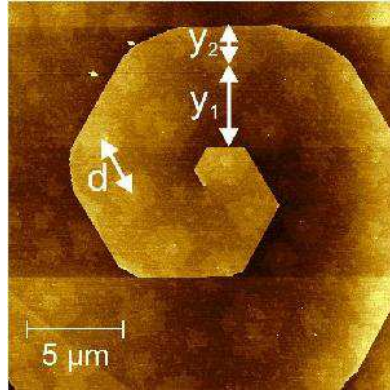


**Figure 2.11:** Nucleation on a 6H spiral (Si-face). The distance between next neighbouring nuclei  $d$  and the relative position  $y_1$  and  $y_2$  of the nuclei on the terrace were measured.

### 2.3.2 Observed Nuclei

The nuclei shape is not observed to be dependent on the substrate polarity or deposition pressure as demonstrated in Fig. 2.12. In most cases the nuclei are irregularly shaped, but we also observed hexagonal or dendritic nuclei.

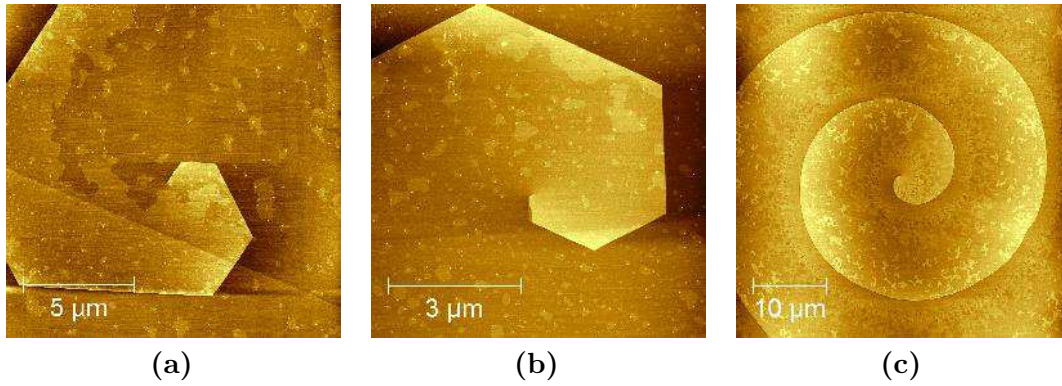


**Figure 2.12:** The shape of the nuclei could not be related to deposition pressure or seed polarity. (a) 6H spiral Si-face, 300 mbar. (b) 6H spiral Si-face, 150 mbar. (c) 15R spiral C-face, 200 mbar.

AFM images of the samples considered for the analysis of nuclei distribution are shown in Fig. 2.13. We have chosen these samples since there is no continuous layer formed on the edge of the spiral steps (as, for example, in Fig. 2.12 (a) and (b)). On the Si-face the shape of the nuclei is dendritic and the height of the nuclei corresponds to one bilayer ( $2.5\ \text{\AA}$ ). Some nuclei show initial formation of a second nucleation layer.



## 2 On-axis growth of SiC

The nuclei on the C-face are circular shaped and ragged at the edges. Second layer nucleation can be observed on many nuclei. The height is also  $2.5 \text{ \AA}$  per layer. In addition many small nuclei are present between the larger ones.

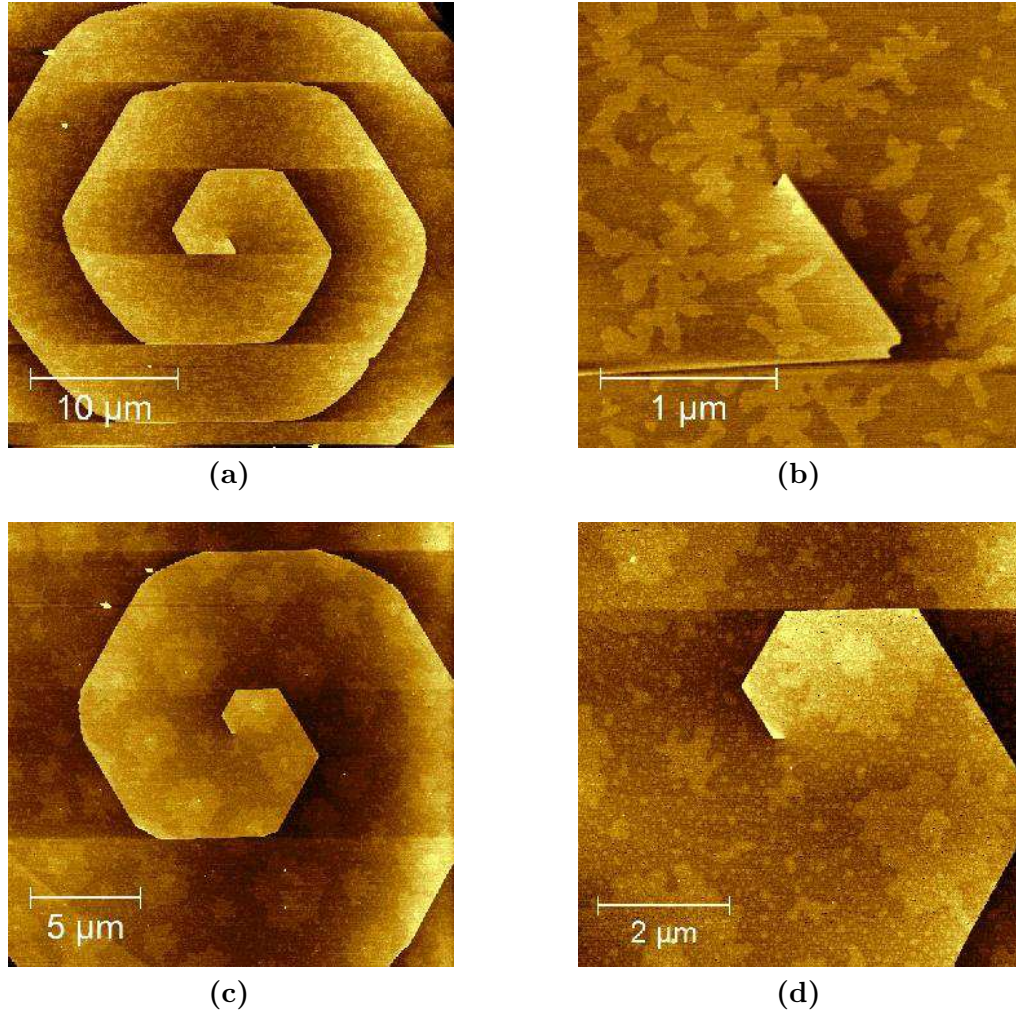


**Figure 2.13:** Samples used for the analysis. (a) and (b) are showing a spiral on Si-face grown at 250 mbar. (b) and (c) are images of the C-face sample grown at 400 mbar.

Ogura *et al.* studied Au islands on Ir(111) and Pt(111) by scanning transmission microscopy and performed simulations on the shape of the islands [57]. They observed a transition from dendritic to triangular or hexagonal shape with increasing number of deposited monolayers. Moreover they noticed that the nuclei shape is dependent on the substrate. According to their simulations, anisotropic diffusion at the island edges is responsible for the shape of the islands. Following the conclusion

of Ogura *et al.*, the nuclei shape on our samples should be dependent on the spiral polytype. The different stacking sequences of the polytypes should affect the anisotropic diffusion on the nuclei. Since we do not observe such a polytype dependence of the nuclei, we conclude that the anisotropic diffusion of the adatoms on the edges is not responsible for the island shape.

The shape of islands is also known to be temperature dependent. Michely and Krug showed that the shape of Pt islands on Pt(111) changes from dendritic to hexagonal with increasing deposition temperature [58]. Hence, it is assumed that the temperature on the seed surface was not always the same during the crystal growth. This seems to be reasonable as the temperature is not directly read on the seed but on a graphite plug above. The contact between seed and graphite plug is probably not always the same resulting in different thermal coupling and thus different seed temperatures. Furthermore, it is not clear at which stage of the growth process the nucleation is taking place. The polytypic transformation on the C-face suggests that the nucleation is taking place during growth, but we cannot exclude that the nuclei form during the cooling of the reactor at the end of the crystal growth.

Another interesting aspect to be discussed in this context is the polytype of the nuclei. Experimental results and first principle total energy calculations suggest that, independent of the underlying substrate polytype, a newly formed layer prefers the cubic stacking [59][56]. However, according to Fissel the 3C polytype is not always the preferred one during nucleation [60]. Other polytypes may form depending on pressure and temperature. Therefore it might be interesting to check experimentally the stacking of the nuclei.

On the Raman spectra only the fingerprint of the 6H polytype is observable (Fig. 2.14). There are two possibilities to explain this spectra. The first one is, that the polytypes of nuclei and substrate are the same and hence the spectra do not show any other polytype.

From the nuclei distribution discussed in the next section, it is evident that Ostwald ripening is taking place during growth. Therefore, the second possibility to explain the spectra is that the nuclei might fully disintegrate. But even if the polytype of the nuclei is different to the substrate, the volume of the nuclei is probably too small to contribute to the Raman spectra. Hence, from the available data it is not possible to clearly verify the nuclei polytype.

High resolution TEM characterization of a cross-section could reveal the real stacking of the nuclei. However, the sample preparation by focused ion beam (FIB) was not successful as it resulted in the amorphization of the top utmost surface.

## 2 On-axis growth of SiC

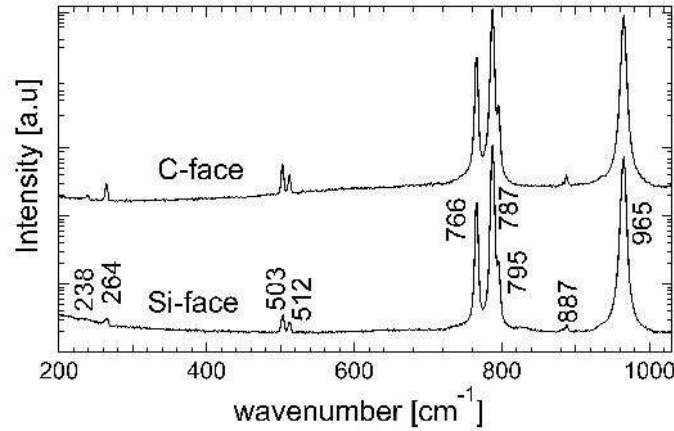


**Figure 2.14:** Raman spectra (laser 514 nm) of the spirals shown in Fig. 2.13. Both spectra show only peaks of the 6H polytype.

### 2.3.3 Nuclei distribution

The histogram of the nuclei on the Si- and C-face spiral steps are shown in Fig. 2.15. On the x-axis the relative position of the nuclei is plotted, *i.e.* 10% is close to the rising step and 100% close to the descending step. The nuclei frequency next to the rising step is on both faces low. This is the depletion zone and it will be discussed at the end of this section.

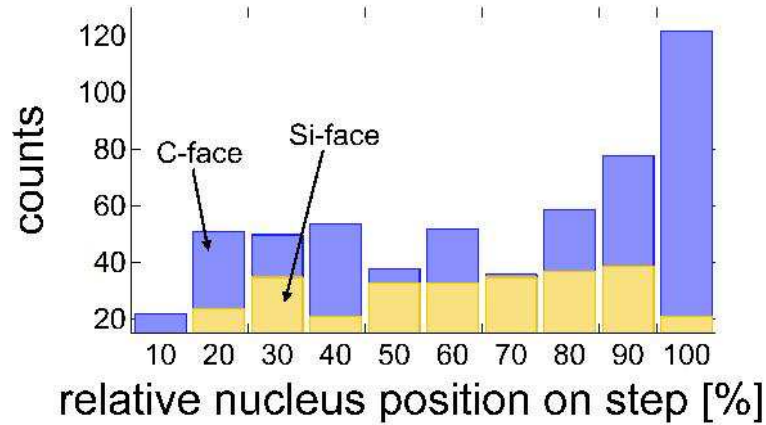


**Figure 2.15:** The nuclei appear cumulated at the descending step of a terrace on the C-face. Next to the rising step less nuclei are counted. Latter is similar for the nuclei on Si-face but also at the descending step less nuclei are observed than in the centre of the terrace.

Between 20 and 80% of the terrace width the nuclei frequency is almost constant

on both faces. However, next to the descending spiral edge the nuclei frequency is increasing on the C-face. This is contrary to the Si-face where the frequency is decreasing in the same way as at the rising step.

The increased frequency of nuclei at the descending step on the C-face is probably related to the Ehrlich-Schwoebel (ES) effect [49][50]. Fig. 2.16 shows a top view of a fcc crystal surface and its section. The adatom A can diffuse easier to the crystal edge than the adatom B on the upper terrace. When the adatom A is diffusing towards the edge it is not only attracted by the atoms 1 and 2 but also by atom 3. Thus the diffusion barrier  $E_{SD}$  is reduced by  $E_{ES2}$  for the adatoms on the lower terrace. In contrast, the upper adatom B is not attracted by the atoms 1, 2 and 3 resulting in an barrier increased by  $E_{ES1}$ . Consequently, adatoms on the lower terrace are rather diffusing towards the crystal edge than the adatoms on the upper terrace. A similar histogram was reported by M. Klaua on the nucleation of Au on a stepped Ag(111) surface [61] and he also concluded that the increase of nuclei at the descending edge is due to an ES barrier.

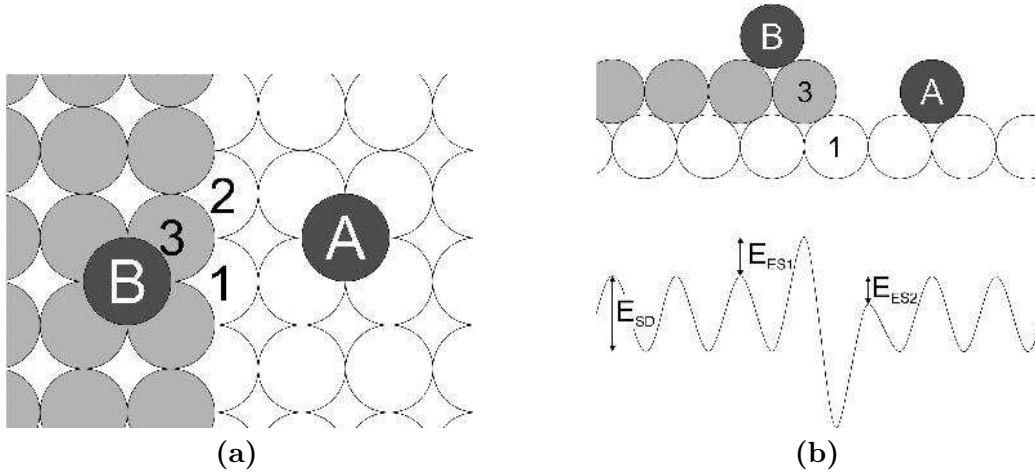


**Figure 2.16:** Schematic illustration of the Ehrlich-Schwoebel effect. (a) Top view on a fcc crystal. (b) Section of the left image with potential diagram. Image taken modified from [48].

The histogram suggests that the Ehrlich-Schwoebel effect is only present on the C-face. However, regarding the AFM images in Fig. 2.12 it can be concluded that the ES barrier can be also present on the Si-face. Note that the step height of the spiral shown in Fig. 2.13 (a) and (b) is the same as those in Fig. 2.12 (a) and (b). Thus a different step height cannot be accounted for the change in the ES barrier. The previously discussed temperature difference on the samples might affect the ES effect and explain its more pronounced appearance on some samples.

## 2 On-axis growth of SiC

Regarding the nuclei in Fig. 2.13 (c) and (d) it is apparent that there is no prevailing Ehrlich-Schwoebel effect for second layer nucleation as these layers are always located in the island centre. Thus, there is an height dependence of the Ehrlich-Schwoebel barrier. Liu et al. showed by simulations of the  $\{001\}$  Al surface that this barrier is increasing with the number of layers of an island [62]. For the first layer the lowest barrier is obtained while saturation is reached when the island consists of three layers. This indicates that the ES barrier is probably insignificant on single bilayers of SiC but important on spiral steps.

The increasing number of nuclei at the descending edge on the C-face, indicates that the diffusion length is larger than the half terrace width, *i.e.*  $\lambda_s > 3.12 \pm 0.52 \mu\text{m}$ . Adatoms can diffuse a larger distance on the C-face, but as the ES barrier prevents adatom incorporation from an upper terrace, the concentration and hence the number of nuclei increases at the descending edge.

Since this effect is not observed on the Si-face, we infer that the surface diffusion length on this face is smaller than the half terrace width, *i.e.*  $\lambda_s < 3.28 \pm 0.21 \mu\text{m}$ .

At the beginning of this section it was mentioned that close to the edges the number of nuclei is low on Si-face whereas it is only low at the rising step on the C-face. The decrease of the amount of nuclei close to the rising edge is caused by the advance of the spiral step and can be related to Ostwald ripening. The chemical potential of the nuclei is higher than the one of the spiral step. Therefore most nuclei close to the rising step will be disintegrated and the atoms are incorporated into the spiral edge. The nuclei free zone next to the (spiral) edge is also called depleted zone [63]. The same effect can be present on the descending edge if the Ehrlich-Schwoebel barrier is low. The distance of the nuclei to the descending edge is larger than for those close to a rising edge, since the step is moving away from the nuclei.

Fig. 2.17 shows the distribution of the nuclei as a function of the edge distance for Si- and C-face. The red bars correspond to distances measured between the nuclei and the rising edge ( $d_1$ ) and the blue bars to the nuclei distance to the descending edge ( $d_2$ ). From this histogram the length of the depletion zones at both edges can be estimated by determining the position of the first maximum from the left.

The length of the depletion zone on the Si-face is  $0.8 \mu\text{m}$  on the rising and  $1.2 \mu\text{m}$  on the descending edge. On the C-face, the distance to the rising edge is also  $0.8 \mu\text{m}$  but only  $0.4 \mu\text{m}$  to the descending edge. A detailed study on the depletion zone for the growth of *e.g.* Si on Si with varying surfactants has been done by Voigtländer *et al.* [64]. According to the authors, the width of the depletion zone is equal to the mean distance of the islands. This is what we observe for the Si-face

but not for the C-face (Fig. 2.18). The next nucleus distance on the Si-face is  $0.86 \pm 0.23 \mu\text{m}$  and  $2.77 \pm 0.55 \mu\text{m}$ . The accumulation of nuclei next to the descending edge on the C-face was previously ascribed to the Ehrlich-Schwoebel effect. Also Voigtländer *et al.* attribute the asymmetry of the depleted zones to an ES barrier. Nevertheless, due to the large next nucleus distance one would expect a much larger depletion zone next to the rising step on the C-face. We assume that the nuclei are too big and can only be partially disintegrated close to this edge. Therefore, the next nucleus distance does not correspond to the depletion zone on the C-face.

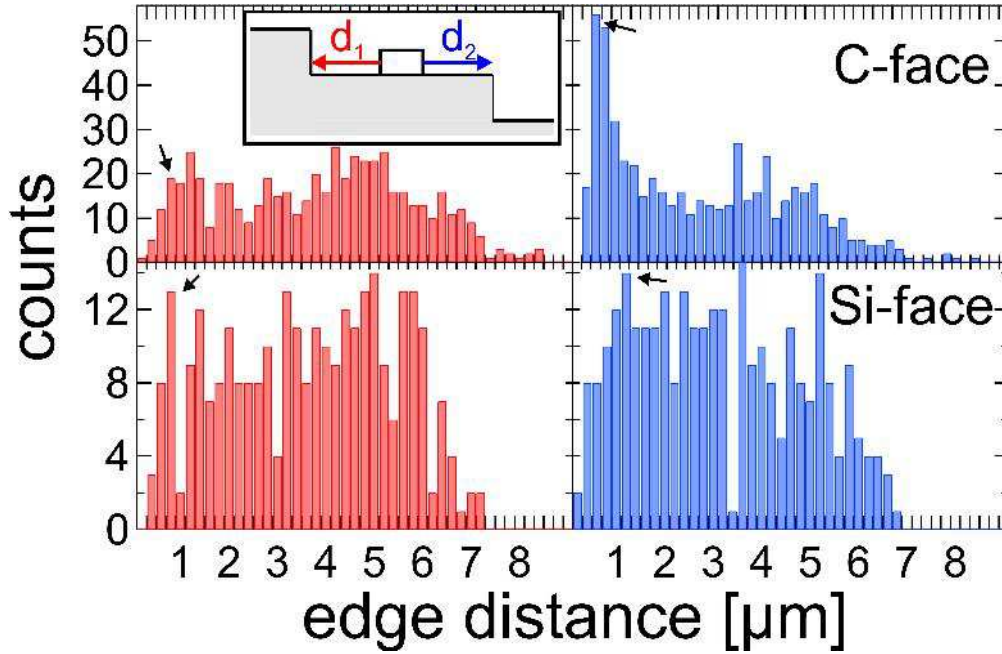


**Figure 2.17:** The distance of the nuclei to the rising (red,  $d_1$ ) and descending (blue,  $d_2$ ) edge. The inset illustrates the distances of the nuclei to the edges.

Yet, nuclei close to the edge might not fully disintegrate and thus cause stacking faults or a change of the polytype. Harada *et al.* described such a mechanism for the top-seeded solution growth on 4H-SiC Si-face seeds [65]. They reported a transition from 4H to 15R or 6H and attributed this polytypic transformation to nucleation on the spiral terraces. Although this seems to be a possible mechanism for the often observed change in the polytype, we will show in chapter 3.1 that a polytypic transformation can take place without the occurrence of any nuclei.

### 2.3.4 Estimating the diffusion length from the nuclei density

The surface diffusion length is an important parameter for the simulation of surface processes. An experimental measurement could be thus helpful for the optimization



## 2 On-axis growth of SiC

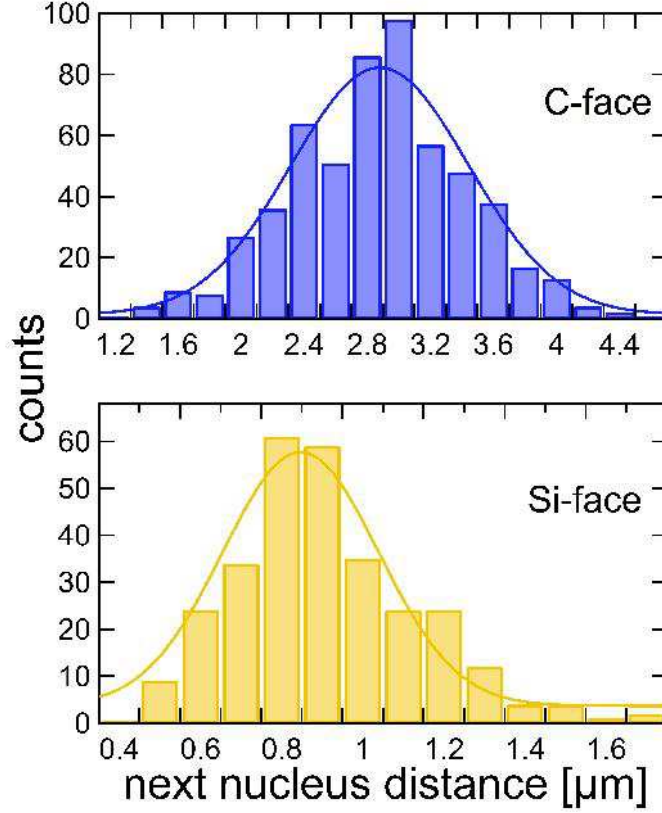


**Figure 2.18:** Histograms of the next nucleus distances on the Si- and C-face.

of these simulations. In the following a short review on the estimation of the diffusion length is given.

Nishizawa and Kimura [66] proposed that the surface diffusion length corresponds to the half average distance between hillocks. They grew epitaxial layers of GaAs by CVD on the  $\{111\}$ B facet of a GaAs substrate and observed the formation of triangular hillocks. Due to the homogeneous distribution and the temperature dependent density of these hillocks the authors concluded that surface migration is the origin of their formation.

Another model for determining the surface diffusion length was proposed by Kimoto and Matsunami [67]. They grew crystals on on-axis 6H SiC by CVD in a temperature range of 1200 - 1600 °C for 10 to 300 s. Before the growth, mesas were formed on the substrate by photolithography and reactive ion etching. The lateral advance of these tables was measured after growth and related to the diffusion length  $\lambda_s$ . The authors compared their model to the one of Nishizawa and Kimura and found a difference in the diffusion length of almost one order of

## 2.4 Conclusion on the on-axis growth of SiC

magnitude. However, the tendency of the diffusion length as a function of the temperature is similar in both cases.

The approach of Nishizawa and Kimura assumes that all adsorbed atoms are incorporated into the nuclei and neglects thus desorption. This might be true for low temperature processes but not for the PVT growth. Moreover, a direct relation between surface diffusion length and nuclei density cannot be established as easily as proposed by Nishizawa and Kimura. Calculations of Halpern showed that the mean nuclei distance can be much larger or smaller than the surface diffusion length [68]. Although a noticeable difference of the next nuclei distance is found (Fig. 2.18) between Si- and C-face, a derivation of the diffusion length is hence not possible.

The method of Kimoto and Matsunami can be adopted for the CVD process, but it is only hardly employable on the PVT growth. The higher growth rates and temperatures during PVT growth make an exact control of the nuclei step advance difficult. Therefore we conclude, that there is no simple way to access the diffusion length from the nuclei density.

However, due to the observed nuclei distribution we are able to assert that the diffusion length on the C-face is larger than the half terrace width, *i.e.*  $\lambda_s > 3.12 \pm 0.52 \mu\text{m}$ , whereas it is smaller than the half terrace width on the Si-face, *i.e.*  $\lambda_s < 3.28 \pm 0.21 \mu\text{m}$ . These results show the same tendency as published by Matsunami *et al.* [67].

## 2.4 Conclusion on the on-axis growth of SiC

In this chapter various aspects of the on-axis SiC growth were discussed. The crystal growth rate can be either limited by the vapour transport or by the surface diffusion and incorporation of adatoms on kink sites. We observed that the growth rate is almost inversely proportional to the pressure in the reactor and concluded that the growth is limited by the vapour phase transport. Due to an advective flow this inverse dependency is modified.

Nucleation is an unwanted process that is nevertheless randomly observed during the growth of SiC. The increased number of nuclei on descending terraces suggests that there is a significant Ehrlich-Schwoebel barrier on the C-face. Furthermore, the nuclei distribution on the spiral terraces also indicates that the diffusion length is larger on the C-face than on the Si-face. The exact surface diffusion length cannot be obtained from the nuclei density in our case.





## 3 Spiral phenomena

This chapter deals with mechanisms related to the growth of spirals on SiC. Although spirals have been thoroughly studied in the last decades, novel results on their growth process on SiC are revealed.

For the first time the growth laws of spirals on SiC are systematically analysed. We will show that the spiral growth law is not only dependent on the spiral type but also on the seed polarity. Furthermore, it is reported that the C-face spirals do not follow any known growth law. Simulations are performed to understand this behaviour.

A dissociation of the top bilayer on C-face spirals was achieved under certain, reproducible conditions. This new kind of spiral structure and its possible origin are discussed.

Before we start the presentation and discussion on the spiral growth mechanism, an insight is given on the surfaces and related spirals typically obtained from the experiments.

### 3.1 Observed spirals

In the following, we will give an overview on spirals usually observed on the SiC crystal surfaces. Furthermore, the shapes of the spirals are discussed.

#### 3.1.1 Spiral types

On our samples, we obtained a huge variety of spiral types and patterns. Most of them were already reported and discussed in the early days of growth spiral research [69] but still not all mechanisms which lead to their formation are understood. The aim of this section is to present the typical spiral patterns obtained by the PVT growth of SiC. In addition, the established models to explain the pattern formation are introduced.

#### Single and double spirals

Simple and double spirals are mainly observed during the initial growth of the crystals on 6H on-axis seeds (Fig. 3.1). The simple spirals consist of one branch with a step height of the unit cell parameter  $c$  or, in case of the 15R polytype, of  $c/3$ . Spirals with step heights larger than  $c$  form an open core and are thus micropipes.

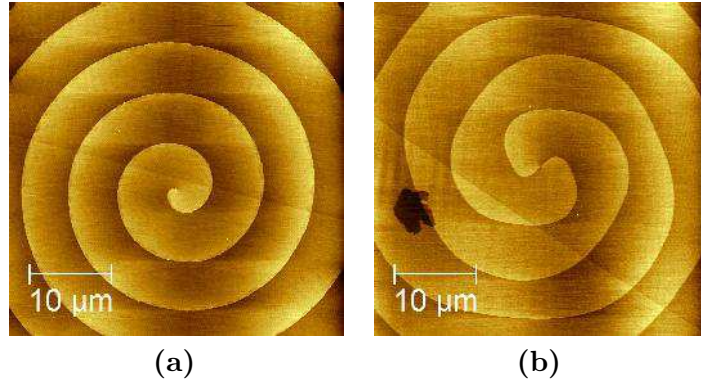


**Figure 3.1:** Simple and double spirals with  $b = 1$  have one or two branches respectively and no hollow core.

The step height of the double spirals is  $7.5 \text{ \AA}$ , *i.e.* their Burgers vector is the same as for 6H simple spiral. Although these spirals were already observed by Amelinckx in 1951 [70], there exists no explanation why there are two different 6H spiral types for the same Burgers vector. The stacking of each branch is 3C but for one branch the tetrahedrons are turned by  $60^\circ$  resulting thus in the ABC ACB stacking [71]. The polygonization of the double spirals in their centre is discussed in chapter 3.1.2.

On the Si-face crystals, mainly spirals of the 6H polytype were observed whereas on the C-face, in addition, 4H and 15R polytypes were present. The Raman spectra of the 4H and 15R spirals of thin crystals always show the fingerprint of the 6H substrate (Fig. 3.2). Occasionally, the fingerprint of 6H, 4H and 15R were measured. By measuring the step height of AFM images, the polytype on the surface can be clearly determined.

The polytype stability is known to be higher on the Si-face than on the C-face [72]. In the literature it is often reported that the polytype on the C-face transforms from 6H to 4H [73][60][74] and less frequently to 15R [75]. Fissel noted that the polytypic transformation is strongly affected by different growth parameters, such as Si/C ratio and substrate temperature [60].

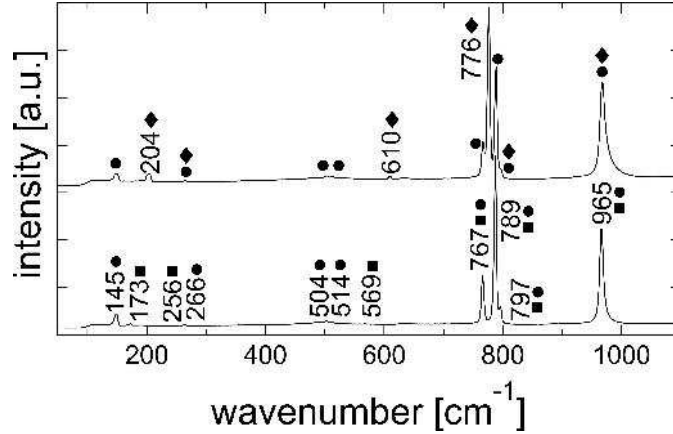


**Figure 3.2:** The Raman spectra of two spirals grown on C-face 6H seeds prove the presence of the 6H (filled circles), 15R (filled squares) or 4H (filled rhombi) polytype. The 6H fingerprint is visible in both cases. Note that some peaks of different polytypes have (almost) the same wavenumber. In such a case only the wavenumber of the 6H polytype is given. All relevant peak positions can be found in the appendix (Tab. C.1).

In some publications it is suggested that the polytypic transformation on the C-face is taking place due to nucleation on the spiral steps [72][65]. Although nuclei are not always visible on the surfaces of transformed crystals, such a mechanism cannot be excluded.

Another possibility is that stacking faults are formed during the growth. A similar mechanism was discussed in detail by Pirouz and Yang for the  $\alpha \leftrightarrow \beta$  SiC transition [29]. According to their model the faulted regions are created by the motion of partial dislocations. They analysed TEM images obtained from thermally treated SiC crystals and related the observed stacking sequences to their model. As they did not consider growth conditions but thermal treatment, their model cannot be directly transferred to our observations. However, it can be concluded that the polytypic transformation can also take place due to the creation of stacking faults.

The total energy differences of various polytypes relative to 3C was calculated with the anisotropic next-nearest-neighbour Ising spin model by many authors [76][77][78][79][80]. Cheng excepted, they all found that the total energy of the 4H polytype is lower than the one of the 6H. Limpijumnong also calculated the energy of the 15R polytype and obtained an even lower energy for the 15R polytype. Hence, it is in favour of the fact that if a polytypic transformation is occurring, either the 4H or 15R polytype can form. The lower surface energy on the C-face probably favours the formation of stacking faults and thus of the 4H and 15R polytype as already suggested in [81].

### 3 Spiral phenomena

The simple and double spirals are further discussed in chapter 3.3, where their growth modes are analysed in detail.

#### **Micropipe formation**

In 1951 Frank proposed the existence of micropipes [35]. This defect is a screw (or mixed) dislocation with a large Burgers vector. Due to the high strain at the centre of such a dislocation, the atoms in the core are evaporating leaving thus an empty tube at the dislocation line behind.

Micropipes are observed in many different crystals, such as GaN [82], mica [83], ZnS [84] and SiC [85]. Although micropipes are known now for more than 60 years, there is still no generally accepted model explaining their formation.

Nevertheless, the amount of micropipes in commercial wafers has been drastically decreased over the last years by optimizing the growth parameters. While the micropipe density remained constant at  $10 \text{ cm}^{-2}$ , the diameter of commercial wafers increased from 50 (2") to 100 mm (4") between 1999 and 2009 [86][1]. At the present time, wafers with zero micropipe density are available from Cree [20]. Despite the progress in micropipe reduction, there is still a scientific interest in this kind of defect, especially concerning the origin of the micropipes.

A key problem is the understanding of the initial micropipe formation. There exist many models trying to explain the origin of micropipes. For instance, it was observed that micropipes nucleate on inclusions of silicon or carbon [87][62]. The overgrowth of the inclusions results in a lattice mismatch and hence a micropipe. Another model is that high axial temperature gradients cause stress in the crystal and thus the formation of micropipes [88]. Furthermore, it was proposed that stacking fault clusters cause micropipes [89] or the coalescence of different domains [90]. The problem of all these theories is, that they can only explain the micropipe formation for a special case. It seems, that there is no general model to describe the origin of micropipes.

On our samples we sometimes observed the agglomeration of spirals with likewise signs (Fig. 3.3), some of them forming a micropipe (Fig. 3.3 (a) and (e)). This is remarkable, since dislocations with opposite Burger vector signs annihilate whereas those with same sign repel each other [33].

Once a micropipe is present it grows by absorbing other dislocations with likewise sign in its vicinity. According to Pirouz the net force  $F_{net}$  between a dislocation and a micropipe is [91]

$$F_{net} = \frac{Gb^2}{2\pi(d+r)} \frac{nd^2 + 2ndr - r^2}{d(d+2r)} \quad (3.1)$$

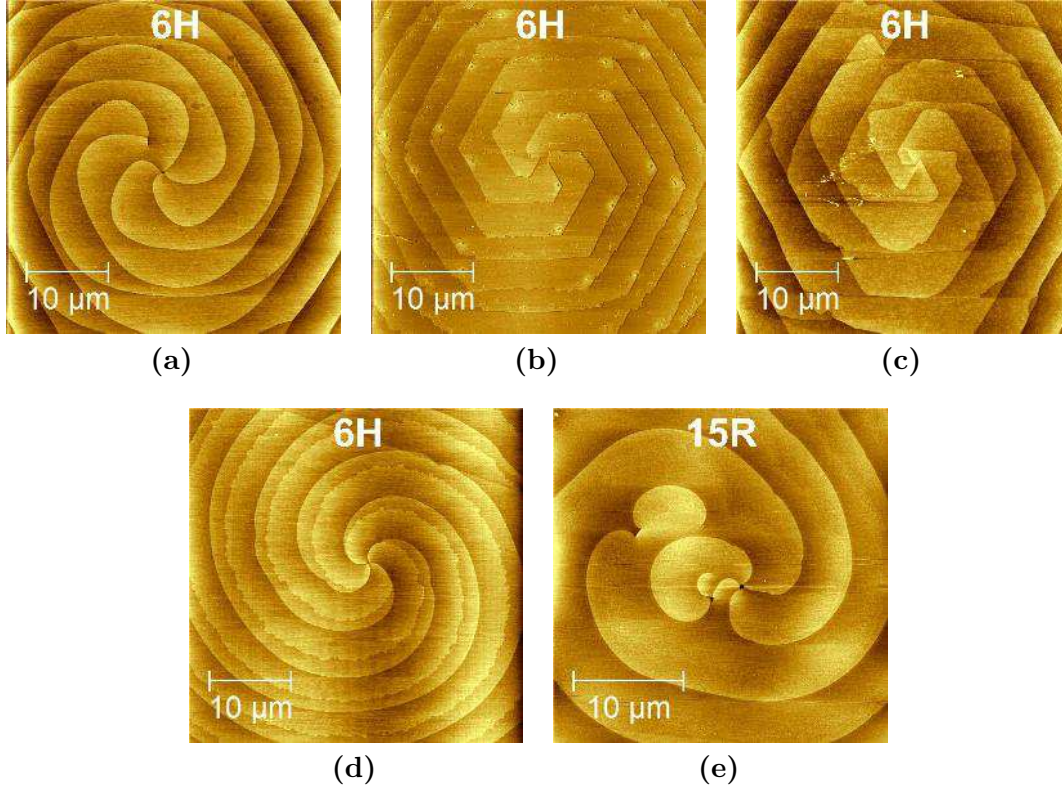


**Figure 3.3:** Spirals with likewise sign agglomerate and may form a micropipe. On these images two or more spirals are present.

where  $G$  is the shear modulus,  $b$  the Burgers vector,  $r$  the radius of the empty micropipe core,  $d$  the distance between the dislocation and the surface of the empty micropipe core and  $n$  the magnitude of the micropipe.

The force between dislocation and micropipe is attractive if [91]

$$\frac{d}{r} < \left( \frac{n+1}{n} \right)^{1/2} - 1. \quad (3.2)$$

Due to the high growth temperatures, the mobility of the dislocations is sufficiently large to reach micropipes far away of their origin. Apparently, the forces between two dislocations without empty core ( $r = 0$ ) are always repulsive. Therefore, we suggest that screw dislocations with likewise signs can overcome the repulsive forces at high growth temperatures and thus form a micropipe.

### Frank-Read source

### 3 Spiral phenomena

The Frank-Read source is usually known in the context of dislocation multiplication [92]. A dislocation can be pinned on precipitations, inclusions or at intersections with other dislocations for example. In such a case, the dislocation is immobile only at this position. If a dislocation is pinned at two points, the application of shear stress will result in glide of the segment in-between (Fig. 3.4). First, the line will bow and then bend around the pinned points A and B (Fig. 3.4 (b) - (d)). Finally, the dislocation segment annihilates at m and n due to different signs of the Burger vectors (Fig. 3.4 (e) and (f)). A closed loop detaches and propagates through the crystal leaving a dislocation segment between A and B behind. As a consequence, this mechanism is in principle regenerative and can be repeated after each loop but since every loop reduces stress in the crystal, the actual number of loops will be limited [69].

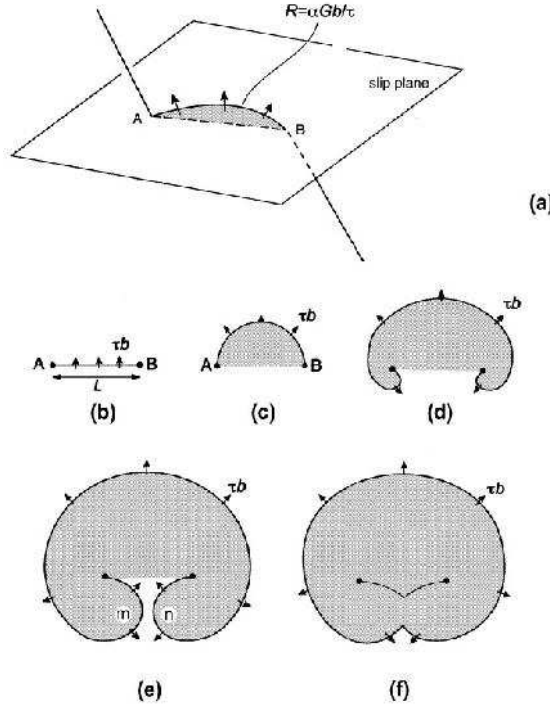


**Figure 3.4:** The Frank-Read mechanism of dislocation multiplication. Image taken from [33].

The same process can take place at the surface of growing crystals when growth spirals are present [48]. Two spirals with opposite signs create closed loops during growth if the distance between the centre of both spirals is larger than  $2\rho_c$ , *i.e.* twice the critical radius. If the distance is smaller than  $2\rho_c$  the dislocations will annihilate.

Fig. 3.5 shows some examples of Frank-Read sources observed on our samples.

### 3.1 Observed spirals

Depending on the growth progress, only a straight line ((c), hardly visible), or bended steps, as on the other images, are visible. Furthermore it can be noticed, that a single Frank-Read source creates a wedding cake like structure.

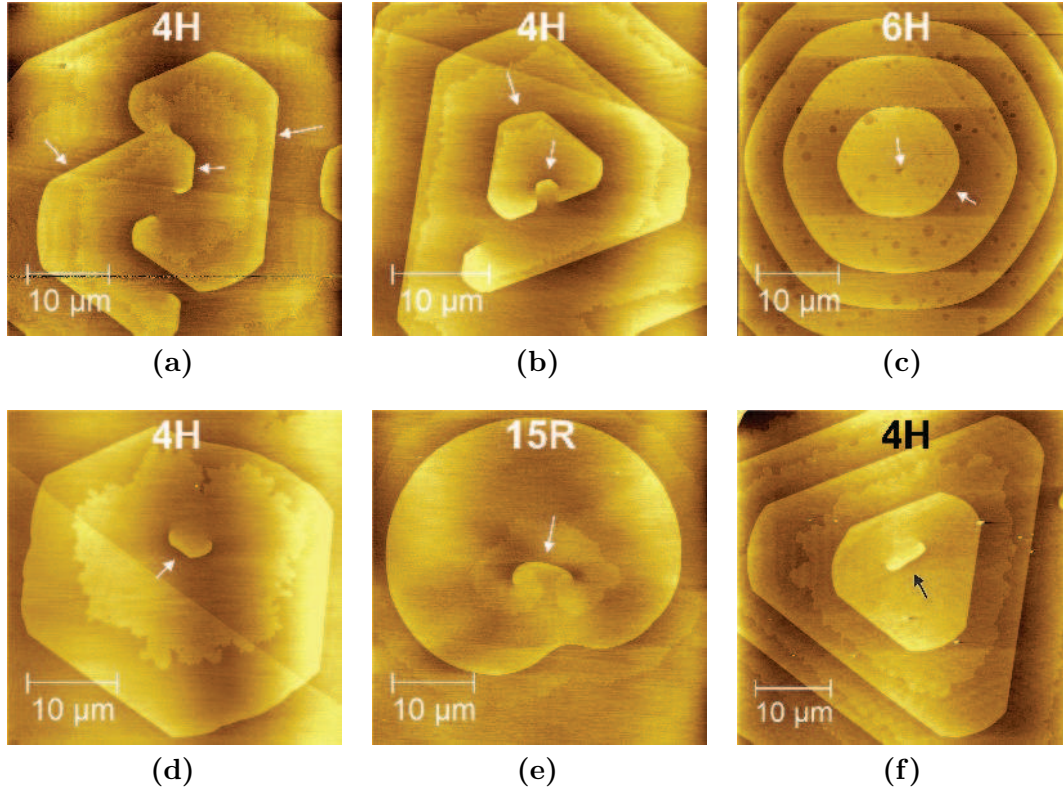


**Figure 3.5:** Two spirals with different sign create a Frank-Read source. When the steps of two closely located spirals meet, a joint step is created which results in a loop upon crystal growth. The joint steps are indicated by arrows.



### 3 Spiral phenomena

#### Spiral agglomeration

In many cases, an agglomeration of spirals on single domains was observed in this work as shown in Fig. 3.6. On the one hand, the surface structures of such a spiral agglomeration can be complex. On the other hand, the shapes on the surface can be broken down into interactions of spirals with likewise and opposite sign.

As previously mentioned, spirals with likewise signs tend to arrange around a centre and may form micropipes during further growth of the crystal. The arrangement of those spirals is visible in Fig. 3.6 (b), (c) and (d) (on the left side). Also a parallel alignment is possible as in Fig. 3.6 (d).

Spirals with opposite signs form Frank-Read sources, often over a wide distance (centre to centre distance larger than  $20\text{ }\mu\text{m}$ ).

The mixture of many spirals of these types result in the surface structures shown in Fig. 3.6.

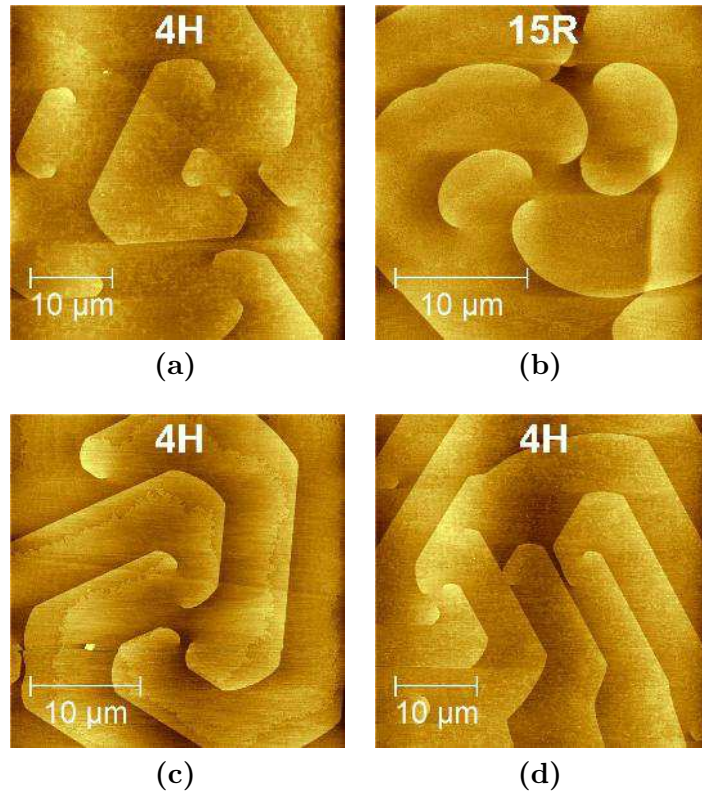


**Figure 3.6:** If many spirals are agglomerated, complex surface structures are formed.

### 3.1.2 The shape of the spirals

The shape of growth spirals can vary from strongly polygonized (Fig. 3.7 (a)) to perfectly round (Fig. 3.7 (d)) as it was already reported in the first publications on spirals [85][69].

On our samples the spiral shape seems to depend mainly on the polytype. The 15R spirals are always roundly shaped, the 4H spirals are strongly polygonized, the 6H simple spirals are slightly and the 6H double are more polygonized than the simple but less than the 4H spirals.

Several authors discussed the spiral shape and they all agree that the advance rate of the spiral steps is determining the shape [69][93][94][71][95].

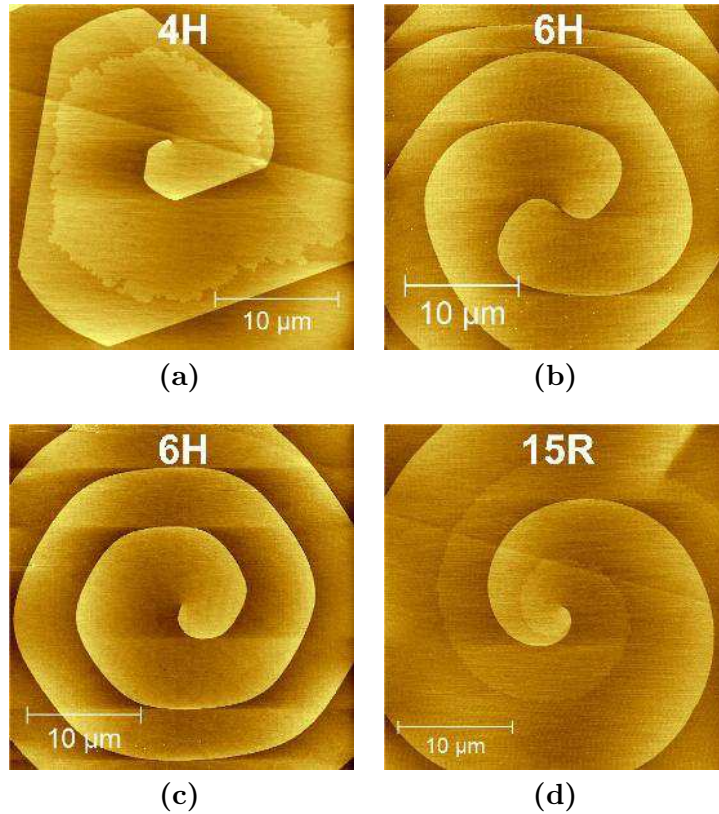


**Figure 3.7:** The degree of polygonization clearly depends on the polytype: (a) 4H (C-face), (b) 6H double (Si-face), (c) 6H simple (Si-face), (d) 15R spiral (C-face).

Amelinckx proposed that the polygonization of a spiral depends on the kink density at an edge [69]. This density is unequal for the different step orientations. If the surface diffusion length is small, a polygonized spiral results as the low kink density on some steps reduces their velocity. On the contrary, a roundly shaped

### 3 Spiral phenomena

spiral is obtained if the diffusion length is large. Then, all adatoms reach a kink site. This reasoning cannot explain why the degree of polygonization varies with the polytype. On the C-face, 4H and 6H (simple and double) spirals are polygonized while 15R spirals are perfectly round. If the degree of polygonization was related to the number of kink sites, the 15R polytype should be also polygonized. This is regardless of whether the number of kink sites scales with the step height or not, as the number of bilayers of the 15R polytype is in-between the 4H and 6H type. Therefore, the explanation of Amelinckx can be excluded here.

Sunagawa suggested that the step roughness modifies the step velocity and hence the spiral shapes [95]. The roughness of surface or step can be defined by the Jackson factor  $\alpha$  [96][18]

$$\alpha = \left(\frac{w}{u}\right) \frac{\Delta H}{k_B T_m} \quad (3.3)$$

where  $w$  is the number of next neighbouring adatoms on the growing face,  $u$  the number of next neighbouring atoms in the crystal,  $\Delta H$  the enthalpy of crystallization and  $T_m$  the melting temperature of the crystal. The smaller  $\alpha$  the rougher is the step.

According to Sunagawa a small  $\alpha$  (rough step) results in an isotropic step advance rate and thus a round spiral. The spiral is polygonized for large  $\alpha$  (smooth step). It is argued that the strong bondings in the plane are responsible for the step roughness and hence for the degree of polygonization. If the bondings are rather weak the step is rough and the spiral roundly shaped.

This approach is non-satisfying for the spirals we observed since their shape is determined by the polytype. This cannot be explained by the step roughness and the Jackson factor which only considers material constants and indirectly growth conditions (via  $w$ ).

Let us have a closer look on the parameters entering the step velocity. Replacing  $\rho_c$  in the previously defined step advance rate (Eq. 1.28) by the definition from Eq. 1.24 results in

$$v(\rho) = v_s \left(1 - \frac{\kappa a^2}{k_B T \sigma \rho}\right). \quad (3.4)$$

From this equation it follows that there are two possible reasons for anisotropic spirals [71]. Either the advance rate of a straight step  $v_s$  is anisotropic. Then, the anisotropy of the spiral is maintained all over its domain. Moreover, the specific edge energy  $\kappa$  can be anisotropic. In this case, the polygonization diminishes with increasing distance to the centre. This is what we observe as shown in Fig. 3.8.

In case of an isotropic advance rate  $v_s$  a spiral is polygonized if the expression in the brackets of Eq. 3.4 is smaller than unity ( $1 - \kappa a^2 / (k_B T \sigma \rho) < 1$ ), *i.e.* there is

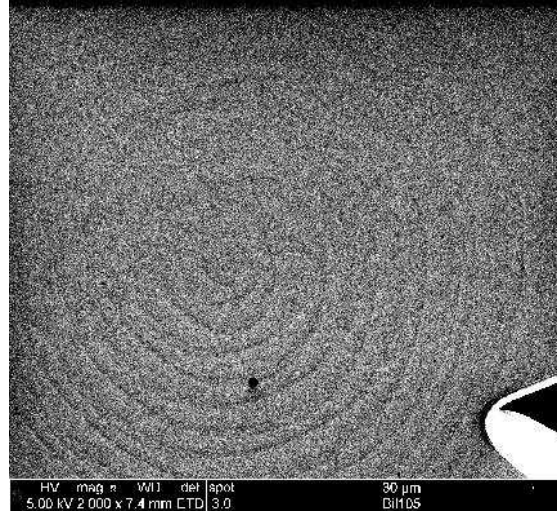


**Figure 3.8:** The polygonization of a 6H double spiral on the C-face decreases continuously with increasing distance to the centre.

a strong anisotropic effect of the curvature. The spiral approaches a round shape if the expression in the brackets is close or equal to unity ( $1 - \kappa a^2 / (k_B T \sigma \rho) \approx 1$ ) [71]. The radius of curvature is increasing by every spiral turn and hence the influence of an anisotropic specific edge energy is continuously diminished.

Previously  $a$  was defined as first neighbour distance of atoms on a step. This definition is true for monoatomic steps but in case of spirals with step heights of several atomic layers  $a$  corresponds to the step height [95]. Thus it is evident that the degree of polygonization of a spiral increases with decreasing step height. This is what we observe for the 4H (step height 10 Å) and 6H spirals (step height 15 Å).

In addition, from Eq. 3.4 it follows that the specific edge energy also plays a role. Yet, we do not assert any effect of the specific edge energy as the polygonization of simple 6H spirals is similar on Si- and C-face (Fig. 3.16 and 3.18). Therefore, either the edge energies are similar or its influence on Eq. 3.4 is too small to observe it experimentally.

Regarding Eq. 3.4 it follows also that the temperature or supersaturation affect the degree of polygonization. The observed spiral shapes are similar for spirals of the same polytype but the polygonization is slightly increasing with increasing pressure and hence decreasing supersaturation (see Fig. 3.16, 3.17 and 3.18).

The presented mechanisms and parameters are not responsible for the shape of the 15R spirals. Another possible origin for the round shape of the 15R spirals could be the particular stacking of this polytype. The step height of spirals of this polytype is 12.5 Å which corresponds to 5 bilayers. Therefore three spiral turns are necessary to complete the unit cell. If we assume that the bilayer stacking

### 3 Spiral phenomena

of the first 5 bilayers is ABCBA, it follows that after one spiral turn a forbidden stacking sequence would occur (ABCBA ABCBA) since two bilayers of the same type are stacked on each other. This is not possible due to the direction of the bondings [29]. As a consequence, the atoms must slip after one spiral turn and create thus a stacking fault [97][98]. This is illustrated in Fig. 3.9. The stacking sequence ABCBA winds up around the dislocation core and after a full turn the atoms must slip from A to B, B to C and C to A. The previous considerations pointed out that the anisotropy of the specific edge energy is responsible for the polygonization. The stress field in the basal plane caused by the partial dislocation is proportional to the magnitude of the Burgers vector  $b$  and inversely proportional to the distance  $r$  ( $\sigma_{xx} \propto b/r$ ) [33]. Therefore it is conceivable that the specific edge energy is modified by the stress field of the partial dislocation losing thus its anisotropy.

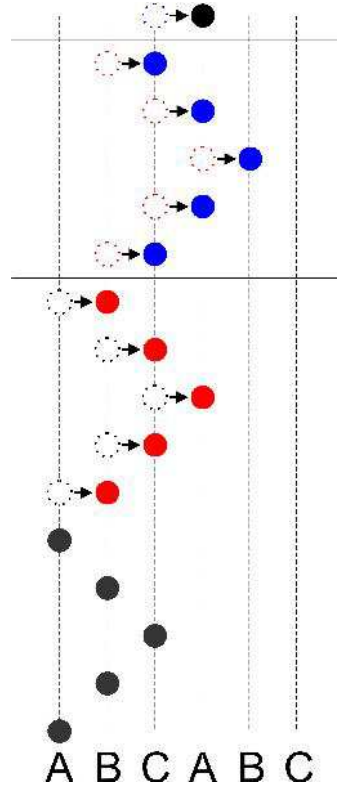


**Figure 3.9:** The particular stacking of the 15R polytype requires the creation of a partial dislocation on each spiral turn.

On the polygonized 4H spirals two different facets can be distinguished which are both alternating (Fig. 3.7 (a)). One facet is straight and longer than the second type which is also roundly shaped. The expected shape of a hexagonal polygonized

### 3.1 Observed spirals

spiral is illustrated in Fig. 3.10. In this figure it is assumed that the advance rate of each facet is the same resulting in a continuous increase of the facet lengths [48][94]. Hence, it can be concluded that the advance rate of the alternating facets of the observed 4H spirals is unequal. As their shape does not correspond to the one shown in Fig. 3.10 the term irregular hexagonal polygonized spirals is used for them.

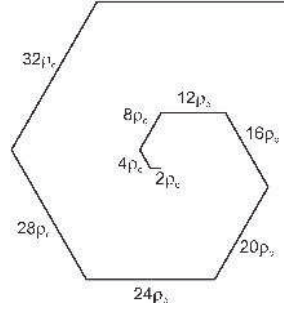


**Figure 3.10:** If the advance rate is the same for all steps of a hexagonal polygonized spiral, the length of each facet should increase continuously.

The unequal step advance rate might be caused by anisotropic diffusion rates, a mechanism which we present in the following.

Ogura *et. al.* grew Au islands on Ir(111) and Pt(111) surfaces<sup>1</sup> and observed dendritic and triangular islands [57]. The authors related the island shape to the substrate symmetry. The threefold symmetry of the fcc (111) substrates results in a triangular shape of growing islands due to anisotropic corner diffusion rates.

Such a mechanism is also conceivable in the case of 4H SiC. There are several possibilities to form the 4H polytype by arranging its bilayers. There is either a cubic sequence followed by a hexagonal bilayer (*e.g.* **ABCB**) or first the hexagonal bilayer with a cubic sequence on it (*e.g.* **BABC**). The latter case is illustrated in Fig. 3.11 and will be discussed in the following.

Let us assume a step on a (0001) plane as illustrated in Fig. 3.12. This image does not correspond to the real case of a SiC step as only a monoatomic step is drawn but it can be assumed that the surface process remains similar. Furthermore, we suppose that the first bilayer of the step is the one with the slowest advance rate and that this bilayer hence controls the total step advance. The adatom *C* at the corner can either diffuse towards the A or the B step. The diffusion of this atom depends on the barriers  $E_{ca}$  and  $E_{cb}$ . If both barriers are equal both steps advance with the same velocity. The barriers can also be different and then it is clear that the adatoms at the corner preferably diffuse in direction of the lower

<sup>1</sup>The crystal structure of Au, Ir and Pt is fcc.



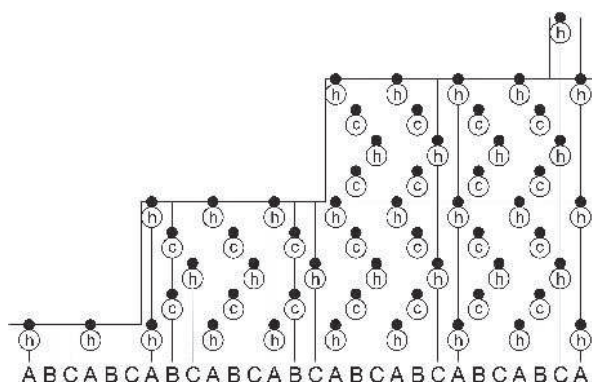


**Figure 3.11:** One possible stacking of the 4H polytype (BABC). The three top bilayers are arranged as for the cubic polytype.

barrier, increasing hence the growth rate of this step. The shape of the new layer is therefore hexagonal for equal and triangular for unequal corner diffusion barriers, as for example shown in [99][57].

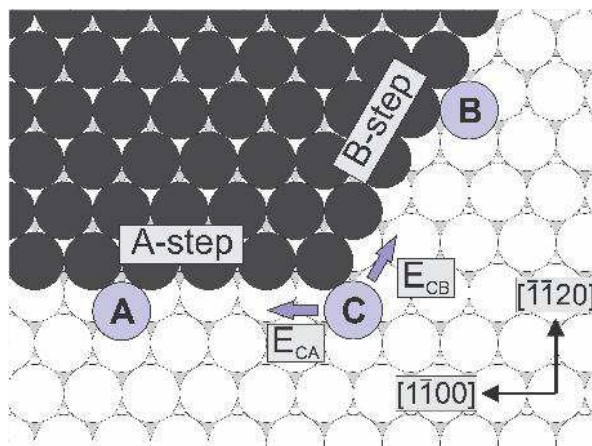


**Figure 3.12:** Depending on the stacking, the diffusion rate from the corner to an A or B step might be different. Image adapted from [57].

Following the reasoning of Ogura *et al.* we suppose that the particular BABC stacking of the 4H polytype causes an anisotropic corner diffusion barrier. If a new layer grows on this kind of stacking, the symmetry of the first bilayer is hexagonal but the three bilayers below (and also above) are stacked as in a fcc crystal. The threefold symmetry of these bilayers (triangle in Fig. 3.13) is imposed on the on-growing layer and hence affecting its actual hexagonal symmetry. The change of the hexagonal spiral shape towards a triangular one is probably due to the anisotropic corner diffusion, introduced above.

Since the diffusion barriers are related to the atomic configuration, we assume

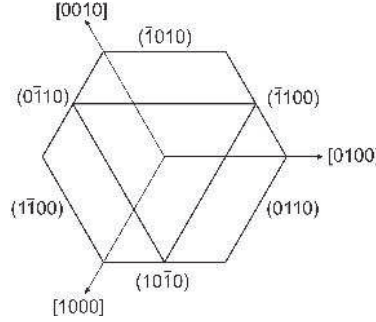


**Figure 3.13:** The hexagonal shape is expected for a spiral with symmetric edge diffusion barriers. For an increasing difference of this barrier the shape will pass from an irregular hexagon into a triangle.

that these barriers are proportional to the specific edge energy. Therefore, the decreasing polygonization with increasing radius of curvature can be explained by Eq. 3.4.

## 3.2 Growth rate of micropipes

During the growth of C-face SiC crystals it seemed that the micropipe growth is of higher importance than on the Si-face. For the same deposition time of two hours on both faces we noticed that on the C-face almost always all spirals were overgrown by the micropipe spirals. In contrast, the Si-face crystals were still covered by growth spirals.

Fig. 3.14 shows the surfaces of crystals grown on a Si-face and a C-face seed. The growth conditions were similar in both cases, *i.e.* two hours crystal growth at 50 mbar. Mainly on the upper part of the Si-face crystal domains, marked by D, are visible. The domains are irregularly shaped and limited by black lines (the domain boundaries). Each domain contains at least one growth spiral, which can be seen at higher magnifications. On the C-face, stripes oriented along the crystallographic axes can be seen. These stripes originate from micropipes, indicated by M in the image. Domains, as in the case for the Si-face crystal, are not present.

The problem of accumulated spirals with likewise signs has already been discussed in literature [5][48]. If there are  $n$  dislocations either aligned on a straight line with length  $L$  or in a circle with perimeter  $L$  the resulting terrace width  $x_0$  can be expressed by [48]

$$x_0 = \frac{\Lambda}{n'} \quad (3.5)$$



### 3 Spiral phenomena

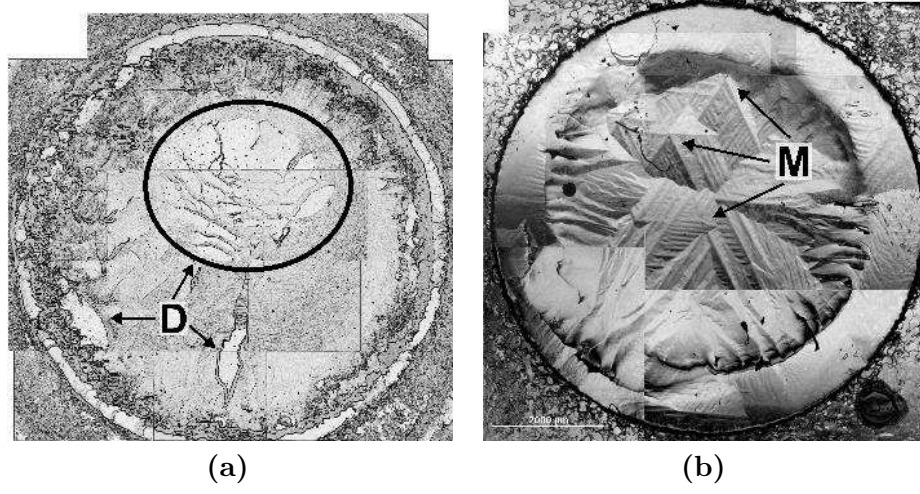


**Figure 3.14:** DIC microscopy images of (a) a **Si-face** and (b) **C-face** crystal surface. The Si-face image was post-processed to enhance the contrast of the domains. The D indicates spiral domains while M is indicating micropipes. The diameter of the growth area is 0.7 mm.

where

$$n' = n \left( 1 + \frac{L}{\Lambda} \right)^{-1} \quad (3.6)$$

and  $\Lambda$  corresponds to the terrace width of a simple spiral.

There are two limiting cases for Eq. 3.5. If the dislocations are widely spaced ( $L \gg \Lambda$ ) then the terrace width becomes [48]

$$x_0 = L/n. \quad (3.7)$$

Hence, the terrace width is independent of the supersaturation. In the second limiting case, the dislocations are closely accumulated ( $L \ll \Lambda$ ) and it follows that [48]

$$x_0 = \Lambda/n. \quad (3.8)$$

The width is a function of the supersaturation, which enters into the equation via  $\Lambda$  (Eq. 1.32,  $\Lambda \propto 1/\sigma$ ).

As mentioned before, a micropipe is a screw dislocation with a large Burger vector. An empty core is formed in the centre to reduce the strain energy. The micropipe is now regarded as an accumulation of  $n$  simple spirals originating from an empty core with diameter  $L$  (*i.e.*  $L \ll \Lambda$ ). Replacing  $\Lambda$  in Eq. 1.34 by  $x_0$  from

### 3.2 Growth rate of micropipes

Eq. 3.8 results in

$$R_m = nR \quad (3.9)$$

where  $R_m$  is the growth rate of a micropipe with  $n$  branches and  $R$  the growth rate of a simple spiral.

As a consequence of the latter equation, micropipes will always overgrow simple spirals due to the linear scaling of the growth rate with the number of branches. The faster growth of spirals with larger Burgers vector was experimentally shown by Chernov [100]. He measured the growth rate of spirals on  $\beta$ -methyl naphthalene crystals with Burgers vector of  $4c$ ,  $40c$  and  $60c$  and reported a significant increase in growth rate with increasing Burgers vector.

The overgrowth of a domain is shown in Fig. 3.15. The black arrows are indicating the direction of the lateral growth. This direction can be either identified by AFM images or by regarding the step structure of microscope images. If a step encounters a particle or emerging dislocation the step advance is locally lowered resulting in bulges (visible on the lower left of Fig. 3.15 (a)). On AFM images high points are bright whereas low points are dark. From Fig. 3.15 (c) it follows that steps are overgrowing the visible spiral from the lower left. These images are illustrating that domains can overgrow other domains and that steps of micropipes are overgrowing domains containing closed core spirals.

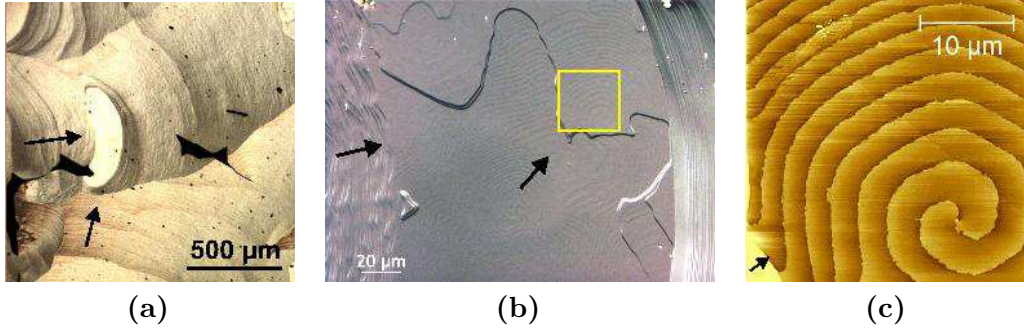


**Figure 3.15:** Spirals are overgrown by micropipes or by domains with accumulated spirals. The AFM image (c) corresponds to the area marked by the yellow square in (b).

But why is the micropipe growth on the C-face of higher importance than on the Si-face? As the growth rate scales with  $n$  on both faces comparably, the derived equation does not give an answer to this question. Another explanation might be the origin of the wafers. The Si- and C-face wafers used for the experiment were produced by different companies. Therefore it is conceivable that although the

### 3 Spiral phenomena

density of defects is similar on both wafers, the amount of micropipes is higher on the used C-face substrates.

Due to the different growth behaviours, the deposition time was adjusted to the pressure on the C-face. Hence, the deposition time was reduced with decreasing pressure.

## 3.3 Spiral growth modes

The access to growth parameters is limited during the PVT growth of SiC. Controllable parameters are crucible geometry, temperature and pressure. The supersaturation, which is the determining factor for the growth process, is inaccessible. Furthermore, in-situ observation of the crystal surface, as for other growth techniques [10], is not possible.

As detailed in chapter 1.4.3, the supersaturation can be indirectly estimated via the growth rate and spiral terrace width. In addition, the growth law can be determined from these two quantities.

In the following an ex-situ analysis of the growth spirals is performed. We will show, that there are fundamental differences between the spirals on the Si- and C-face. This is ascertainable by the spiral shapes and their growth laws. Simulations are performed to confirm our experimental findings.

### 3.3.1 Experimental details and analysis

#### Growth process

The growth process was described before in chapter 2.1.2. The deposition time was always two hours for Si-face substrates, except for the sample grown at 400 mbar. Due to the low growth rate at this pressure the deposition time was increased to four hours. On the C-face the growth rate had to be varied in a wide range in order to avoid the overgrowth of simple spirals by micropipes (see chapter 3.2). Thus, the deposition time was set between 15 min at 50 mbar and 60 min at 400 mbar.

#### Surface characterization

The surfaces of the crystals were first analysed by DIC microscopy to pre-select growth spirals. Then, an image of the spiral centre was taken by AFM in order to verify that the spiral is either of the simple or double type. The spiral types are discussed in the next section. The scan size varied between 20 and 40  $\mu\text{m}$  depending

on the domain size or particles on the surface. Although the spiral polytype can be determined by its step height from AFM images, Raman spectroscopy was performed additionally in order to identify the polytype without any doubt. The crystal thickness was measured by a micrometer dial gauge.

#### Spiral choice

For the analysis of the shape, only simple and double 6H spirals were considered on the **Si-face**. Simple spirals have one branch and their step height corresponds to the  $c$ -lattice parameter ( $15 \text{ \AA}$ ) of the 6H polytype. Fig. 3.16 shows one simple spiral of each sample taken into consideration for the analysis.

The branches of double spirals are both leaving from the centre and the height of each branch is  $c/2$  ( $7.5 \text{ \AA}$ ). Hence, the  $c$ -component of the Burgers vector is the same for 6H simple and double spirals. Some exemplary double spirals are shown in Fig. 3.17.

On the **C-face** mainly simple 15R spirals were present (Fig. 3.19). In addition, 4H spirals were found occasionally which were often interlaced. 6H spirals were observed rarely and in most cases also interlaced. Therefore mainly 15R spirals with a step height of  $c/3$  ( $12.5 \text{ \AA}$ ) and additionally some simple 6H spirals were analysed on the C-face (Fig. 3.18).

### 3 Spiral phenomena

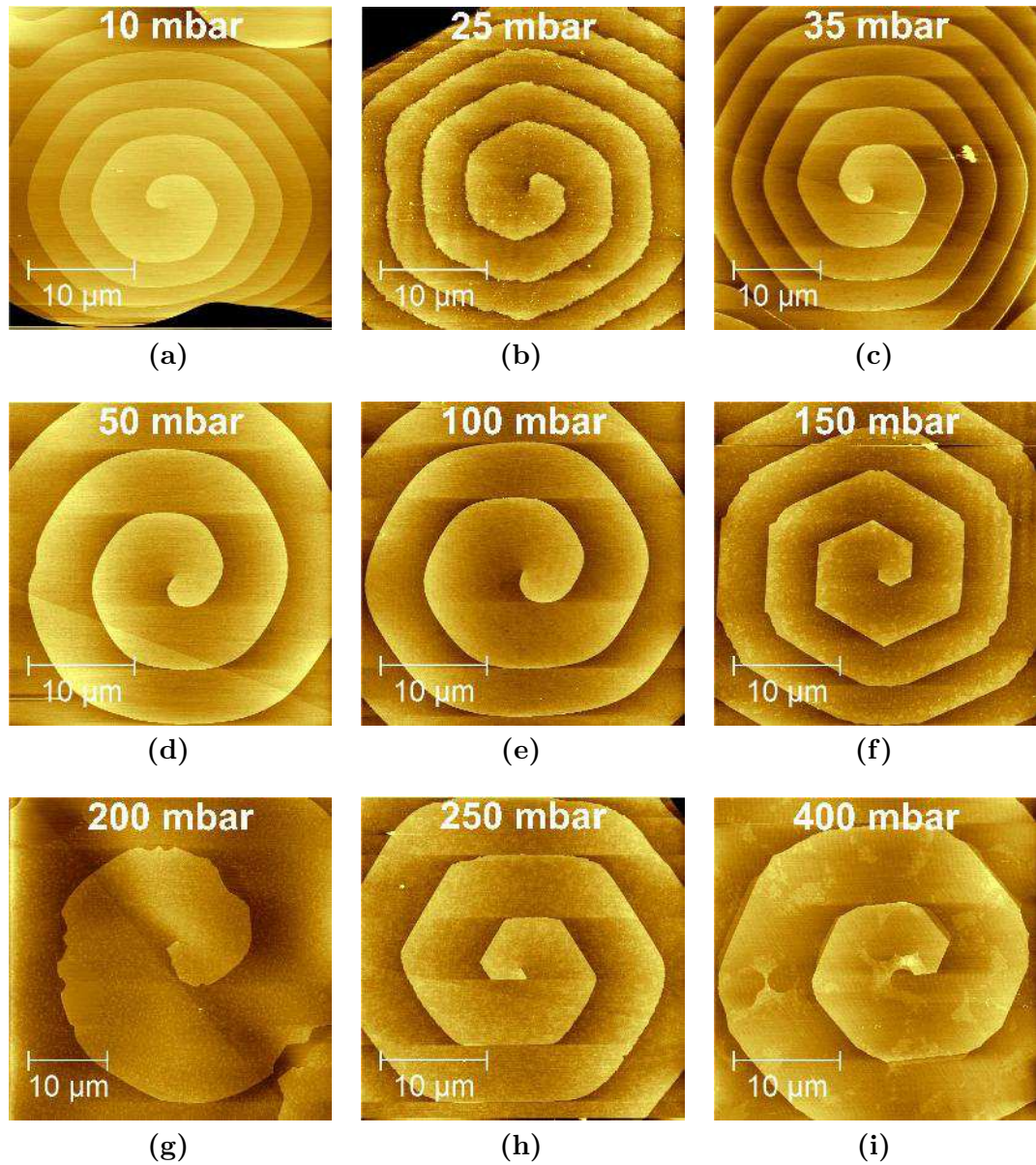


**Figure 3.16:** Simple 6H spirals observed on the Si-face crystal surfaces.



### 3.3 Spiral growth modes

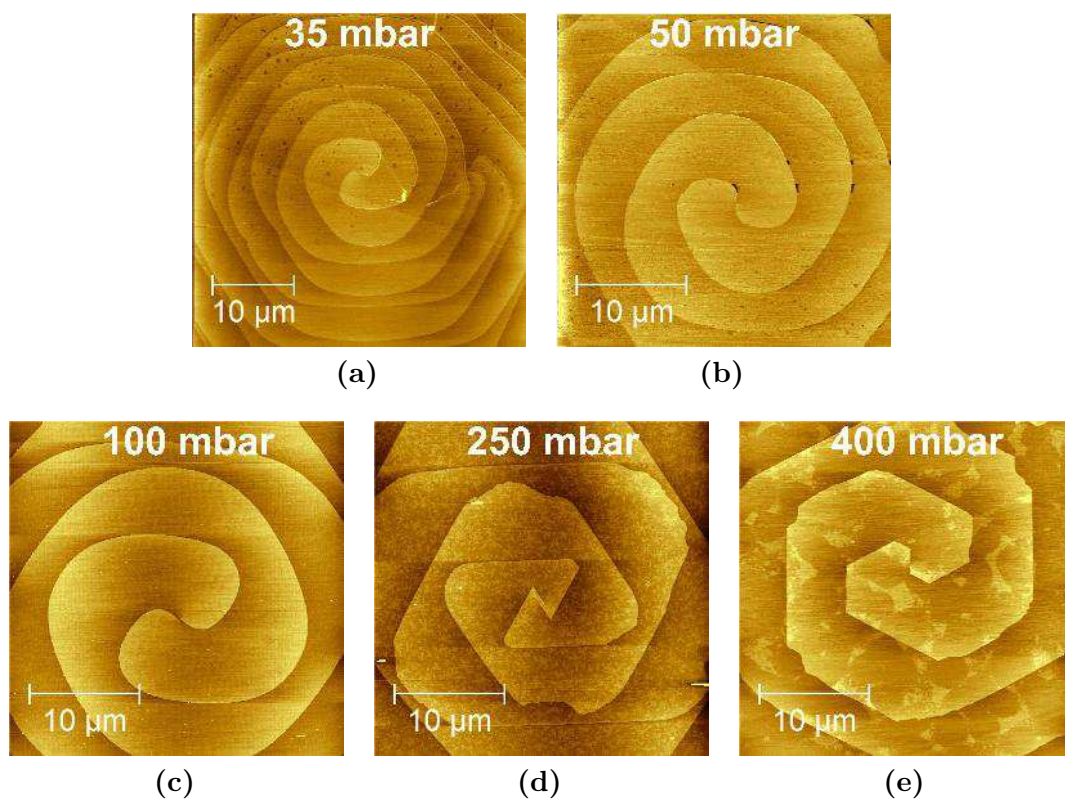


**Figure 3.17:** Double 6H spirals consist of two branches leaving from the centre.

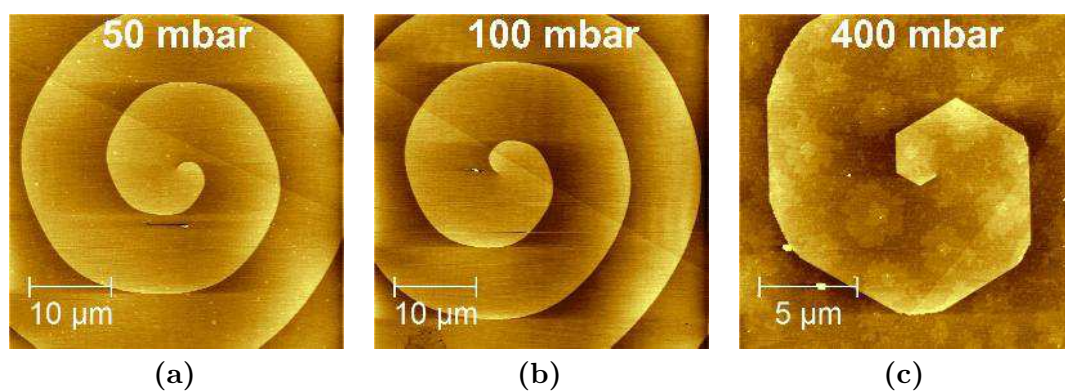


**Figure 3.18:** Simple 6H spirals were only rarely observed on the C-face.

### 3 Spiral phenomena

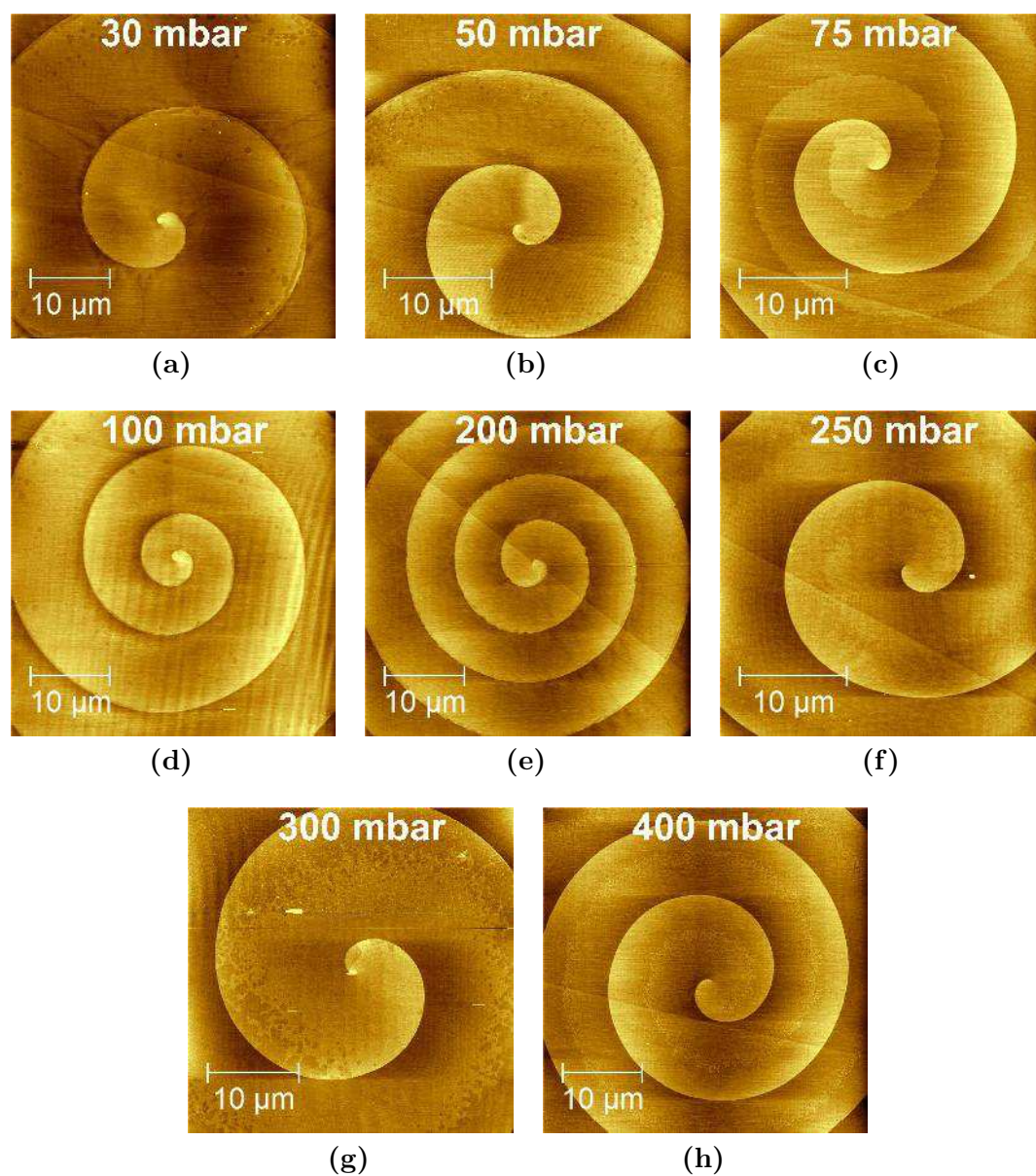


**Figure 3.19:** Most simple spirals on the C-face were identified as 15R polytype.

#### Spiral analysis

From the AFM and DIC microscopy images the spiral profiles and average terrace widths were extracted.

The AFM images were used to measure the terrace width as a function of the spiral turns close to the emergence point of the dislocation (Fig. 3.20(a)). The average terrace width and standard deviation of each sample was calculated for the simple spirals on the Si-face, excluding the first and second turn. The terrace width usually approached a constant value after a few turns.

In addition the maximum terrace width, which was usually observed within the first turns, was determined and also averaged for each sample. The terrace width of the double spirals on the Si-face and of the spirals on the C-face were never observed to be constant. Therefore only their maximum terrace widths were measured and averaged.

Furthermore, the terrace width was measured on DIC microscopy images outside the spiral centres after each spiral turn in the direction with the largest distance to a domain boundary (Fig. 3.20(b)). With the data from the AFM and DIC images spiral profiles were created.

In total, 33 simple spirals on nine Si-face samples and ten double spirals on five Si-face samples were analysed. On the C-face, 37 simple 15R spirals on eight samples and ten simple 6H spirals on 3 samples were analysed.

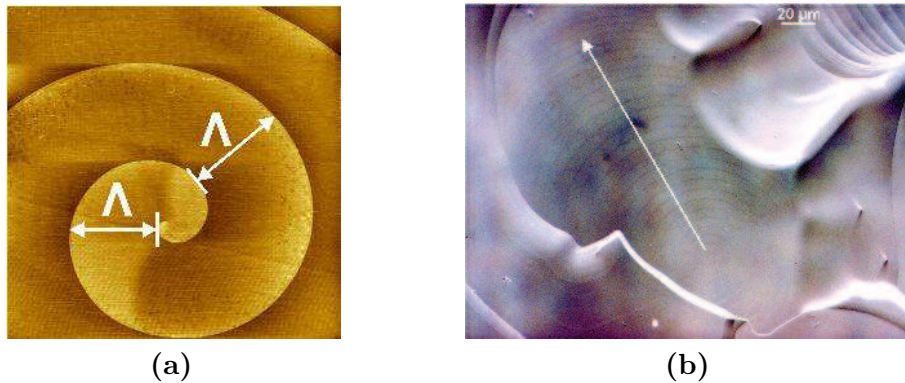


**Figure 3.20:** (a) The terrace width  $\Lambda$  was measured on the AFM images as indicated by the white arrows. (b) The images from the DIC microscopy were used to extract the terrace width in one direction on the domain (along the white arrow).



### 3.3.2 Results and discussion

#### Profiles from experiment

The spiral profiles shown in Fig. 3.21 are essentially different for the simple spirals on the Si-face and the C-face.

The terrace width of the simple spirals on the Si-face increases within the first spiral turn. Then, the width is decreasing within the two following turns and approaching a constant value. The higher the deposition pressure is, the less pronounced the peak in the centre becomes. In addition, the average terrace width increases with increasing pressure.

Also on the C-face, the terrace width is increasing first but the maximum is only reached after two to four turns. Moreover, the width is then decreasing continuously and contrary to the Si-face no plateau is observed. There is no tendency of the terrace width on the pressure.

The profile of the double spirals on the Si-face is a mixture of the two shapes observed for the simple spirals on the C- and Si-face. The terrace width sharply increases within the first turn and decreases continuously afterwards. This decrease is less pronounced than on the C-face, nevertheless, the terrace width does not approach a constant value.

According to the BCF theory, the terrace width of a growth spiral is expected to be constant for a given supersaturation and temperature (compare with Eq. 1.32). Hence, regarding the spiral profiles, two questions arise:

1. Why is there an increase and decrease of the terrace width on the Si-face within the first two spiral turns?
2. Why is the terrace width on the C-face and for the double Si-face spirals not approaching a constant value?

The second question will be discussed in the simulations part at the end of this section. Here, we will first focus on the maximum that appears within the first spiral turns.

A process that can change the spiral shape is the back stress, or back force effect [7][48]. If the surface diffusion length is small, *i.e.* the diffusion fields are nowhere overlapping (Fig. 3.22 (a)), only adatoms not farther away than the diffusion length are incorporated at a spiral edge. At the middle of the terrace the concentration  $c_0$  is defined by the number of arriving and desorbing atoms. This changes when the diffusion length is increasing and hence the diffusion fields are overlapping (Fig. 3.22 (b-c)). Then, all adatoms on the surface might reach a kink site on a step and most of the adatoms reaching a kink site are incorporated into the

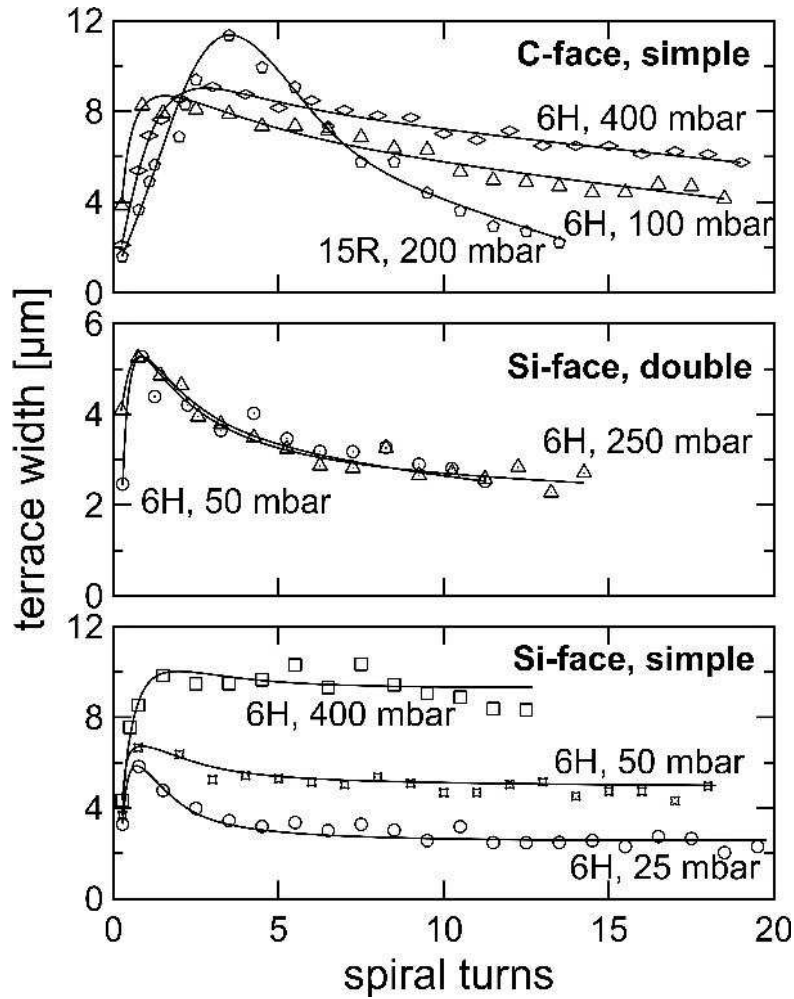


**Figure 3.21:** Spiral profiles of simple spirals on the Si-face (open circles 25 mbar, open stars 50 mbar, open squares, 400 mbar) and of double spirals on the Si-face (open circle with dot 50 mbar, open triangle with dot 250 mbar). The curves on the C-face are obtained for simple 6H (open triangles and rhombi, 100 mbar and 400 mbar respectively) and 15R (open pentagons, 200 mbar) spirals. The solid lines are a guide for the eyes and have no physical meaning.

crystal due to the fast incorporation kinetics which we have verified in chapter 2.2. Consequently, the maximum concentration in the middle of the terrace  $c_1$  and thus the supersaturation decreases (Fig. 3.22(d)).

The decrease of the supersaturation caused by the back stress effect leads, according to the BCF theory ( $\Lambda \propto 1/\sigma$ , Eq. 1.32), to an increased terrace width. Therefore, the presence of the back stress effect should result in an increased average terrace width as illustrated in Fig. 3.23.

The influence of the back stress effect on the spiral shape was simulated by

### 3 Spiral phenomena

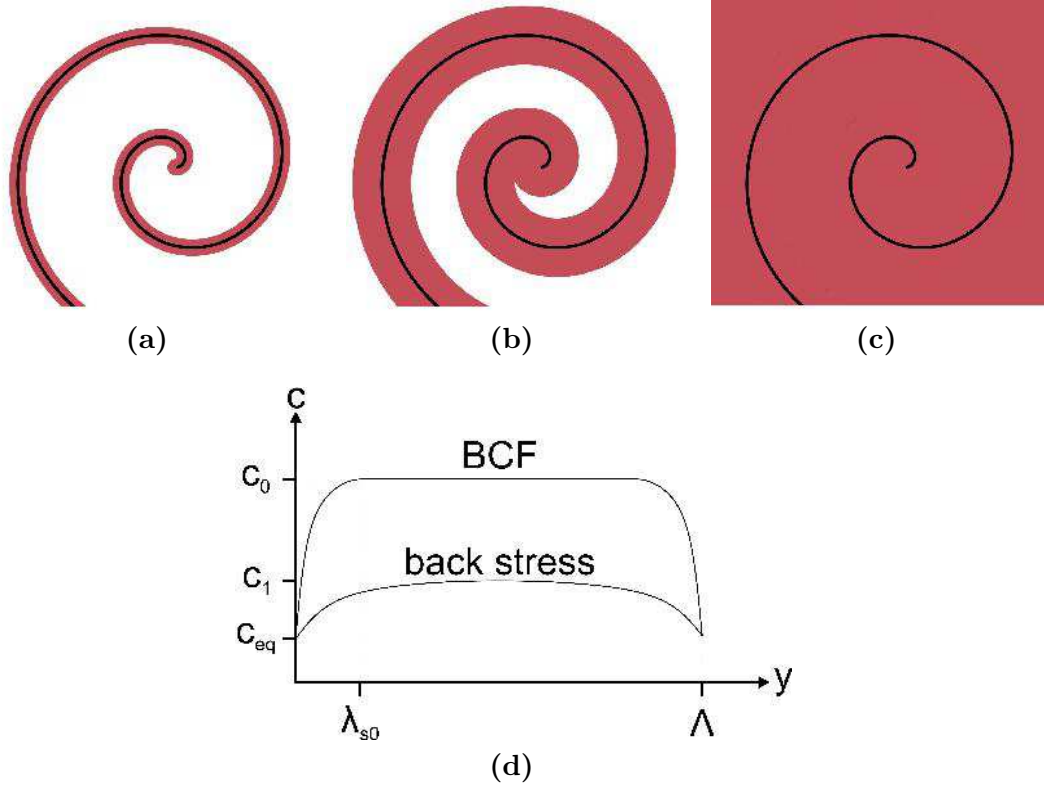


**Figure 3.22:** (a) When the surface diffusion length is small, the diffusion fields (red area) do not overlap. (b-c) With increasing diffusion length, the diffusion fields overlap. (d) The corresponding concentration profile to (c), *i.e.* if the surface diffusion length is larger than the terrace width.

Karma and Plapp [9]. They found that the terrace width of the first two spiral turns is a few percent smaller than the width far away from the centre. The velocity of the steps, and hence the supersaturation, increases after the first turns and that is why the step spacing also increases. Nevertheless, the terrace width approaches also a constant value which is larger than in the case without back stress effect. Accordingly, the appearance of a maximum within the first turns cannot be explained by the back stress effect.

Regarding the step velocity it becomes clear that the origin of the observed spiral shape is related to a (or several) local effect at the spiral centre. In Fig. 3.24 a step segment of an Archimedean spiral is highlighted red. This segment is first located close to the emergence point of the dislocation (Fig. 3.24 (a)) and after one spiral turn it will be at the position indicated in Fig. 3.24 (b). If the advance rate of this segment is constant all over the spiral it follows that the terrace width should always be the same. This is usually expected but not observed in our case.

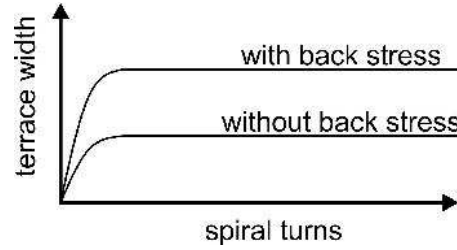


**Figure 3.23:** If the surface diffusion length is larger than the half average terrace width, the terrace width increases due to the back stress effect.

The increasing terrace width within the first turns is equivalent to an increase of the step velocity in the centre. When the maximum terrace width is reached, the velocity is reducing and approaching a constant value.

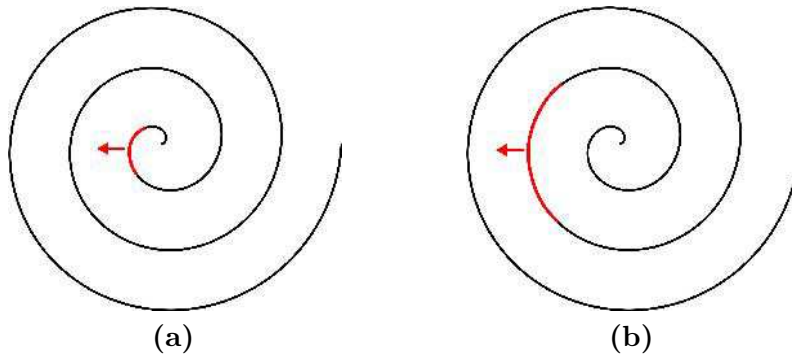


**Figure 3.24:** In the case of an Archimedean spiral the advance rate of a step segment is always the same and thus the step spacing remains constant.

From the discussion of the nucleation on the spiral terraces we know, that there might be an Ehrlich-Schwoebel barrier on the Si-face grown crystals (which is probably smaller than on the C-face). At the spiral centre this barrier can be lowered or even cancelled by two effects as illustrated in Fig. 3.25. First of all, the stress field of the screw dislocation facilitates the adatom incorporation from an upper terrace. Secondly, adatoms on the upper terrace at the centre can diffuse around the spiral centre to the lower edge. In both cases, the surface of collection is increased at the edge and hence the advance rate increases as well. However, 2D numerical simulations are necessary to verify that these two effects actually play a role in the spiral centre. Such simulations would go beyond the scope of this thesis and therefore we have to leave the question open if the different adatom incorporation in the centre is responsible for the observed spiral shape.

### 3 Spiral phenomena

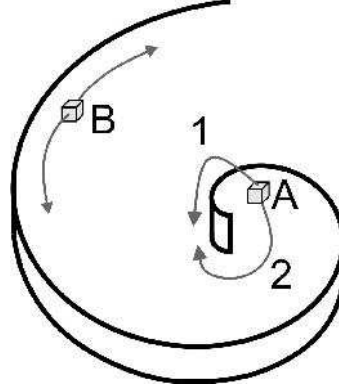


**Figure 3.25:** The Ehrlich-Schwoebel barrier may be of less importance at the spiral centre (atom A) due to the stress field of the screw dislocation (1) or adatom diffusion around the centre (2). Adatoms which are not located at the centre (*e.g.* adatom B) can only diffuse along the descending step in case of a strong ES barrier.

#### Experimental spiral growth laws

The measured values of the average terrace width for the simple spirals on the **Si-face** are plotted as a function of the growth rate in Fig. 3.26. In addition, the maximum terrace width of the simple and double spirals are plotted in this graph. The error bars indicate the standard deviation of the terrace widths. For the maximum of the double spiral we do not show error bars due to the low number of samples.

The average terrace width of the simple spirals shows an inverse square root dependence on the growth rate and follows thus perfectly the BCF theory in the case of  $\lambda_s \ll \Lambda$ . In contrast, the growth law of the maximum value of the simple and double spirals is different. The fit exponent is -0.27 and -0.17 for the maximum values of the simple and double spirals respectively. Although we are not able to determine the supersaturation directly, this graph shows that the supersaturation increases with increasing growth rate ( $R \propto \sigma^2$ , Eq. 1.33).

The increase of the fit exponent for the maximum terrace width of the simple spirals may also be related to the effect of changed adatom incorporation at the spiral centre. The supersaturation at the centre might be less dependent on the variation of the pressure since this edge is not only supplied by adatoms from the lower but also from the upper terrace. But as mentioned before, such a mechanism is speculative and needs verification by simulations.

Previously, it has been discussed that the back stress effect changes the spiral shape. In addition, this effect also changes the growth law [7][9]. Karma and Plapp performed simulations on the spiral growth considering this effect and found a

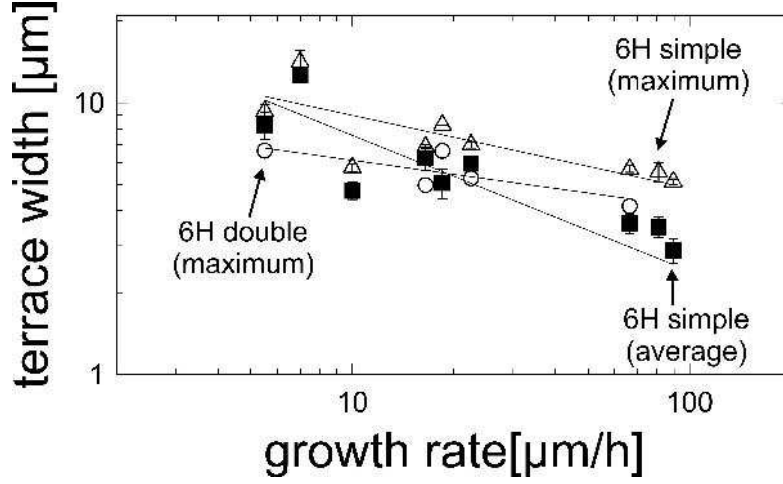


**Figure 3.26:** The terrace width as a function of the growth rate on the Si-face. The exponent from the power fits is  $-0.5$  for the average of the simple spirals (filled squares),  $-0.27$  for the maximum of the simple spirals (open triangles) and  $-0.17$  for the maximum of the double spirals (open circles).

dependency of the terrace width  $\Lambda$  on the growth rate  $R$  of the form  $\Lambda \propto R^{-n}$  [9]. If  $n$  is equal to  $1/2$  there is no back stress effect present and the classical BCF theory is applicable. The back stress effect is of importance if  $n$  is between  $1/3$  and  $1/2$ .

Regarding the simple spiral shapes the presence of this effect can be excluded due to the validity of the BCF theory that follows from the fit exponent. However, for the double spirals the back stress effect may play a role. Due to the different advance rates of the two branches, they approach each other on the hexagonal axes. The diffusion length exceeds then the terrace width resulting in the overlap of the diffusion fields and hence the back stress effect. Yet, the fit exponent of  $-0.17$  is still higher than in the simulations of Karma and Plapp. This may be attributed to a limited domain size as will be shown later on in the simulations section.

Some remarks are necessary for the correct interpretation of the results of Karma and Plapp. In their paper, they actually derived a dependence for  $\Lambda$  on  $\sigma$ , which is  $\Lambda \propto \sigma^{-n}$ . As we do not have any mean to determine the supersaturation, we have to replace the supersaturation by the growth rate. The back stress effect is only possible if the surface diffusion length is larger than the terrace width and then it follows for the growth rate that  $R \propto \sigma$  (see chapter 1.4.3 for a detailed derivation). This results in the relation  $\Lambda \propto R^{-n}$ . The exponent  $n$  is in case of the back stress effect always between  $1/3$  and  $1/2$ . But if the classical BCF theory applies, the law for the rate is different ( $R \propto \sigma^2$ ) and hence the exponent  $n$  depends on which relation is considered. For  $\Lambda \propto R^{-n}$  the BCF exponent is  $1/2$  whereas it changes

### 3 Spiral phenomena

to 1 for  $\Lambda \propto \sigma^{-n}$ .

Tab. 3.1 summarizes the exponent for the different cases. When we compare our results with those obtained from other authors it is important to know if they obtained it by considering the supersaturation or the growth rate. For example, an exponent close to 0.5 clearly indicates the back stress effect if the supersaturation was measured in the experiment. Contrary, if the growth rate was determined instead an exponent of almost 0.5 corresponds (rather) to the BCF theory.

**Table 3.1:** The exponent  $n$  for the different growth relations.

	$\Lambda \propto \sigma^{-n}$	$\Lambda \propto R^{-n}$
$n_{BCF}$	1	1/2
$n_{bs}$	$1/3 < n < 1/2$	$1/3 < n < 1/2$

Experimental verifications of the BCF theory or the back stress effect are rare in literature. Rangelov *et al.* analysed the spiral growth on Si (111) surfaces [10]. A source Si wafer is placed parallel to a second Si wafer. The source wafer is evaporated resulting in spiral growth on the second wafer. These spirals were observed *in-situ* by low distortion reflection electron microscopy and the authors found that  $n = 0.45 \pm 0.05$ . As the authors determined the supersaturation, it is evident that the back stress effect is present.

Another experimental observation of the back stress effect was by Wiesauer and Springholz [101]. They studied the terrace width as a function of the growth rate for PbTe spirals grown on BaF<sub>2</sub> (111) substrates. The film was grown by molecular beam epitaxy. The authors found an exponent of 1/3 which is clearly indicating the back stress effect.

The terrace width of the spirals on the **C-face** is completely independent of the supersaturation since the terrace width is constant for both 6H and 15R polytype (Fig. 3.27). In chapter 3.2 it has already been shown, that the terrace width can be constant if there are many dislocations on a single domain. Furthermore, the width can become almost constant if the steps are generated by a micropipe.

The latter has been experimental verified by De Yoreo *et al.* [102]. They grew crystals of potassium dihydrogen phosphate (KH<sub>2</sub>PO<sub>4</sub>, KPD) and analysed the surfaces by AFM. The observed spirals always had an open core, *i.e.* they were micropipes. The measured terrace widths were almost constant over a large supersaturation range. This was attributed to the presence of the hollow core. However, such an effect can be excluded in our case since we only considered single independent spirals without empty core. In the following we will present simulation results

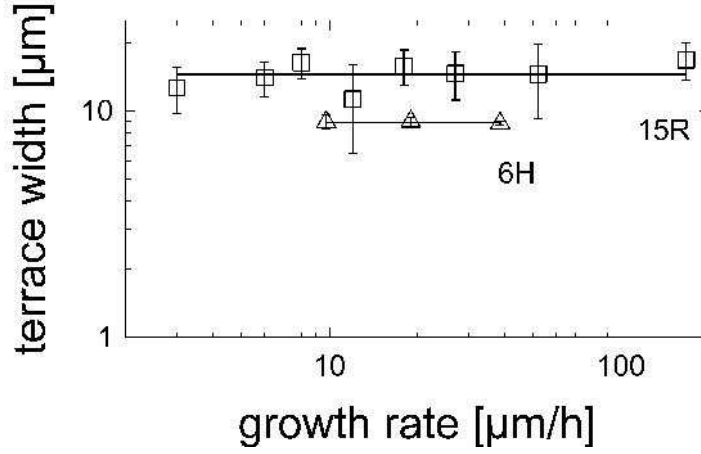


**Figure 3.27:** The terrace width as a function of the growth rate on the C-face. The fit of the 15R simple spirals is constant. The scale is the same as in Fig. 3.26.

which suggest that if both a substantial ES effect and a large surface diffusion length are present, the variation of the terrace width with the growth rate becomes small.

### Simulations

The aim of the simulations is to find an explanation for the double Si-face and single C-face spiral shapes and, moreover, for the corresponding growth laws. If diffusion fields are overlapping, the back stress effect can reduce the power law exponent down to  $1/3$  [9]. The additional presence of an Ehrlich-Schwoebel barrier is certainly affecting the growth law. Its effect on the spiral and two dimensional nucleation growth of Pt(111) was studied by Redinger *et al.* [8]. However, the authors focused on the comparison between the shape of a hillock formed by spirals and by nucleation. They did not report about the terrace width as a function of the growth rate. The reported spiral shapes from their experiments and simulations show similarities to the C-face spirals observed here, as the terrace width is first increasing followed by a strong decrease. The authors attribute the latter decrease to the finite size of the phase field simulation and hence the limited domain size of the spirals. Also in our experiments the domain size of the spirals is always limited, either by other surrounding domains or by the overgrowth of micropipes.

A simulation programme created in our laboratory was used to study the effect of the surface diffusion length, domain size and Ehrlich-Schwoebel barrier on the spiral shape as well as on the growth law [103]. The numerical approach is quite similar to the one developed by van der Hoek *et al.* [71]. These authors simulated



### 3 Spiral phenomena

the shape of double spirals considering the anisotropy of the specific edge energy.

In our simulations the advance rate of a step depends only on the concentration gradient at the rising edge. Incorporation of adatoms from the terrace above is forbidden. This is equivalent to a strong Ehrlich-Schwoebel effect. The simulation starts with a straight step fixed at one end which corresponds to the emergence point of the dislocation. On this step there is a given number of points. The velocity of each point is calculated similar to Eq. 1.28 but without reducing the exponential function to its first order as in Eq. 1.21:

$$v = v_0 \sigma \left\{ 1 + \frac{1}{\sigma} \left[ 1 - \exp \left( \frac{\rho_c}{\rho \sigma} \right) \right] \right\} \tanh \left( \frac{\Lambda}{2\lambda_s} \right) \quad (3.10)$$

On the initial straight step the points used to calculate the step velocity are equidistant. As the step proceeds during growth, the distance between the points is changing. Due to the curvature of the step the points in the centre are closer located to each other than outside. Therefore points are added where the curvature becomes higher and deleted where the curvature becomes smaller, as proposed by van der Hoek *et al.* [71].

Before the step velocity can be calculated, the local concentration and then the terrace width must be determined first. The concentration profile in a segment on the terrace is calculated as indicated by the grey shaded areas in Fig. 3.28. For the terrace width, the normal to the current position in direction of the next descending step is created. The terrace width is then obtained by interpolating the intersection coordinates between the normal and the step. The advantage of this approximation is, that the concentration profile does not need to be solved two dimensionally accelerating thus computation time. But at the centre of a simple spiral, this approximation becomes inaccurate since the local supersaturation is affected by diffusion around the dislocation centre (Fig. 3.28, red shaded area). A higher accuracy is hence obtained by simulating double spirals.

Our simulation is capable to include anisotropic effects and the stress field of the dislocation but for simplicity these two effects are neglected. For each simulated spiral it is ensured that the steady state of growth is reached.

The importance of the diffusion length on the spiral shape in case of a strong ES effect is shown in Fig. 3.29. A diffusion length smaller than the terrace width results in independent and equidistant steps (Fig. 3.29 (a)). When the distance between a step and the domain boundary becomes smaller than the equilibrium terrace width, which is the width without a domain boundary, the adatom concentration decreases and thus the terrace width is reduced progressively.

The coupling of the diffusion fields, *i.e.*  $\lambda_s \gg \Lambda$ , results in a spiral with continuously decreasing terrace width towards the domain boundary. Consequently,

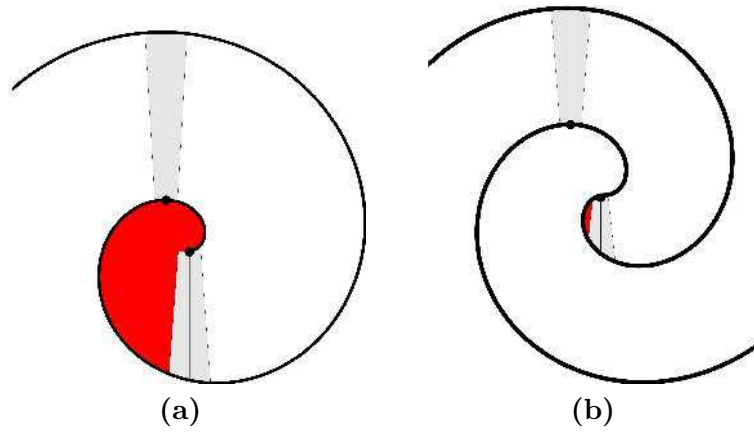


**Figure 3.28:** The accuracy of the simulation is lower on (a) single than on (b) double spirals since diffusion at the centre is less important in the second case. However, outside the centre, this does not play a role.

the terrace width is a function of the number of spiral turns and the size of the domain.

Fig. 3.30 shows the maximum terrace width as a function of the domain size and with the supersaturation as parameter for  $\lambda_s \gg \Lambda$ . At low supersaturations the domain size influences strongly the maximum terrace width. With increasing supersaturation the variation of the terrace width diminishes. The actual diffusion

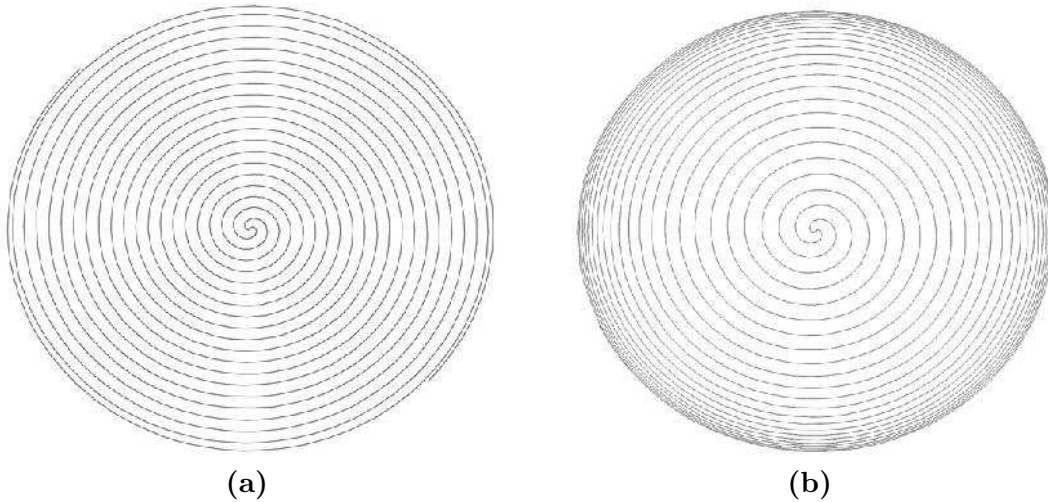


**Figure 3.29:** Spiral shapes obtained (a) for small surface diffusion length ( $\lambda_s \ll \Lambda$ ) and (b) large diffusion length ( $\lambda_s \gg \Lambda$ ). The spiral growth is limited to a disk which corresponds to the domain size.

### 3 Spiral phenomena

on the surface is getting confined under the assumption of a strong Ehrlich-Schwoebel barrier with increasing supersaturation as the terrace width decreases. The larger the terrace width is, the larger is also the “catchment” area of adatoms. As a consequence, the influence of a large diffusion length is of higher importance for lower supersaturations.

The large possible variation of the maximum terrace width with the domain size for a given supersaturation is also observed in our experiments, especially for the 15R spirals (indicated by the error bars in Fig. 3.27). For instance, on the sample with a growth rate of 12  $\mu\text{m}/\text{h}$  the measured maximum terrace width varies between 7.03 and 17.4  $\mu\text{m}$ . This can be ascribed to the different domain sizes of the spirals. This also implies, that the growth law can be partially concealed by the variation of the domain size. Yet, according to the simulation results the maximum terrace width is not independent of the supersaturation.

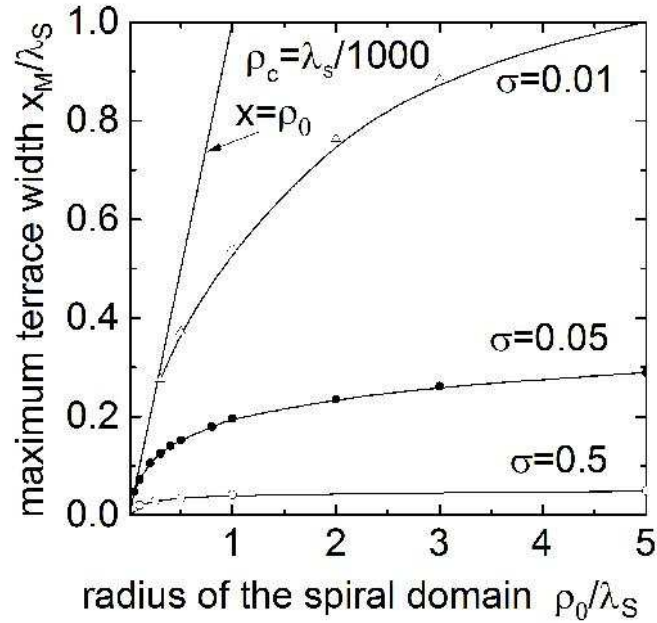


**Figure 3.30:** Simulated variation of the maximal terrace width  $x_M$  versus the ratio of finite domain size  $\rho_0$  and surface diffusion length  $\lambda_s$  with supersaturation as parameter.

Experimentally we observed that the terrace width is constant after one turn on the Si-face whereas there is a continuous decrease after a maximum on the C-face. We also simulated the terrace width as a function of the number of spiral turns for varying surface diffusion length normalized to the critical radius defined in Eq. 1.24 (Fig 3.31). For diffusion lengths smaller than or equal to half the terrace width ( $\lambda_s/\rho_c = 500$  in Fig 3.31) the terrace width is constant after a few turns except

close to the domain border. As the surface diffusion length increases, the constant plateau decreases and finally only a broad peak remains. The simulated spiral shape agrees in principle with the observed shapes for the spirals on the C-face and the double spirals on the Si-face (Fig. 3.21). Deviations between experiment and simulation can be explained by the assumption of a strong Ehrlich-Schwoebel effect in our simulations, which completely forbids the incorporation of adatoms from upper terraces. We do not suppose that this corresponds to the real situation during the growth.

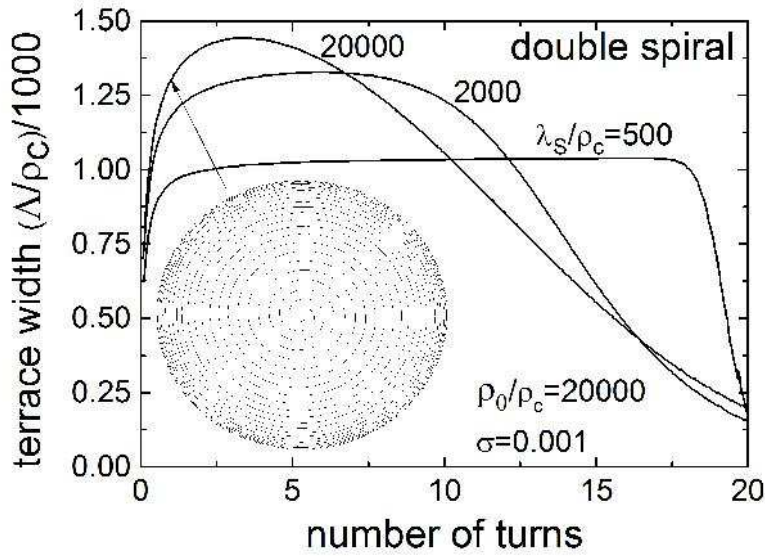


**Figure 3.31:** Simulated variation of the terrace width with the number of turns  $N$ , with the diffusion length  $\lambda_s$  as parameter.

The conclusion that the diffusion length is larger on the C-face than on the Si-face is in agreement with the results from nucleation (see chapter 2.3.3) and the publication by Matsunami *et al.* [67].

## 3.4 Spiral step dissociation

The spiral growth on SiC on-axis crystals is a well known and understood growth process. During the growth of SiC crystals on C-face substrates in this work it was observed that under certain reproducible growth conditions the top bilayer of a spiral dissociated as shown in Fig. 3.32(a). This phenomenon has not yet been described or reported in literature.

### 3 Spiral phenomena

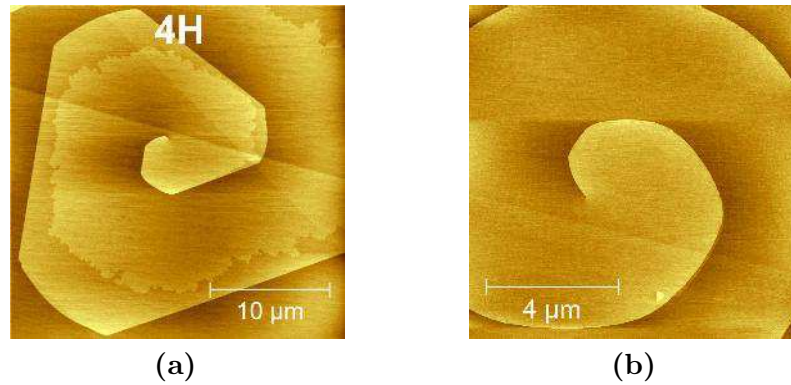


**Figure 3.32:** (a) A 4H spiral on a C-face substrate. The top bilayer ( $2.5 \text{ \AA}$ ) dissociated while the other bilayers remain bunched (height  $7.5 \text{ \AA}$ ). (b) A 6H spiral on a Si-face sample showing no dissociation. The step height is  $15 \text{ \AA}$ .

#### 3.4.1 Experimental

SiC crystals were grown on 6H on-axis Si- and C-face substrates. The growth process was the same as described in chapter 2.1.2. The deposition pressure was varied between 10 and 400 mbar and the deposition time between 30 min and 5 h. The growth spirals on the sample surfaces were characterized as explained in chapter 2.1.3. On the Si-face substrates the grown crystal were always of the 6H polytype. In contrast, the domains grown on the C-face were either of the 4H or 15R polytype. The 6H polytype was mainly observed on micropipes on the C-face.

#### 3.4.2 Results

A spiral step dissociation on the sample surfaces was observed when

1. a C-face substrate and
2. a fresh SiC powder source

were used for the growth process.

The dissociation of the top bilayer was observed for any polytype (4H, 6H, 15R), for any pressure and any deposition time studied. The height of  $2.5 \text{ \AA}$  of this layer was confirmed by AFM in all cases and is exemplary shown in Fig. 3.33. The other bilayers below the dissociated one remained bunched. Fig. 3.35 shows some examples of dissociation for different growth conditions. The spiral dissociation was also observed on a crystal grown on a C-face Lely seed (Fig. 3.36).

Experiments on the Si-face with the same growth parameters as on the C-face never resulted in dissociated growth spirals, even when a fresh SiC powder was used.

### 3.4 Spiral step dissociation

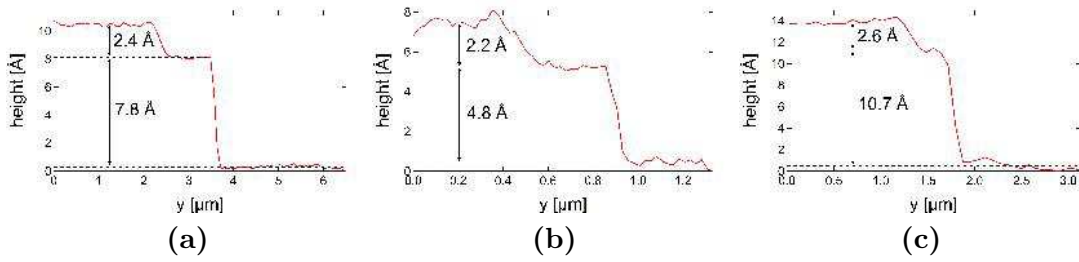


**Figure 3.33:** Step profiles measured by AFM of (a) a 4H spiral, (b) a 6H micropipe and (c) a 15R spiral. Only the top bilayer dissociates and its height is always 2.5 Å.

On the C-face the dissociation was only observed with a fresh powder, otherwise the step profile was the same as on the Si-face.

Having a closer look on the dissociated bilayers it can be noticed that next to the emerging point of the screw dislocation the steps are bunched and that there is no dissociation. However, within the first half turn of the spiral, the top bilayer detaches. The width of the dissociated bilayer is in most cases around half the total terrace width as illustrated in Fig. 3.34. The term total terrace width means the distance between two bunched steps. In addition, the dissociated bilayers are usually unstable and show fluctuations. The phenomenon of parasitic nucleation that was observed on some samples was discussed previously in chapter 2.3.

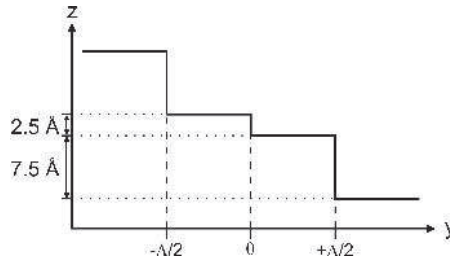


**Figure 3.34:** The position of the dissociated bilayer is schematically illustrated for the 4H polytype. The edge of the dissociated step is observed to be around the middle of two bunched steps for all polytypes.



### 3 Spiral phenomena

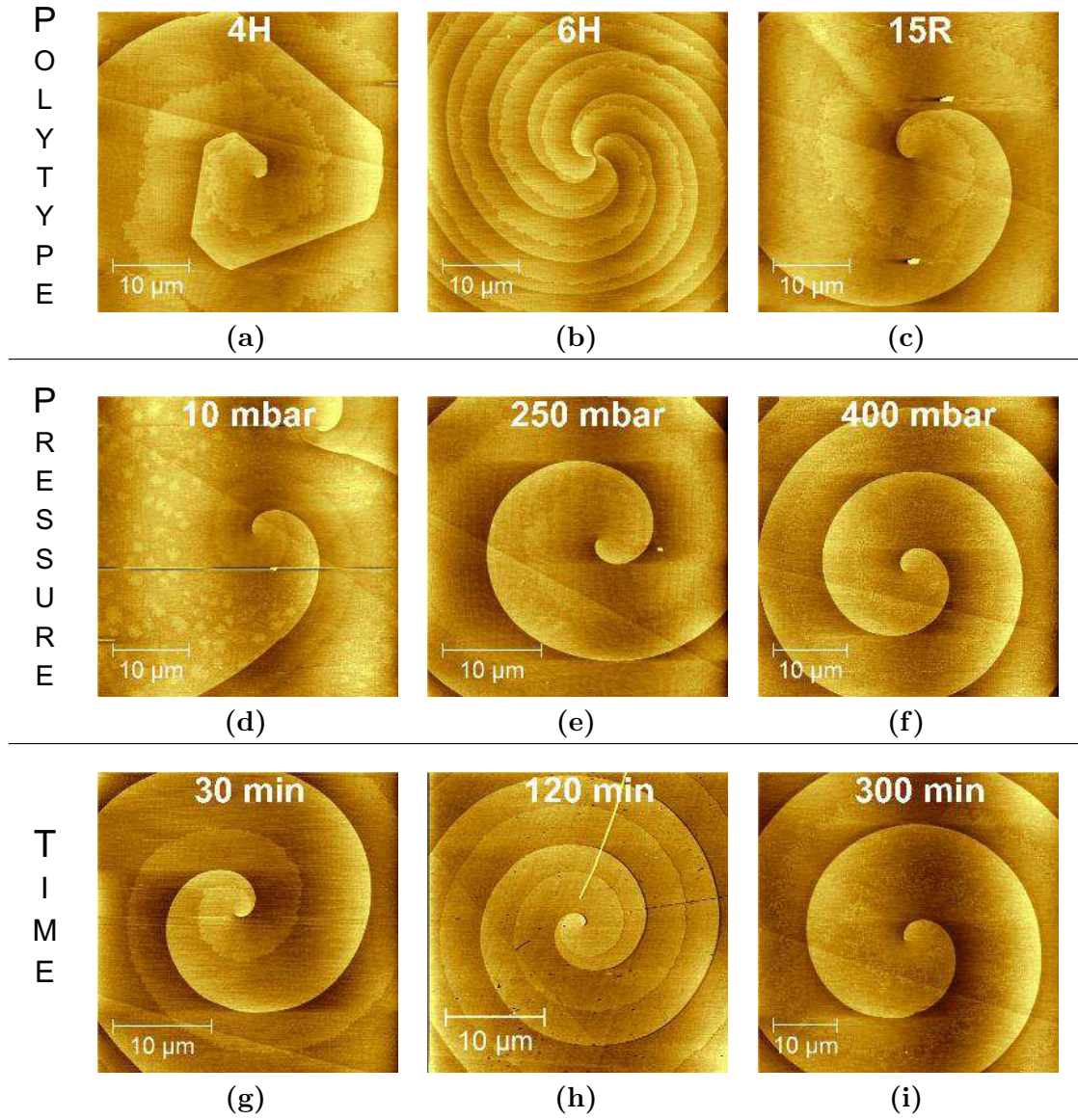


**Figure 3.35:** The step dissociation was observed for all polytypes (a-c), varying pressures (d-f) and deposition times (g-i). Note that all shown spirals are from different samples.



**Figure 3.36:** A dissociated spiral grown on a Lely seed. The dissociation is maintained over the whole spiral.



#### 3.4.3 Discussion

##### Related phenomenons

The step height of closed core growth spirals is usually an integer value of the  $c$  lattice parameter. Amelinckx was the first who observed that 6H spirals may form double growth spirals [70]. These spirals consist of two branches with step heights of 7.5 Å. Thus one branch corresponds to three bilayers or a half unit cell. Also the step height of 15R spirals is with one third of the unit cell (12.5 Å) smaller than the actual  $c$  lattice parameter [3]. However, all these steps are still higher than the single bilayer observed in this work.

Another phenomenon often discussed in the field of SiC growth is step bunching. Several steps on the surface bunch to form macroscopic steps whose height can be some tenth of the unit cells. Step bunching is usually observed in the step flow growth on off-axis substrates where straight steps are growing laterally [104] but also on growth spirals [95]. The formation of these macrosteps is explained by the relative movement of two steps. While one step is moving slowly the step above moves faster and is thus catching up to the lower step resulting in a macrostep. This idea of step bunching does not correspond to the observations made in this work as the top layer is detaching from the main step. Yet, the bilayers below the dissociated step are here referred to as bunched in order to emphasize the difference to the top bilayer.

##### Origin of the spiral step dissociation

Kimoto *et al.* studied the CVD growth of 4H, 6H and 15R SiC on substrates off-oriented 3 – 8° towards the  $\langle 11\bar{2}0 \rangle$  direction [105][106]. They observed that on the Si-face the step height mostly corresponds to two (4H) or three bilayers (6H and 15R) while on C-face mainly single bilayer steps exist. The off-angle and polytype has only a low impact on the step height contrary to the C/Si ratio that can drastically change the morphology. High C/Si ratios, *i.e.* 5 whereas 2 is low, rather lead to bunched steps. They suggest that a low C/Si ratio results in a higher nitrogen doping concentration which may impede the advance of the steps and maintain hence the single bilayers. This argument is based on a publication of Larkin *et al.* who reported that nitrogen and carbon compete for the incorporation on C sites in the crystal and that a C-rich environment results in a lower nitrogen concentration in the crystal [107].

Based on the experimental observations of Kimoto *et al.* Monte Carlo simulations were performed by Stout and in addition by Borovikov *et al.* [108][109]. Stout

### 3.4 Spiral step dissociation

simulated the growth of various polytypes (2H, 4H, 6H, 3C) on  $8^\circ$  off-oriented (0001) surface towards the  $\langle 1\bar{1}00 \rangle$  directions. The steps of the 3C polytype remained unbunched, *i.e.* of single bilayer step height, while for the hexagonal polytypes step bunching occurred. The step configuration is 2 bunched bilayers for the 2H, 1+3 bilayers for the 4H and 1+1+4 bilayers for the 6H polytype. According to Stout, this is caused by the different bonding configurations of the bilayers.

A similar argument is brought forward by Borovikov *et al.* Depending on the orientation of the tetrahedrons in the bilayer, two bonding configurations are possible at the step edge (Fig. 3.37). The jump of an adatom from an upper layer to the lower step is more difficult at a  $S_N$  than at a  $S_D$  step. Two jumps are required for an adatom at a  $S_N$  step in order to get attached to the step. On the other hand, only one jump is necessary for an adatom at a  $S_D$  step. Hence, adatom incorporation on a  $S_N$  step impeded resulting in a lower step velocity. The Ehrlich-Schwoebel barrier is consequently different for both step types.

The difference between the simulations of Stout and Borovikov *et al.* is that in the latter publication a scaling factor is introduced, which can be interpreted as adatom surface diffusion length. This length is dependent on the tetrahedron orientation of the underlying bilayer. Thereby "beyond-nearest-neighbor interactions", which are responsible for the long range formation of a polytype, are taken into consideration. The scaling factor is taken from Righi *et al.* who determined this factor for the Si-face [56].

As a result, Borovikov *et al.* found that on a (0001) surface with a miscut towards the  $\langle 1\bar{1}00 \rangle$  direction first a stepped structure of 3+3 bilayers is formed which then further bunches to steps with 6 bilayers. A miscut towards the  $\langle 11\bar{2}0 \rangle$  always results in 3+3 bilayers. This configuration remains stable due to a zigzag step shape with alternating  $S_N$  and  $S_D$  segments within one step. On the C-face similar results are obtained. Due to the lack of data for the scaling factor on the C-face, they used the same factor on both faces. The authors suggest that this causes the similar results.

The experimental results of Kimoto *et al.* and the related simulations of Borovikov *et al.* and Stout show, that the seed polarity and the step orientation plays an

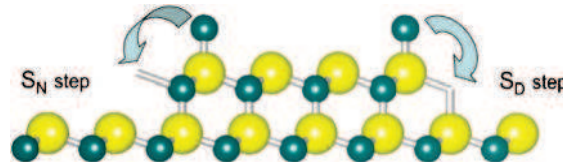


**Figure 3.37:** The advance rate of a step depends on the bonding configuration at the edge. Image taken from [109].

### 3 Spiral phenomena

important role for their configuration. Now coming back to the spiral dissociation, we can conclude that the phenomenon observed by Kimoto *et al.* is not related to our dissociation. The spirals are continuously changing their step orientation when they wind up which is completely different to the miscut induced step morphology of Kimoto *et al.* The simulations of Borovikov *et al.* show that the bunching behavior is depending on the step orientation which is conflicting with a spiral shape. Therefore, there is probably another mechanism responsible for the spiral step dissociation.

Since the different step configurations are unlikely to cause the spiral dissociation, we will briefly examine the suggestion of Kimoto *et al.*, that the amount of impurities might be important for the step structure. The analysis of the SiC powder before and after the growth process by X-ray diffraction (Fig.3.38) reveals that only the fresh powder contains silica ( $\text{SiO}_2$ ). Thus it can be concluded that the silica in the powder evaporates completely during the heat ramp and initial SiC growth. This possibly changes the partial pressures of the sublimating SiC species and hence the C/Si ratio. This might also enhance the incorporation of impurities, as reported by Larkin *et al.*, which result in the spiral dissociation. Moreover, such a mechanism would agree with the observation of step bunching if the crystals are grown from an used powder which does not contain silica. The incorporation of nitrogen impurities is known to be easier on the C- than on the Si-face [110][51]. Another difference between a fresh and used powder is their different porosity. A fresh powder can adsorb more air and hence nitrogen during air exposure than a used powder with reduced porosity. This might explain why the dissociation is only observed on the C-face growth with a fresh powder.

For the sake of completeness, it should be mentioned that the doping via nitrogen can result in step bunching. This was reported by Papaioannou *et al.* for the CVD growth on  $3.5^\circ$  off-oriented (0001) substrates [111]. They used  $\text{N}_2$  and  $\text{NH}_3$  as doping gas and observed a strong increase in step bunching compared to undoped crystals. The nitrogen concentration in the crystals is not mentioned. Ohtani *et al.* studied the formation of meandering macrosteps due to nitrogen doping [112]. The step structure of doped ( $\text{N} = 1 \cdot 10^{19} \text{ cm}^{-3}$ ) and undoped ( $\text{N} = 4 \cdot 10^{17} \text{ cm}^{-3}$ ) crystals grown on the {0001} faces were analyzed by AFM. The undoped C-face crystal and the doped Si-face crystal show both perfectly straight and equidistant steps. On the doped C-face crystal the formation of meandering macrosteps of 7 to 15 nm is observed. They suggest that this is caused by a competition between modified step kinetics due to the nitrogen incorporation and the elastic step interactions.

In both studies, step bunching is observed if additional nitrogen is introduced to the growth process. The authors of both publications agree, that the usual

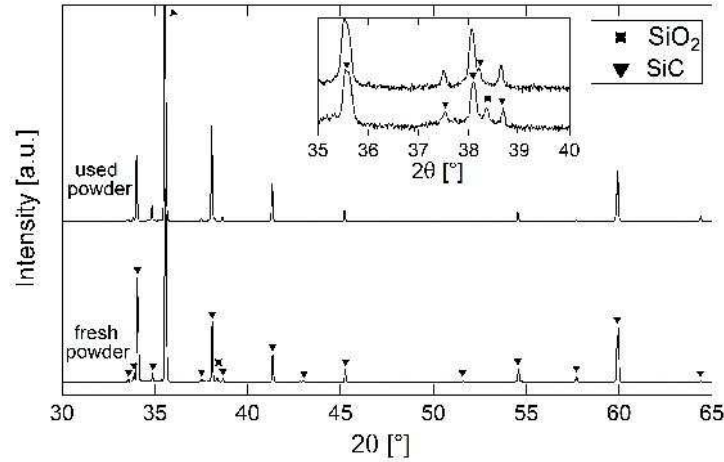


**Figure 3.38:** X-ray diffraction pattern of a fresh and a used SiC powder. The different phases found in the diffraction pattern for SiC are not indicated individually in order to emphasize that the main difference between the powders is the SiO<sub>2</sub> content.

unintentional doping does not result in bunching. Therefore we can conclude, that the doping phenomena reported by Papaioannou *et al.* and Ohtani *et al.* are not of importance in our case.

Chernov reported for the vapour growth of  $\beta$ -methyl naphthalene and p-toluidine crystals that macroscopic steps gradually disintegrate into microscopic steps with increasing supersaturation [100]. We do not observe an effect of the pressure, and hence supersaturation, on the spiral dissociation and therefore we infer that the observations of Chernov rely on another mechanism.

It is known that bulk strain can change the structure of the steps on a vicinal surface [113]. This is usually observed and studied on heteroepitaxial growth of thin films [113][114][115]. Xie *et al.* studied for example the step structure of Ge<sub>0.5</sub>Si<sub>0.5</sub> films and found that the step energy strongly increases (decreases) if the layer is under tensile (compressive) strain [113]. The spiral steps are under shear strain of the screw dislocation and hence there is no tensile or compressive strain (except if the dislocation is of the mixed type). There exists no literature on the influence of the shear strain of a dislocation on the step structure but we assume that the dissociation is impeded by the shear in the center, since the top bilayer detaches not directly in the centre but after around a half spiral turn.

In summary, a mixture of several effects might cause the spiral step dissociation. One of them is possibly the enhanced impurity incorporation when silica is present. As the nitrogen incorporation rate is higher on the C-face than on the Si-face the

### 3 Spiral phenomena

polarity dependence of the dissociation might be explained. However, the shear strain rather impedes the step detachment in the centre. Further investigation are necessary to understand the mechanism of the dissociation.

#### The role of $\text{SiO}_2$

In order to check if the  $\text{SiO}_2$  content in the powder is of importance for the step dissociation, two additional experiments were performed. The aim was to force the step dissociation where previously only bunched steps were observed, *i.e.* on C-face with a used powder and on Si-face with a fresh powder.

Firstly, 0.54 g  $\text{SiO}_2$  powder was dispersed on top of an already used SiC powder crucible. A piece of silicon (0.74 g) was placed on the powder. Then a SiC crystal was grown on a C-face substrate for one hour at 200 mbar. On the sample surface 15R and 4H spirals were observed. While the steps of the 15R decomposed into single bilayers at the step edge, the 4H steps remained perfectly bunched (Fig. 3.39). It is clear that the  $\text{SiO}_2$  has an effect on the 15R step structure but it is curious that the 4H steps remain straight and bunched. Hence, the specific step configuration of each polytype might be important for the stability of a step.

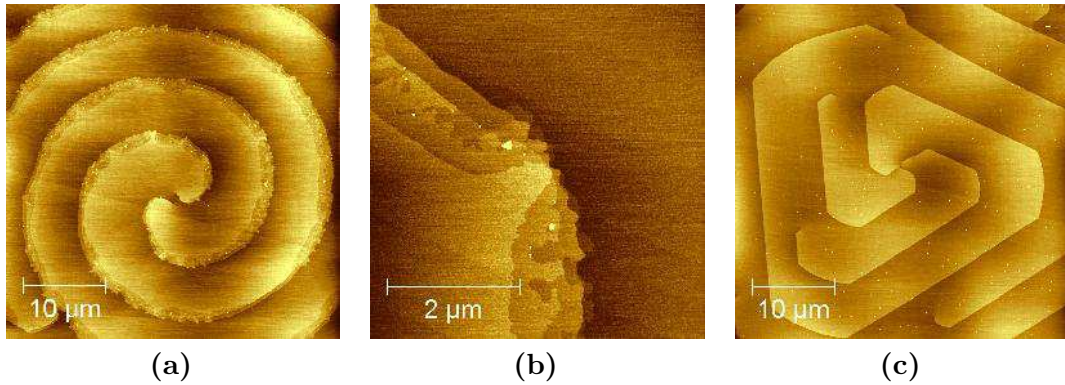


**Figure 3.39:** Adding  $\text{SiO}_2$  powder to a used SiC powder source for the growth of a SiC crystal on the C-face results in destabilization of the steps for the (a)(b) 15R but not for the (c) 4H polytype. On the 15R polytype the bunched step decomposes into single bilayers.

For the second experiment, a fresh SiC powder was used. On the top 19.90 g SiC powder was mixed with 4.34 g  $\text{SiO}_2$ . In addition, a silicon piece of 0.58 g was added as illustrated in Fig. 3.40 (a). Again, a SiC crystal was grown for one hour at 200 mbar but this time on a Si-face substrate. On the sample surface only polygonized 6H spirals were observed. The steps are straight but small triangularly

shaped bilayers are located at the step edges. Furthermore, few large islands are visible on the terraces. A step dissociation is not present and therefore it is concluded that the addition of  $\text{SiO}_2$  to the powder is not sufficient to force the dissociation on the Si-face.

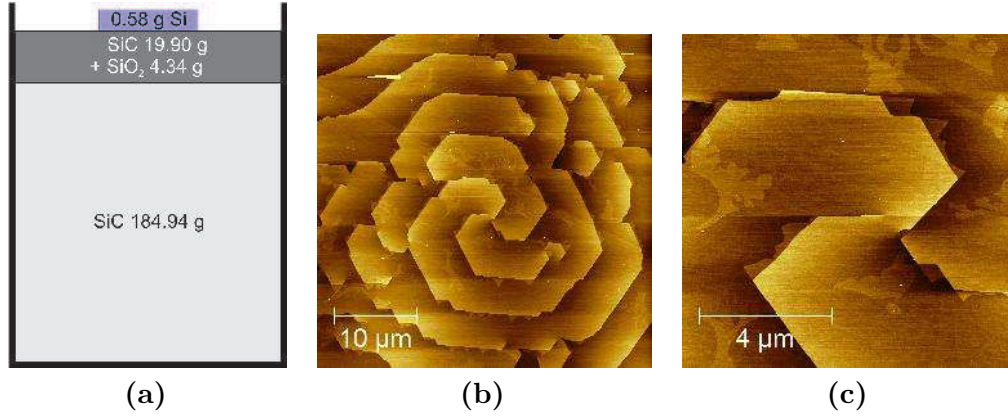


**Figure 3.40:** (a)  $\text{SiO}_2$  was mixed with SiC powder on top of the crucible. (b) The sample surface of SiC crystal grown on Si-face is covered by polygonized 6H spirals. (c) On the spiral surfaces islands and small triangular bilayers close to the step edges are visible.

From these experiments it is not clear if the  $\text{SiO}_2$  content in the powder may affect the step structure. Experiments with varying  $\text{SiO}_2$  content in the powder might give more information on the role of silica during the growth process.

#### Fluctuations of the top bilayer edges

All dissociated bilayers show fluctuations on their edges, *i.e.* they are not as straight or perfectly round shaped as the bunched steps. In order to understand why only single layers are diffuse we will give a short overview on the roughening of surfaces and steps.

The roughening transition describes the change from a smooth to rough surface due to an increase of the driving force or temperature. The Jackson factor  $\alpha$ , already introduced briefly in chapter 3.1.2, is a measure for the surface roughness [96]. If  $\alpha \leq 2$  the surface is expected to be rough, if  $\alpha > 3$  it is smooth. Typically, for metals the Jackson factor is 2, for semiconductors  $2 < \alpha < 3$  and for oxides and silicates  $\alpha > 3$  [95]. A surface is rough if 50 % of the available sites are randomly covered by atoms whereas a surface is smooth if there are either no atoms on the surface or if the coverage is 100 %.

The effect of the surface roughness on the spiral growth was simulated by Gilmer

### 3 Spiral phenomena

[116]. The growth spirals only contribute significantly to the growth rate at low supersaturations and low temperatures. If the supersaturation is high, 2D nucleation dominates the growth process. At high temperatures the number of kink sites provided by the spirals is low compared to those generated by the surface roughening. Consequently, the spiral arms are smoother at lower temperatures. Gilmer did not study the roughness of a spiral step as a function of their height.

There is, to our knowledge, no publication on the relation between spiral step height and their roughness. But, there is a similar effect on stepped surfaces, the step diffusivity, which has been studied thoroughly.

In the literature there are many examples of studies on the diffusivity of steps (see ref. [117] for an extensive list). For instance, Pai *et al.* related the fluctuations on Ag (110) steps with the dominating mass transport mechanism on the surface [118]. An expression which relates the diffusivity of a step with its stiffness was derived by Bartelt *et al.* [119]. It has also been observed, that the step stiffness is dependent on the step orientation. On silicon the reported values for the stiffness vary in a wide range from  $0.72 \text{ meV/\AA}$  on the (113) surface to  $68 \text{ meV/\AA}$  on the (111) surface at  $900^\circ\text{C}$  [120][121].

By making use of the expressions from Bartelt *et al.*, Sudoh and co-workers analysed the diffusivity of steps as a function of their height on the Si(113) surface [122]. They determined the fluctuations on single (height  $1.63 \text{ \AA}$ ), double, triple and quadruple steps from STM images and deduced the corresponding stiffnesses. According to their results small steps are more diffuse, *i.e.* show more fluctuations, than high steps. Their conclusion is that the step stiffness is proportional to the step height. This scaling has been confirmed by Yoon *et al.* also for steps on the Si(113) surface [120].

This reasoning is also valid for the spiral steps which we have observed. On our SiC samples the fluctuations are only observable on steps of single bilayer height. Fig. 3.41 shows bunched steps of  $5.0 \text{ \AA}$  height and dissociated single bilayers of  $2.5 \text{ \AA}$  height next to two micropipes. Hence, steps that are at least  $5.0 \text{ \AA}$  high are stiff enough to form a straight edge at the given growth temperature ( $2100^\circ\text{C}$ ).

The diffusivity varies in a wide range for the single bilayers on the different samples. This might indicate that the fluctuations are very sensitive to the growth temperature. Although the temperature was set to  $2100^\circ\text{C}$  for all experiments, variations cannot be excluded as the temperature is only read on top of the graphite crucible. The contact between seed and crucible is probably not always identical causing thus temperature differences on the seed surface.



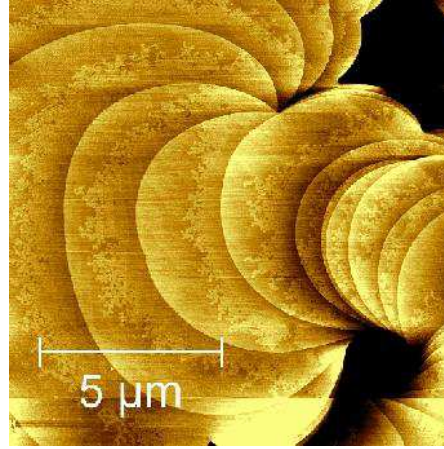


**Figure 3.41:** Step fluctuations are only observed for single bilayers.

### The position of the dissociated step

The position of the dissociated step on a terrace was measured on AFM images of spirals with at least two turns. The latter condition is necessary to verify that the dissociated step approaches a stable position. The relative position of the dissociated step between two bunched steps, which is the upper to total terrace width ratio, is plotted in Fig. 3.42 for different polytypes.

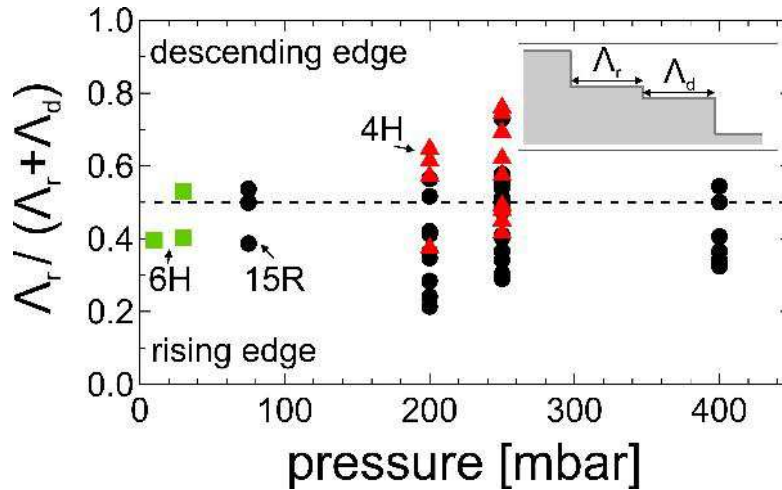


**Figure 3.42:** The relative position of the most dissociated steps is around 0.5 (dashed line), i.e. in the middle of a terrace.  $\Lambda_r$  is the distance of the dissociated step to the rising step and  $\Lambda_d$  respectively to the descending step. The green squares correspond to the 6H, the black circles to the 15R and the red triangles to the 4H polytype.



### 3 Spiral phenomena

The average of all relative positions is  $0.47 \pm 0.13$  and hence the dissociated step is located around the middle between two bunched steps. The data points at 75 mbar for the 15R polytype are obtained from one sample and indicate that there can be a large variation of the step position even for spirals grown on the same sample. Therefore, we infer that the principal dissociation is caused by the general growth conditions (seed polarity and powder preparation) but the relative position is influenced by local parameters. This could be, for example, the local impurity concentration. It is conceivable that a higher local impurity concentration results in a stronger retardation of the dissociated step and hence a position closer to the rising step.

The question is now, why the dissociated step remains at its position in the middle of a terrace even far from the spiral center. We suggest that this is related to the elastic interactions between the steps.

If one considers two steps with different heights but with a similar net flux towards them, one would expect a faster advance rate for the lower step. Less adatoms are necessary for the advance of this step. The experiments show that the dissociated steps are located around the middle of a terrace, independent of the growth time. This indicates that the velocity of the bunched and dissociated steps is equal despite their unequal heights. If their velocities were different, the faster step would catch up the slower one and hence only bunched steps should be present.

Atoms on a stepped surface do not have the same bonding configuration as the atoms on a flat surface. This causes a distortion of the perfect crystal lattice and hence a strain field. Consequently, each step is correlated to a elastic energy  $W_{int}$  and in the case of two steps of the same material but different step height and terrace width it follows [123]

$$W_{int} = 2h_1h_2 \frac{(1-\nu)^2}{\pi E} d_{bi}^2 \gamma^2 \left( \frac{1}{\Lambda_r^2} + \frac{1}{\Lambda_d^2} \right) \quad (3.11)$$

where  $\nu$  is the Poisson ratio,  $E$  Young's modulus,  $h_1$  and  $h_2$  the number of bilayers per step,  $d_{bi}$  the height of one bilayer (2.5 Å),  $\gamma$  the surface energy,  $\Lambda_r$  and  $\Lambda_d$  the terrace widths as illustrated in the inset of Fig. 3.42.

In principle, this equation could be used to perform simulations and hence to check if the assumption is right that the elastic interactions are responsible for the stable position of the dissociated bilayer. This is a challenging task, as the growth process is highly dynamic. The dynamics of this process become clear if we consider only one dissociated bilayer exactly located in the middle of a terrace. By incorporating an adatom at the step edge, this step advances and the elastic interactions with the nearby steps, and hence the surface concentrations on the

### 3.5 Conclusion on the growth spirals

steps, are changing. As a consequence, the advance rates of the bunched steps is also affected. The simulation of such a dynamic process is beyond the scope of this thesis and therefore we have to leave the question open whether the elastic interactions are responsible for the stable position of the dissociated step.

We would like to note that despite of elastic interactions the position of the dissociated step is not pinned to the centre of a terrace. Simulations and experimental results prove that the increased mobility of kink sites at elevated temperatures results in a variation of the average distances between steps [124][121]. A Gaussian distribution of step-step distances is obtained if there are repulsive forces, such as elastic interactions, between the steps [125]. This is what we actually observe for the dissociated step as shown in Fig. 3.43.

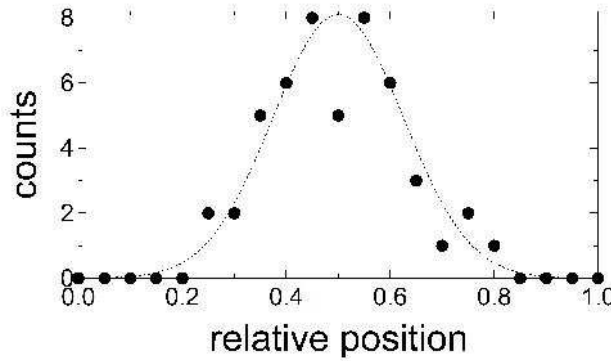


**Figure 3.43:** Distribution of the dissociated step on a terrace. The dashed line corresponds to a Gauss fit.

The drop at exactly 0.5 is however odd and indicates that step positions close to the terrace centre, but not in the centre, are preferred. But as the number of data points is low, the uncertainty of this histogram is high. Further studies are needed in order to verify and understand this distribution.

## 3.5 Conclusion on the growth spirals

In this chapter, the focus was on growth spirals on SiC. We have observed that the degree of polygonization of a growth spiral is depending on the polytype. Since the polygonization decreases with increasing distance to the centre we concluded that the specific edge energies are different for the two types of facets.

The average terrace width of the simple spirals on the Si-face as a function of the growth rate follows perfectly the BCF theory for  $\lambda_s \ll \Lambda$ . The supersaturation is higher for low pressures, or equivalently high growth rates, but no statement on

### *3 Spiral phenomena*

the absolute supersaturation can be made. The growth law of the double spirals is assumed to be strongly affected by the overlapping diffusion fields of the terraces. The maximum terrace widths on the C-face are constant for a wide range of growth rates. This has never been observed before for closed simple spirals. We assume that a limited domain size, the back stress effect and a strong Ehrlich-Schwoebel barrier contribute to this constant terrace width on the C-face.

Under certain growth conditions, we achieved a dissociation of the top spiral step. This novel observation is attributed to impurity incorporation and shear strain of the screw dislocation but further studies are necessary to understand the underlying mechanism. We have demonstrated that the stiffness of the dissociated step is extremely low which is why these steps show large fluctuations. The dissociated step is usually located around the middle of a terrace. We assume that elastic interactions between the step are responsible for the position of the dissociated step.





# Conclusion

In this thesis the on-axis growth of silicon carbide crystals was studied. New insights on the growth mechanism were obtained through a detailed analysis of surfaces grown by PVT and complimentary simulations.

We have ascertained that the growth of SiC by physical vapour transport is limited by the vapour phase transport and not by the surface diffusion and incorporation kinetics of adatoms at the surface. Therefore we conclude that the density of growth spirals, or kink sites respectively, is sufficiently large that the growth rate is not lowered.

Nucleation was occasionally observed on both Si- and C-face. The analysis of the nuclei revealed that the Ehrlich-Schwoebel barrier is more pronounced on the C- than on the Si-face. Due to the nuclei distribution on the spiral steps we conclude that the diffusion length on the C-face is larger than half the terrace width ( $\lambda_s > 3.12 \mu\text{m}$ ) at the used growth conditions. On the contrary we found that the diffusion length on the Si-face is smaller than half the terrace width ( $\lambda_s < 3.28 \mu\text{m}$ ). Although we could not determine the exact diffusion lengths, the obtained orders of magnitude can be helpful for other simulations on SiC.

For the first time, the growth modes of the spirals on the Si- and C-face of SiC were studied. The experimental results show that the growth mode of the spirals depends not only on the seed polarity, but also on the spiral type. The single spirals on the Si-face follow perfectly the BCF theory. However, the growth mode of the double spirals is different due to the back stress effect. The terrace widths are smaller than the diffusion length resulting in overlapping diffusion fields and a modified spiral growth.

The spirals on the C-face do not show any variation of the terrace width for changing growth rates. This has never been observed before for closed core spirals. Our simulations suggest that for a limited domain size, a strong Ehrlich-Schwoebel effect and the back stress effect can significantly lower the dependency of the terrace width on the growth rate. Yet, according to the simulation results the terrace width is not totally independent of the supersaturation. Hence, the simulations cannot entirely explain our experimental results.

The analysis of the spiral terrace width as a function of the growth rate does not give direct access to the supersaturation. However, the results on the Si-face

## *Conclusion*

reveal that the growth rate increases with the supersaturation. Therefore, we can determine on which sample the supersaturation was higher if we compare their terrace widths.

Finally, we observed a novel dissociation of spiral steps into a single bilayer and a bunched step. This dissociation is only obtained if a fresh powder and a C-face seed is used. The origin of this effect could not be clearly determined but we assume that impurity incorporation play an important role. The position of the dissociated step is around the centre of two bunched steps. We suggest that this is caused by the elastic interactions between the steps.

Our studies revealed new mechanisms on the spiral growth of SiC. Yet, we could not answer satisfactorily all questions caused by our observations. Hence, there is still some work to do.

The independence of the C-face spiral terrace widths on the supersaturation requires further study. As our simulations demonstrated, the domain size is a critical parameter influencing the terrace width. The initial domain size cannot be determined, but selecting only the spirals which are alone on a large domain might reveal if the terrace width is really fully independent of the supersaturation.

Another unresolved issue is the origin of spiral step dissociation. The experimental observations suggest that the SiO<sub>2</sub> content in the powder plays a crucial role on this effect. One approach to check if the SiO<sub>2</sub> is of importance for dissociation would be to grind the used powder and perform grow experiments with increasing SiO<sub>2</sub> content in this powder. Hence, a dissociation should be observable for a certain amount of SiO<sub>2</sub>. It would be also interesting to attempt if a further increase of the SiO<sub>2</sub> content in the powder results in a dissociation of all steps.

We assume that the position of dissociated step is maintained due to elastic interactions between the steps. This assumption has still to be verified by simulations.







# A Appendix

## A. Differential interference contrast (DIC) microscopy

The DIC microscopy, also Nomarski microscopy, is an optical microscopy technique used to image samples with little contrast in normal optical microscopes.

The optical setup of a DIC microscope can be either in transmission or reflection mode. The reflection mode will be described here as it was used for this thesis. Fig. A.1 shows the principal setup of the reflection mode. First the entering light is linearly polarized. Then the polarized light is split into two rays polarised at  $90^\circ$  to each other by a Nomarski prism. First the entering light is linearly polarized. Then the polarized light is split into two rays polarised at  $90^\circ$  to each other by a Nomarski prism.

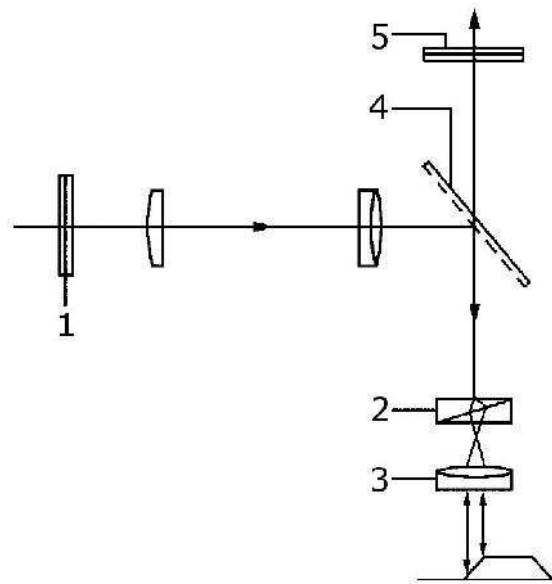


**Figure A.1:** Optical arrangement of a DIC microscope in reflection mode.(1) Polarizer; (2) Nomarski prism; (3) objective lens; (4) light reflector; (5) analyzer. Image taken modified from [126].

This prism consists of two birefringent crystals (*e.g.* quartz) wedges that are

## A Appendix

cemented together in a manner that the optical axis of the first wedge is parallel to the surface and the optical axis of the second one obliquely to the surface.

The two rays are aligned parallel by the objective lens. The distance between these two rays is called shear and is much smaller than the resolving power of the objective. The rays are reflected on the sample surface and recombined by the Nomarski prism. If the optical path is identical, the beam is recombined to linear polarized light and blocked by the analyzer that is in crossed position with the polarizer. However, if there is a difference in the optical path the Nomarski prism recombines the beams to elliptically polarized light which is not blocked by the polarizer.

Thus areas where the height changes appear bright whereas flat areas appear dark on the image. The obtained image seems like a pseudo 3D image. This is actually not the case as the bright regions only indicate a change in height but it is not clear if one sees *e.g.* a mound or sink. The advantage of DIC microscopy compared to normal optical microscopy is that even very small changes in height can be observed. The smallest by DIC microscopy seen spiral step height was  $7.5 \text{ \AA}$  in this thesis (Fig. A.2).

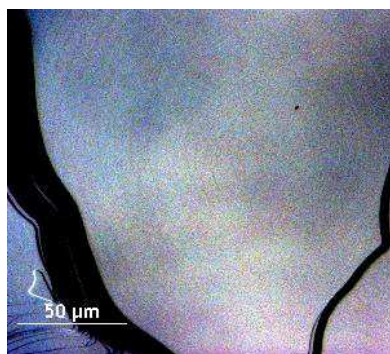


**Figure A.2:** Close to the height resolution limit of the used Normaski microscope: a 6H double spiral with a step height of  $7.5 \text{ \AA}$ .

## B. Atomic force microscopy (AFM)

The atomic force microscope is a tool to measure surface properties. In this work the AFM was used to analyze the surface topography of the samples. There are two modes to do this: contact and tapping mode. The principal setup which is shown in Fig. B.1 is the same in both cases. A probe scans the surface line per line. The piezo tube controls the x,y and z movement of this probe. On the back side of the probe a laser is reflected towards a photodetector.

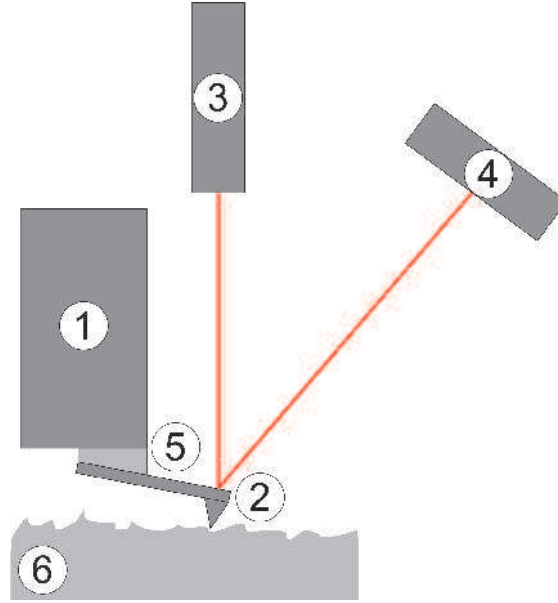


**Figure B.1:** Scheme of an AFM setup. (1) x,y and z piezo tube, (2) Cantilever and probe, (3) Laser, (4) Photodetector, (5) oscillation piezo, (6) Sample. Image taken modified from [127].

In contact mode, the probe is in direct contact with the sample surface. The setpoint of the force exerted by the probe on the sample is in the repulsive regime as illustrated in Fig. (a). The position of the laser on the photodetector is maintained constant by the AFM feedback system. If the height of the sample is changing during scanning the laser is deflected from the setpoint on the detector and the feedback system corrects this deflection by changing the z position of the piezo tube. The response to the change in height is not instantaneously as it is affected for instance by scanning frequency, gain parameters and sample topography (flat or rough). Therefore the deflection signal gives the error of the measurement. The amplitude of this signal indicates how fast the feedback system reacts on a height change.

Contrary to the contact mode, the probe is not in permanent contact with the sample surface when the tapping mode is used. An oscillating signal is generated and applied to the piezo between the piezo tube and the cantilever. Thus the cantilever is oscillating mechanically. The frequency is chosen to be close to the resonance frequency of the cantilever. If the probe is close to the surface, van der Waals forces cause a shift of the resonant frequency that is measured by the feedback system. Then the z position of the probe is adjusted in order to keep the resonant frequency constant. In tapping mode the error signal corresponds to the measured amplitude of the cantilever. In addition to the scan parameters

## A Appendix

in contact mode, the amplitude of the cantilever oscillation can be set in tapping mode. The smaller this amplitude is, the closer the probe is to the surface and the stronger the interactions between probe and sample surface become.

The advantage of the contact mode is that the response of the tip is directly related to the change in height and thus the surface can be measured fast. However, this mode might damage the sample surface or cause wear of the probe. The tapping mode is slower but damages the surface less. Also the signal to noise ratio is better in tapping mode.

## C. Raman spectroscopy

Raman spectroscopy is a widespread method to identify the polytype(s) of a SiC crystal. The sample is irradiated with monochromatic light which is scattered either elastically or inelastically. A photon can excite molecular vibrations to a higher level if the frequency of the photon is the same as the difference between the two vibrational states as illustrated in Fig. C.1. After excitation the vibrational state returns to a lower state by emitting a photon. If this state is the same as the initial one, the photon frequency is also the same and the light was scattered elastically. This is also called Rayleigh scattering. Yet, the vibrational state can be higher than the initial one and consequently the frequency of the emitted photon will be smaller than of the exciting photon. This is Stokes scattering and it is an inelastic scattering process. A third possibility is, that a molecular vibration already at a higher level is excited to an even higher state and that after photon emission the initial vibrational state is obtained. Then the frequency of the emitted photon will be larger than the frequency of the exciting photon. This is also an inelastic scattering event and is called Anti-Stokes scattering.

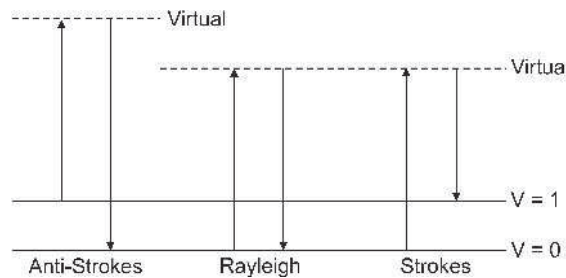


**Figure C.1:** Possible excitations of molecular vibrations. Image taken modified from [126].

In the first case, the elastic or Rayleigh scattering, the frequency of the light does not change. However, the frequency of the light changes if it is scattered inelastically,

### C. Raman spectroscopy

i.e. energy is transferred to the crystal during the scattering process (Stokes and Anti-Stokes scattering). Since Anti-Stokes scattering requires an already excited state, its intensity is significantly lower than for the Stokes scattering. The frequency change caused by the inelastic scattering is the Raman shift.

Raman spectra are showing the intensity of the Raman shift in terms of wavenumber  $\bar{\nu}$ . The wavenumber is defined as  $\bar{\nu} = 1/\lambda = \nu/c$ . The observed bands in the Raman spectra correspond to molecular vibration frequencies. The spectra in this thesis were analyzed by the fingerprint method. The reference of Raman shifts given in Tab. C.1 is compared to the measured spectra in order to determine the polytypes.

**Table C.1:** Raman shifts of various SiC polytypes. Table taken from [128].

polytype	$x = q/q_B$	frequency ( $\text{cm}^{-1}$ )			
		planar acoustic FTA	planar optic FTO	axial acoustic FLA	axial optic FLO
3C	0	-	796	-	972
2H	0	-	799	-	968
	1	264	764	-	-
4H	0	-	796	-	964
	2/4	196, 204	776	-	-
	4/4	266		610	838
6H	0	-	797	-	965
	2/6	145, 150	789	-	-
	4/6	236, 241		504, 514	889
	6/6	266	767	-	-
8H	0	-	796	-	970
	2/8	112, 117	793	-	-
	4/8	203		403, 411	917, 923
	6/8	248, 252		-	-
	8/8	266	767	-	-
15R	0	-	797	-	965
	2/5	167, 173	785	331, 337	932, 938
	4/5	255, 256	769	569, 577	860
21R	0	-	797	-	967
	2/7	126, 131	791	241, 250	
	4/7	217, 220	780	450, 458	905, 908
	6/7	261	767	590, 594	

## D. Field emission gun scanning electron microscopy (FEG-SEM)

Electrically conductive sample surfaces can be imaged by scanning electron microscopy (SEM). The resolution of the SEM is about a few nm and the magnification can be set between 10x - 500 000x.

Fig. D.1 shows a schematic drawing of a SEM. In the used Quanta 250 SEM the electron beam is generated by a field emission gun (FEG). A high electric field is applied to a very sharp metallic tip and as a result electrons are drawn off the metal due to the tunneling effect. The brightness of the FEG is much higher ( $\sim 5 \cdot 10^8 \text{ Acm}^{-2}\text{sr}$ ) than for a thermoionic emission gun ( $\sim 5 \cdot 10^5 \text{ Acm}^{-2}\text{sr}$ ) but requires a high vacuum to avoid emission instabilities due to residual gas [126]. The condenser lenses demagnify the electron beam. The objective lens focus the beam on the sample surface.

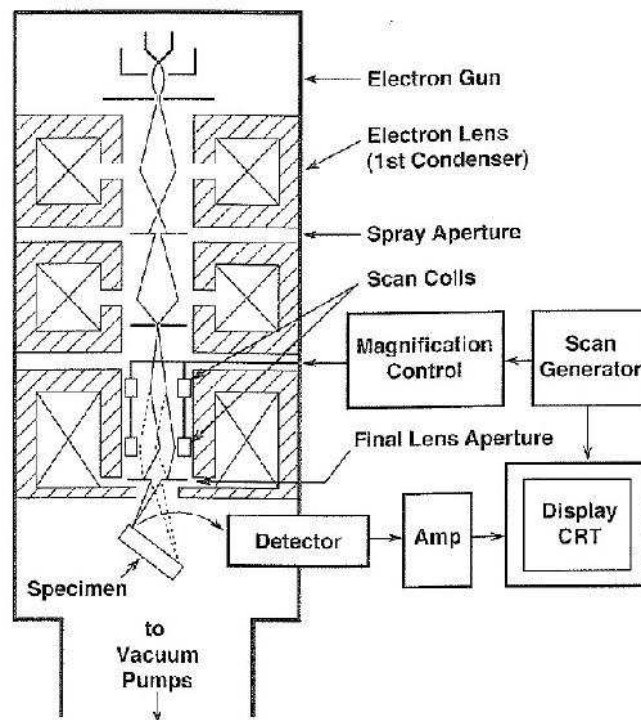


**Figure D.1:** Schematic drawing of a SEM. Image taken from [129].

The electron beam interacts with the specimen surface in various ways. Inelastic scattering causes the emission of secondary electrons (SE) from atoms in the sample. Due to their low energy, only SE generated close to the surface can be detected. Therefore, the SE are used to obtain topographic images.

### *E. High resolution transmission electron microscopy (HRTEM)*

Electrons of the incident beam can also be elastically scattered by the nuclei of the sample atoms. These backscattered electrons (BSE) give information on the chemical composition as the probability of backscattering is depending on the atomic number.

Elements can be further detected by emitted X-rays. The electrons of the beam can eject core electrons of atoms in the sample. An electron of this atoms in a higher state can fall to the lower state of the ejected electron. Since there is an energy difference between these two states, this process is accompanied by the emission of a X-ray photon. The energy of this photon is characteristic for the element and can be detected by a detector. Hence, chemical compositions of a sample can be analyzed.

The SEM is a popular tool in science due to the multiple possibilities to image and characterize samples. However, in the case of SiC, its application is limited. The electron beam reacts with residuals of the vacuum pump which cause a carbonization of the surface. Furthermore, exact height information of the sample surface cannot be extracted. Also the spiral steps are hard to image, as the small step height only generates a low contrast. The advantage of the SEM is that it can image a larger area than the AFM.

## **E. High resolution transmission electron microscopy (HRTEM)**

Atomic structures can be imaged by high resolution transmission electron microscopy (HRTEM). The resolution limit of the used JEOL 2010 is 1.9 Å.

Fig. E.1 shows a schematic drawing of a TEM. An electron beam is generated by a field emission gun (see appendix D.). The beam is demagnified by the condenser lenses. The intermediate lens is used to switch between image and diffraction mode. Finally, the image is magnified on the detector or fluorescent screen by the projector lens.

In general, the electron scattering on the sample causes two different types of contrast. The electrons of the beam can be scattered by the atomic nuclei in the sample. The contrast created by this scattering depends on sample thickness and density. The contrast is controlled by the scattered electrons which can pass the objective aperture.

Images can also be generated by the diffraction contrast. Electrons also follow Bragg's law ( $n\lambda = 2d\sin\theta$ ) and if the conditions this law are fulfilled constructive diffraction occurs. The magnetic lenses below the sample can be adjusted to view the diffraction pattern on the screen, which is the diffraction mode. Moreover, the



## A Appendix

optical path can be changed to the image mode so that either the transmitted or diffracted beam can be used to generate the image. Bright field images are obtained when the diffracted beams are blocked by an aperture. For dark field images, only one diffracted beam is used for the image.

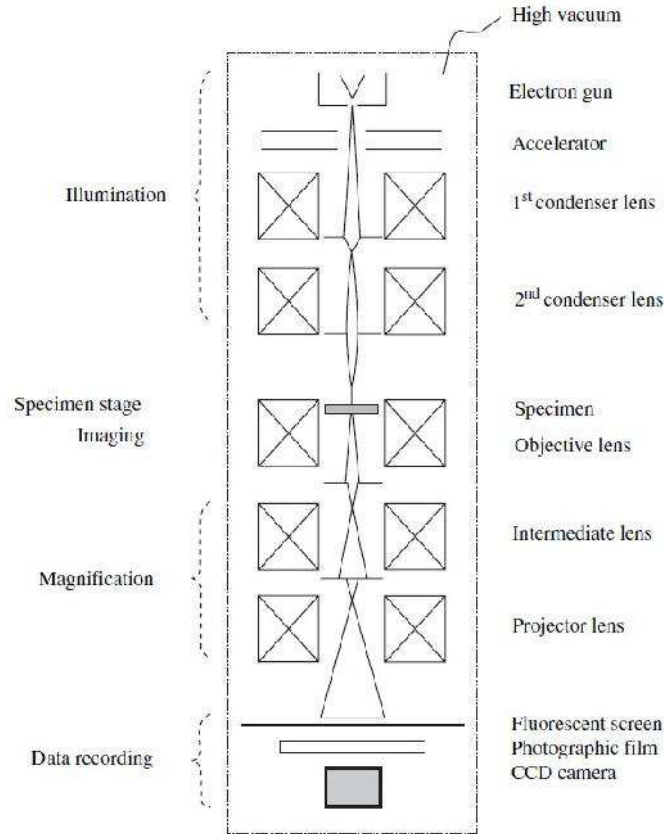


**Figure E.1:** Schematic drawing of TEM. Image taken from [129].

High resolution images are obtained from two electron beams with different phases. The diffracted beam changes its phase after passing crystalline sample with periodic lattice (Fig. E.2) while the direct beam maintains its phase. The image is formed by the recombination of these two beams.

Samples must be sufficiently thin, around 100 nm depending on the atomic weight, for the TEM analysis. If the sample is too thick, the electron beam is absorbed. A sample can be prepared by the sandwich method. For this, the thickness is reduced by polishing. Then, two slices of the sample are glued with their surfaces facing each other. A hole is created at the interface of these two slices by ion beam milling with low angle (about  $4^\circ$ ). The thickness at this hole is thin enough for the TEM. It is clear that this technique requires a homogeneous surface. In order to prepare a slice of a certain area on a sample, focused ion beam milling is

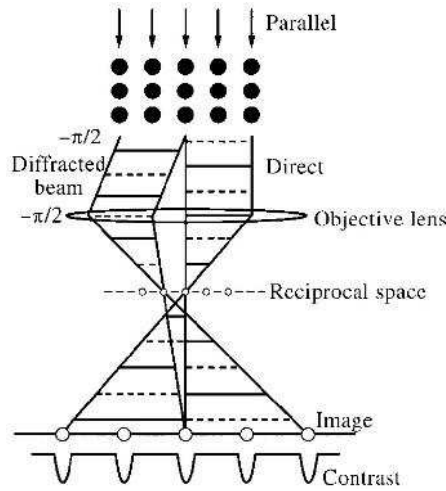


**Figure E.2:** Formation of a phase contrast image by HRTEM. Image taken from [129].

performed. The region of interest is identified by the SEM. A platinum or gold layer is deposited to protect the sample from the ion bombardment of the following ion milling. Although this technique is also employed to analyze surfaces by TEM, we were not able to prepare a sample without creating an amorphous layer on the utter surface.

## F. X-ray diffraction

The structure and phases of crystalline samples can be studied by X-ray diffraction. A Bruker D8 Advance diffractometer with copper source in the  $\theta$ - $2\theta$  geometry was used in the present work. Fig. F.1 shows an illustration of the geometric arrangement.

X-rays are generated in a tube by accelerating electrons towards a target. The deceleration of the electrons in the target produces the white X-rays with a large range of wavelengths. The smallest wavelength corresponds to the maximum acceleration voltage of the electrons. An incident electron can also excite another electron in the inner shell of an atom to higher state. When the electron falls back to its initial state, a characteristic X-ray with a specific wavelength is emitted. Apparently, this wavelength depends on the electronic configuration of the atom and is hence depended on the element. The most common target materials are chromium, iron, copper and molybdenum.

Soller slits are collimating the X-rays generated by the source. On the sample, the X-rays are diffracted according to Bragg's law ( $n\lambda = 2d\sin\theta$ ). A monochromator

## A Appendix

in front of the detector let only pass the  $K\alpha$  radiation.

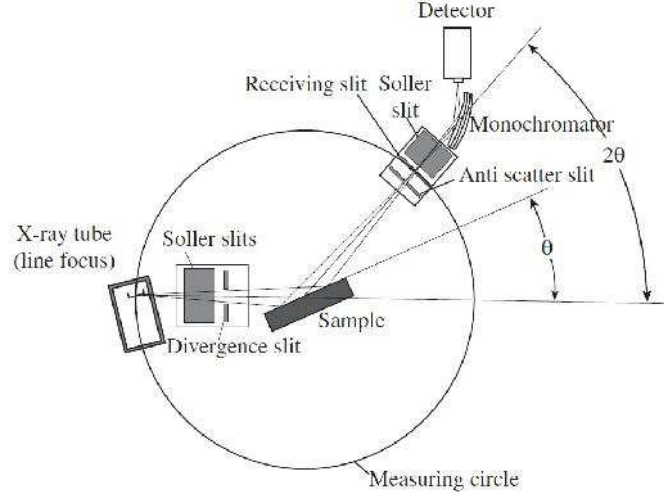


**Figure F.1:** Schematic illustration of an X-ray diffractometer. Image taken from [126].

The sample is rotated during measurements and hence the measured spectrum shows the X-ray intensity as a function of  $2\theta$ . As the diffraction angle  $\theta$  depends on the plane spacing of the crystal the obtained spectra are unique for each crystalline phase. The phase(s) of the crystal can be identified by comparing the spectra with the data of a database.

## G. Laue diffraction

The orientation of a single crystal can be determined by X-ray diffraction in Laue geometry. Contrary to the  $\theta$ - $2\theta$  method introduced in the previous section, a transmission and not reflection geometry is employed. Furthermore, the X-ray beam is polychromatic in order to get as many reflexes as possible. The geometry of the used Philips PW1730 is illustrated in Fig. G.1.

The X-ray beam is diffracted by the sample, which is fixed on a goniometer, and therefore spots corresponding to the lattice planes are generated on the film. The distance  $D$  between the sample and film must be measured for the correct indexing of the spots. The Bragg angle  $\theta_i$  of the  $i$ s spot can be determined by [126]:

$$\theta_i = \frac{1}{2} \tan^{-1} \left( \frac{R_i}{D} \right) \quad (\text{A.1})$$

$R_i$  is the distance from the transmitted beam in the center to the  $i$ s spot.

Inserting this angle into Bragg's law results in [126]

$$d_i = \frac{\lambda}{2 \sin \left[ \frac{1}{2} \tan^{-1} \left( \frac{R_i}{D} \right) \right]} \quad (\text{A.2})$$

where  $d_i$  is the lattice spacing to the corresponding spot.

Computer simulations with the given parameters are compared with the photograph (Fig. G.2). The tilt of the sample can be corrected, if necessary, to perfectly orientate the sample. In our case this was not necessary, as the Laue diffraction was only performed to determine the crystallographic directions on the sample. The stacking of SiC can only be observed by HRTEM if the sample was cut in the right direction, *e.g.* perpendicular to  $[11\bar{2}0]$ .

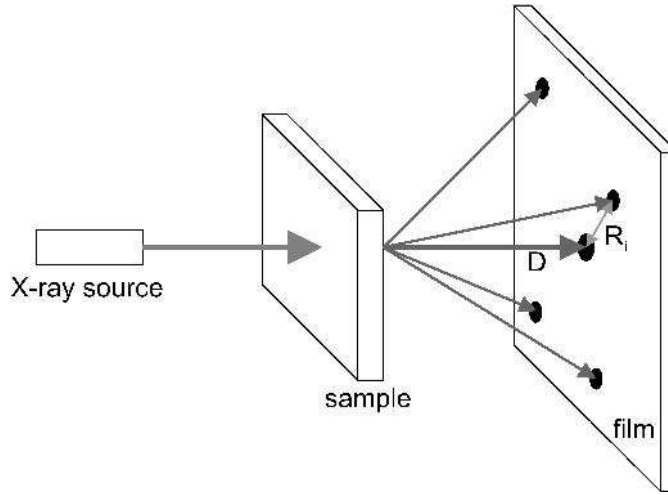


**Figure G.1:** The Laue geometry for X-ray diffraction. Image taken modified from [126].

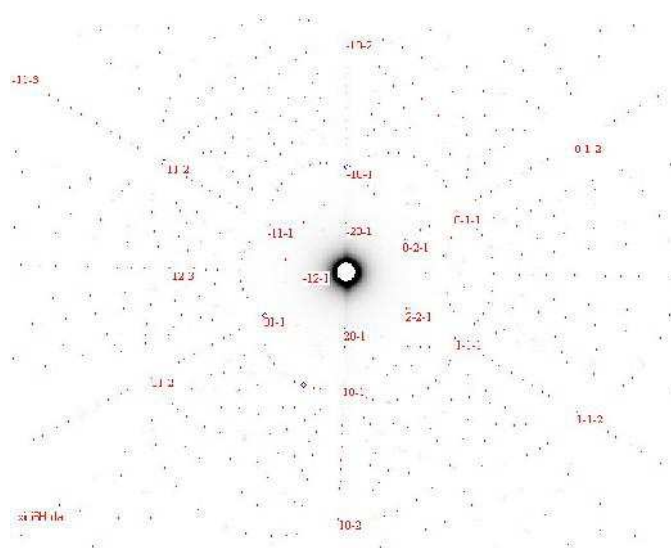


**Figure G.2:** A Laue photograph of a SiC sample with the corresponding simulation.

# Bibliography

- [1] Vijay Balakrishna, Albert A. Burk, Michael J. O'Loughlin, M. F. Brady, Carter Jr, Calvin H, R. T. Leonard, Valeri F. Tsvetkov, Adrian R. Powell, D. P. Malta, Joseph J. Sumakeris, Michael J. Paisley, C. Basceri, Elif Berkman, Y. Khlebnikov, E. Deyneka, H. McD Hobgood, I. Khlebnikov, and C. Balkas. Defect Status in SiC Manufacturing. *Materials Science Forum*, **615-617**:3–6, July 2009.
- [2] F. C. Frank. The influence of dislocations on crystal growth. *Discussions of the Faraday Society*, **5**:48–54, January 1949.
- [3] A. R. Verma. Spiral Growth on Carborundum Crystal Faces. *Nature*, **167**(4258):939, June 1951.
- [4] S. Amelinckx. Spiral Growth on Carborundum Crystal Faces. *Nature*, **167**(4258):939–940, June 1951.
- [5] W. K. Burton, N. Cabrera, and F. C. Frank. The Growth of Crystals and the Equilibrium Structure of their Surfaces. *Philosophical Transactions of the Royal Society of London. Series A, Mathematical and Physical Sciences*, **243**(866):299–358, 1951.
- [6] N. Cabrera and M. M. Levine. XLV. On the dislocation theory of evaporation of crystals. *Philosophical Magazine*, **1**(5):450–458, 1956.
- [7] N. Cabrera and R. V. Coleman. Theory of crystal growth from vapor. In J. J. Gilman, editor, *The Art and Science of Growing Crystals*. John Wiley & Sons Inc, 1963.
- [8] Alex Redinger, Oliver Ricken, Philipp Kuhn, Andreas Rätz, Axel Voigt, Joachim Krug, and Thomas Michely. Spiral Growth and Step Edge Barriers. *Phys. Rev. Lett.*, **100**:35506, Jan 2008.
- [9] Alain Karma and Mathis Plapp. Spiral Surface Growth without Desorption. *Phys. Rev. Lett.*, **81**:4444–4447, Nov 1998.

## Bibliography

- [10] B. Ranguelov, J.J. Métois, and P. Müller. Spirals on Si(111) at sublimation and growth: REM and LODREM observations. *Surface Science*, **600**(21):4848 – 4854, 2006.
- [11] J.J. Berzelius. Untersuchung über die Flußspathsäure und deren merkwürdigsten Verbindungen. *Ann. Phys. Chemie Folge 1*, **77**.
- [12] H. Moissan. *C.R. Acad. Sci. Paris*, **140**:405, 1905.
- [13] E. G. Acheson, 1893. US492767.
- [14] H.J. Round. *Electr. World*, **19**:309, 1907.
- [15] H. Baumhauer. Über die Kristalle des Carborundums. *Z. Kristallogr.*, **50**, 1912.
- [16] Gmelin Handbook of Inorganic Chemistry, 1984.
- [17] Jan Anthony Lely. *Ber. Dtsch. Keram. Ges.*, **32**:229–236, 1955.
- [18] G. Dhanaraj, K Byrappa, P. Vishwanath, and M. Dudley, editors. *Springer Handbook of Crystal Growth*. Springer Berlin Heidelberg, 2010.
- [19] Yu.M. Tairov and V.F. Tsvetkov. Investigation of growth processes of ingots of silicon carbide single crystals. *Journal of Crystal Growth*, **43**(2):209–212, March 1978.
- [20] <http://www.cree.com/>.
- [21] Magnus Willander, Milan Friesel, Qamar-ul Wahab, and Boris Straumal. Silicon carbide and diamond for high temperature device applications. *Journal of Materials Science: Materials in Electronics*, **17**(1):1–25, 2006.
- [22] P. Roussel. SiC power devices: if only we had a switch. *semiconductorTODAY*, **2**(5):40–42, june 2007.
- [23] <http://www.infineon.com/>.
- [24] B. Gentinne, J.-P. Eggermont, D. Flandre, and J.-P. Colinge. Fully depleted SOI-CMOS technology for high temperature IC applications. *Materials Science and Engineering: B*, **46**(1–3):1–7, 1997.
- [25] J.C. Zolper. A review of junction field effect transistors for high-temperature and high-power electronics. *Solid-State Electronics*, **42**(12):2153 – 2156, 1998.

- [26] W. Bergner, F. Bjoerk, D. Domes, and G. Deboy. Infineon's 1200V SiC JFET - The New Way of Efficient and Reliable High Voltages Switching. Technical report, Infineon Technologies AG, 2011.
- [27] G. Dhanaraj, X.R. Huang, M. Dudley, V. Prasad, and R.-H. Ma. In K. Byrappa and T. Ohachi, editors, *Crystal Growth Technology*. Springer-Verlag Berlin Heidelberg New York, 2003.
- [28] Jean Camassel, Sylvie Contreras, and Jean-Louis Robert. SiC materials: a semiconductor family for the next century. *Comptes Rendus de l'Académie des Sciences - Series IV - Physics*, **1**(1):5 – 21, 2000.
- [29] P. Pirouz and J.W. Yang. Polytypic transformations in SiC: the role of TEM. *Ultramicroscopy*, **51**(1 - 4):189 – 214, 1993.
- [30] Eric Pearson, Tadayoshi Takai, Timur Halicioglu, and William A. Tiller. Computer modeling of Si and SiC surfaces and surface processes relevant to crystal growth from the vapor. *Journal of Crystal Growth*, **70**(1 - 2):33 – 40, 1984.
- [31] D. Zhuang and J.H. Edgar. Wet etching of GaN, AlN, and SiC: a review. *Materials Science and Engineering: R: Reports*, **48**(1):1 – 46, 2005.
- [32] Helmut Föll. *Agglomerate von Zwischengitteratomen (Swirl-Defekte) in Silizium - ihre Bedeutung für Grundlagenforschung und Technologie*. PhD thesis, Max-Planck-Institut für Metal Physics in Stuttgart, University of Stuttgart, 1976.
- [33] D. Hull and D.J. Bacon, editors. *Introduction to dislocations*. Butterworth-Heinemann, 4th edition, 2001.
- [34] J. Weertman and Julia R. *Théorie élémentaire des dislocations*. Masson et Cie, 1970.
- [35] F. C. Frank. Capillary equilibria of dislocated crystals. *Acta Crystallographica*, **4**(6):497–501, Nov 1951.
- [36] K. Kamitani, M. Grimsditch, J. C. Nipko, C.-K. Loong, M. Okada, and I. Kimura. The elastic constants of silicon carbide: A Brillouin-scattering study of 4H and 6H SiC single crystals. *Journal of Applied Physics*, **82**(6):3152–3154, 1997.



## Bibliography

- [37] P.G. Neudeck and J.A. Powell. Performance limiting micropipe defects in silicon carbide wafers. *Electron Device Letters, IEEE*, **15**(2):63 –65, feb. 1994.
- [38] A.R. Powell and L.B. Rowland. SiC materials-progress, status, and potential roadblocks. *Proceedings of the IEEE*, **90**(6):942 – 955, June 2002.
- [39] Sakiko Kawanishi, Takeshi Yoshikawa, and Toshihiro Tanaka. Equilibrium Phase Relationship between SiC and a Liquid Phase in the Fe-Si-C System at 1523-1723 K. *Materials Transactions*, **50**(4):806–813, 2009.
- [40] H. Kleykamp and G. Schumacher. The Constitution of the Silicon-Carbon System. *Berichte der Bunsengesellschaft für physikalische Chemie*, **97**(6):799–804, 1993.
- [41] Dieter H Hofmann and Matthias H Müller. Prospects of the use of liquid phase techniques for the growth of bulk silicon carbide crystals. *Materials Science and Engineering: B*, **61-62**(0):29 – 39, 1999.
- [42] H. Nowotny, E. Parthé, R. Kieffer, and F. Benesovsky. Das Dreistoffsystem: Molybdän-Silizium-Kohlenstoff. *Monatshefte für Chemie / Chemical Monthly*, **85**:255–272, 1954. 10.1007/BF00900444.
- [43] V. D. Heydemann, N. Schulze, D. L. Barrett, and G. Pensl. Growth of 6H and 4H silicon carbide single crystals by the modified Lely process utilizing a dual-seed crystal method. *Applied Physics Letters*, **69**(24):3728–3730, 1996.
- [44] Y.M. Tairov and V.F. Tsvetkov. Progress in controlling the growth of polytypic crystals. *Progress in Crystal Growth and Characterization*, **7**(1-4):111 – 162, 1983.
- [45] Dick Lundqvist. On the Crystal Structure of Silicon Carbide and its Content of Impurities. *Acta Chemica Scandinavica*, **2**:177–191, 1948.
- [46] W.F. Knippenberg. *Philips Research Reports*, **18**(161), 1963.
- [47] Yoshizo Inomata, Mamoru Mitomo, Zenzaburo Inoue, and Hirokichi Tanaka. Thermal Stability of the Basic Structures of SiC(*in japanese*). *Journal of the Ceramic Association, Japan*, **77**:130–135, 1969.
- [48] *Crystal growth for beginners*. World Scientific Publishing Co. Pte. Ltd., 2nd edition, 2003.

- [49] Gert Ehrlich and F. G. Hudda. Atomic View of Surface Self-Diffusion: Tungsten on Tungsten. *The Journal of Chemical Physics*, **44**(3):1039–1049, 1966.
- [50] Richard L. Schwoebel. Step Motion on Crystal Surfaces. II. *Journal of Applied Physics*, **40**(2):614–618, 1969.
- [51] D. Chaussende, P. J. Wellmann, and M. Pons. Status of SiC bulk growth processes. *Journal of Physics D: Applied Physics*, **40**(20):6150, 2007.
- [52] Irina Galben-Săndulache. *Cristallogenèse de carbure de silicium cubique (SiC-3C) en phase gazeuse*. PhD thesis, Ecole Doctorale I-MEP<sup>2</sup>, 2010.
- [53] E. Kaldis and M. Piechotka. Bulk Crystal Growth by Physical Vapour Transport. In D. T. J. Hurle, editor, *Handbook of Crystal Growth*, volume 2. Elsevier Science Ltd, 1994.
- [54] R. Yakimova, M. Syväjärvi, T. Iakimov, H. Jacobsson, R. Råback, A. Vehanen, and E. Janzén. Polytype stability in seeded sublimation growth of 4H-SiC boules. *Journal of Crystal Growth*, **217**(3):255 – 262, 2000.
- [55] G. Augustine, McD. Hobgood, V. Balakrishna, G. Dunne, and R. H. Hopkins. Physical Vapor Transport Growth and Properties of SiC Monocrystals of 4H Polytype. *physica status solidi (b)*, **202**(1):137–148, 1997.
- [56] M. C. Righi, C. A. Pignedoli, G. Borghi, R. Di Felice, C. M. Bertoni, and A. Catellani. Surface-induced stacking transition at SiC(0001). *Phys. Rev. B*, **66**:045320, Jul 2002.
- [57] Shohei Ogura, Katsuyuki Fukutani, Masuaki Matsumoto, Tatsuo Okano, Michio Okada, and Takaaki Kawamura. Dendritic to non-dendritic transitions in Au islands investigated by scanning tunneling microscopy and Monte Carlo simulations. *Phys. Rev. B*, **73**:125442, Mar 2006.
- [58] Thomas Michely and Joachim Krug. *Islands, Mounds and Atoms*. Springer, 2004.
- [59] U. Starke, J. Schardt, J. Bernhardt, M. Franke, and K. Heinz. Stacking Transformation from Hexagonal to Cubic SiC Induced by Surface Reconstruction: A Seed for Heterostructure Growth. *Phys. Rev. Lett.*, **82**:2107–2110, Mar 1999.

## Bibliography

- [60] Andreas Fissel. Thermodynamic considerations of the epitaxial growth of SiC polytypes. *Journal of Crystal Growth*, **212**:438 – 450, 2000.
- [61] M. Klaua. Electron Microscopic Investigations of Surface Diffusion and Nucleation of Au on Ag (111). In A. A. Chernov, editor, *Rost Kristallov / Growth of Crystals*, volume 11, pages 60–63. Springer US, january 1979.
- [62] S. J. Liu, Hanchen Huang, and C. H. Woo. Schwoebel-Ehrlich barrier: from two to three dimensions. *Applied Physics Letters*, **80**(18):3295–3297, 2002.
- [63] Y.-W. Mo, J. Kleiner, M.B. Webb, and M.G. Lagally. Surface self-diffusion of Si on Si(001). *Surface Science*, **268**(1-3):275 – 295, 1992.
- [64] Bert Voigtländer, Andre Zinner, Thomas Weber, and Hans P. Bonzel. Modification of growth kinetics in surfactant-mediated epitaxy. *Phys. Rev. B*, **51**:7583–7591, Mar 1995.
- [65] Shunta Harada, Alexander, Kazuaki Seki, Yuji Yamamoto, Can Zhu, Yuta Yamamoto, Shigeo Arai, Jun Yamasaki, Nobuo Tanaka, and Toru Ujihara. Polytype Transformation by Replication of Stacking Faults Formed by Two-Dimensional Nucleation on Spiral Steps during SiC Solution Growth. *Crystal Growth & Design*, **12**(6):3209–3214, 2012.
- [66] J. Nishizawa and M. Kimura. Layer growth in GaAs epitaxy. *Journal of Crystal Growth*, **74**(2):331 – 337, 1986.
- [67] Tsunenobu Kimoto and Hiroyuki Matsunami. Surface diffusion lengths of adatoms on 6H-SiC{0001} faces in chemical vapor deposition of SiC. *Journal of Applied Physics*, **78**(5):3132–3137, 1995.
- [68] V. Halpern. Cluster Growth and Saturation Island Densities in Thin-Film Growth. *Journal of Applied Physics*, **40**(11):4627–4636, 1969.
- [69] Willy Dekeyser and Séverin Amelinckx. *Les dislocation et la croissance des cristaux*. Masson et Cie, 1955.
- [70] S. Amelinckx. Growth Mechanism of Carborundum Crystals. *Nature*, **168**(4271):431–431, september 1951.
- [71] B. van der Hoek, J.P. van der Eerden, and K. Tsukamoto. Interpretation of double spirals on silicon carbide. *Journal of Crystal Growth*, **58**(3):545 – 553, 1982.

- [72] Yu. A. Vodakov, E. N. Mokhov, A. D. Roenkov, and D. T. Saidbekov. Effect of crystallographic orientation on the polytype stabilization and transformation of silicon carbide. *physica status solidi (a)*, **51**(1):209–215, 1979.
- [73] Masatoshi Kanaya, Jun Takahashi, Yuichiro Fujiwara, and Akihiro Moritani. Controlled sublimation growth of single crystalline 4H-SiC and 6H-SiC and identification of polytypes by x-ray diffraction. *Applied Physics Letters*, **58**(1):56–58, 1991.
- [74] Taro Nishiguchi, T. Shimizu, Makato Sasaki, S. Oshima, and Shigehiro Nishino. Crystal Growth of 15R-SiC and Various Polytype Substrates. *Materials Science Forum*, **353-356**:69–72, January 2001.
- [75] Hiroshi Harima, Taro Nishiguchi, Makato Sasaki, Shigehiro Nishino, and Sohei Okada. Crystal Growth of 15R-SiC Boules by Sublimation Method. *Materials Science Forum*, **338-342**:115–118, May 2000.
- [76] Sukit Limpijumnong and Walter R. L. Lambrecht. Total energy differences between SiC polytypes revisited. *Phys. Rev. B*, **57**:12017–12022, May 1998.
- [77] C. H. Park, Byoung-Ho Cheong, Keun-Ho Lee, and K. J. Chang. Structural and electronic properties of cubic, 2H, 4H, and 6H SiC. *Phys. Rev. B*, **49**:4485–4493, Feb 1994.
- [78] P. Käckell, B. Wenzien, and F. Bechstedt. Influence of atomic relaxations on the structural properties of SiC polytypes from *ab initio* calculations. *Phys. Rev. B*, **50**:17037–17046, Dec 1994.
- [79] A. Zywietz, K. Karch, and F. Bechstedt. Influence of polytypism on thermal properties of silicon carbide. *Phys. Rev. B*, **54**:1791–1798, Jul 1996.
- [80] C Cheng, Volker Heine, and I L Jones. Silicon carbide polytypes are equilibrium structures. *Journal of Physics: Condensed Matter*, **2**(23):5097, 1990.
- [81] R.A. Stein and P. Lanig. Control of polytype formation by surface energy effects during the growth of SiC monocrystals by the sublimation method. *Journal of Crystal Growth*, **131**(1-2):71 – 74, 1993.
- [82] W. Qian, M. Skowronski, K. Doverspike, L.B. Rowland, and D.K. Gaskill. Observation of nanopipes in  $\alpha$ -GaN crystals. *Journal of Crystal Growth*, **151**(3-4):396 – 400, 1995.

## Bibliography

- [83] A. Baronnet. Sur les origines des dislocations vis et des spirales de croissance dans les micas. *Journal of Crystal Growth*, **19**(3):193 – 198, 1973.
- [84] S. Mardix, A. R. Lang, and I. Blech. On giant screw dislocations in ZnS polytype crystals. *Philosophical Magazine*, **24**(189):683–693, 1971.
- [85] Ajit Ram Verma. Growth spirals and polytypism of silicon carbide crystals. *Zeitschrift für Elektrochemie, Berichte der Bunsengesellschaft für physikalische Chemie*, **56**(4):268–274, 1952.
- [86] St.G. Müller, R.C. Glass, H.M. Hobgood, V.F. Tsvetkov, M. Brady, D. Henshall, J.R. Jenny, D. Malta, and C.H. Carter Jr. The status of SiC bulk growth from an industrial point of view. *Journal of Crystal Growth*, **211**(1-4):325 – 332, 2000.
- [87] M. Dudley, X. R. Huang, W. Huang, A. Powell, S. Wang, P. Neudeck, and M. Skowronski. The mechanism of micropipe nucleation at inclusions in silicon carbide. *Applied Physics Letters*, **75**(6):784–786, 1999.
- [88] D. Hofmann, M. Bickermann, R. Eckstein, M. Kölbl, St. G. Müller, E. Schmitt, A. Weber, and A. Winnacker. Sublimation Growth of Silicon Carbide Bulk Crystals: Experimental and Theoretical Studies on Defect Formation and Growth Rate Augmentation. *Journal of Crystal Growth*, **198-199**:1005–1010, 1999. Part 2.
- [89] J. Heindl, H. P. Strunk, V. D. Heydemann, and G. Pensl. Micropipes: Hollow Tubes in Silicon Carbide. *physica status solidi (a)*, **162**(1):251–262, 1997.
- [90] Xianyun Ma. Superscrew dislocations in silicon carbide: Dissociation, aggregation, and formation. *Journal of Applied Physics*, **99**(6):063513, 2006.
- [91] P. Pirouz. On micropipes and nanopipes in SiC and GaN. *Philosophical Magazine A*, **78**(3):727–736, 1998.
- [92] F. C. Frank and W. T. Read. Multiplication Processes for Slow Moving Dislocations. *Phys. Rev.*, **79**:722–723, Aug 1950.
- [93] C. Chapon and A. Bonissent. Morphologie et distances entre les fronts de croissance d’une spirale polygonisée. *Journal of Crystal Growth*, **18**(1):103 – 106, 1973.
- [94] E. Budevski, G. Staikov, and V. Bostanov. Form and step distance of polygonized growth spirals. *Journal of Crystal Growth*, **29**(3):316 – 320, 1975.

- [95] Ichiro Sunagawa. *Crystals - Growth, Morphology and Perfection*. Camebridge University Press, 2007.
- [96] K.A. Jackson, editor. *Liquid Metals and Solidification*. American Society of Metals, 1958.
- [97] P. Krishna and A. R. Verma. A new polytype of silicon carbide, 57R. Its structure and growth. *Acta Crystallographica*, **15**(4):383–387, 1962.
- [98] P. Krishna and A. R. Verma. On the deduction of silicon-carbide polytypes from screw dislocations. *Zeitschrift für Kristallographie*, **121**(1):36–54, 1965.
- [99] Harald Brune, Holger Röder, Karsten Bromann, Klaus Kern, Joachim Jacobsen, Per Stoltze, Karsten Jacobsen, and Jens Nørskov. Anisotropic corner diffusion as origin for dendritic growth on hexagonal substrates. *Surface Science*, **349**(1):L115 – L122, 1996.
- [100] A. A. Chernov. The Spiral Growth of Crystals. *Soviet Physics Uspekhi*, **4**(1):116, 1961.
- [101] K. Wiesauer and G. Springholz. Spiral growth of PbTe (111) in molecular beam epitaxy far from thermodynamic equilibrium. no longer available online.
- [102] J. J. De Yoreo, T. A. Land, and J. D. Lee. Limits on Surface Vicinality and Growth Rate due to Hollow Dislocation Cores on KDP {101}. *Phys. Rev. Lett.*, **78**:4462–4465, Jun 1997.
- [103] Thierry Ouisse. private communication.
- [104] Hiroyuki Matsunami and Tsunenobu Kimoto. Step-controlled epitaxial growth of SiC: High quality homoepitaxy. *Materials Science and Engineering: R: Reports*, **20**(3):125 – 166, 1997.
- [105] Tsunenobu Kimoto, Akira Itoh, Hiroyuki Matsunami, and Tetsuyuki Okano. Step bunching mechanism in chemical vapor deposition of 6H- and 4H-SiC{0001}. *Journal of Applied Physics*, **81**(8):3494–3500, 1997.
- [106] Tsunenobu Kimoto, Zhi Ying Chen, Satoshi Tamura, Shun ichi Nakamura, Norio Onojima, and Hiroyuki Matsunami. Surface Morphological Structures of 4H-, 6H- and 15R-SiC (0001) Epitaxial Layers Grown by Chemical Vapor Deposition. *Japanese Journal of Applied Physics*, **40**(Part 1, No. 5A):3315–3319, 2001.

## Bibliography

- [107] David J. Larkin, Philip G. Neudeck, J. Anthony Powell, and Lawrence G. Matus. Site-competition epitaxy for superior silicon carbide electronics. *Applied Physics Letters*, **65**(13):1659–1661, 1994.
- [108] Phillip J. Stout. Modeling surface kinetics and morphology during 3C, 2H, 4H, and 6H-SiC (111) step-flow growth. *Journal of Vacuum Science & Technology A: Vacuum, Surfaces, and Films*, **16**(6):3314–3327, 1998.
- [109] Valery Borovikov and Andrew Zangwill. Step bunching of vicinal 6H-SiC{0001} surfaces. *Phys. Rev. B*, **79**:245413, Jun 2009.
- [110] Valeri F. Tsvetkov, R.C. Glass, D. Henshall, D. Asbury, and H. Carter Jr. Calvin. SiC Seeded Boule Growth. *Materials Science Forum*, **264-268**:3–8, February 1998.
- [111] V. Papaioannou, J. Stoemenos, L. Di Cioccio, D. David, and C. Pudda. Study of 4H- and 6H-SiC films grown on off-oriented (0001) SiC substrates. *Journal of Crystal Growth*, **194**(3-4):342 – 352, 1998.
- [112] Noboru Ohtani, Masakazu Katsuno, Jun Takahashi, Hirokatsu Yashiro, and Masatoshi Kanaya. Evolution of macrosteps on 6H – SiC(0001) : Impurity-induced morphological instability of step trains. *Phys. Rev. B*, **59**:4592–4595, Feb 1999.
- [113] Y. H. Xie, G. H. Gilmer, C. Roland, P. J. Silverman, S. K. Buratto, J. Y. Cheng, E. A. Fitzgerald, A. R. Kortan, S. Schuppler, M. A. Marcus, and P. H. Citrin. Semiconductor Surface Roughness: Dependence on Sign and Magnitude of Bulk Strain. *Phys. Rev. Lett.*, **73**:3006–3009, Nov 1994.
- [114] J. Tersoff, Y. H. Phang, Zhenyu Zhang, and M. G. Lagally. Step-Bunching Instability of Vicinal Surfaces under Stress. *Phys. Rev. Lett.*, **75**:2730–2733, Oct 1995.
- [115] J. E. Guyer and P. W. Voorhees. Morphological Stability of Alloy Thin Films. *Phys. Rev. Lett.*, **74**:4031–4034, May 1995.
- [116] G.H. Gilmer. Growth on imperfect crystal faces: I. Monte-Carlo growth rates. *Journal of Crystal Growth*, **36**(1):15 – 28, 1976.
- [117] Hyeong-Chai Jeong and Ellen D. Williams. Steps on surfaces: experiment and theory. *Surface Science Reports*, **34**(6-8):171 – 294, 1999.

- [118] W. W. Pai, N. C. Bartelt, and J. E. Reutt-Robey. Fluctuation kinetics of an isolated Ag(110) step. *Phys. Rev. B*, **53**:15991–15996, Jun 1996.
- [119] N.C. Bartelt, J.L. Goldberg, T.L. Einstein, and Ellen D. Williams. The equilibration of terrace width distributions on stepped surfaces. *Surface Science*, **273**(1-2):252 – 260, 1992.
- [120] Mirang Yoon, S. G. J. Mochrie, M. W. Tate, S. M. Gruner, and E. F. Eikenberry. Anisotropic Coarsening of Periodic Grooves: Time-Resolved X-Ray Scattering. *Phys. Rev. Lett.*, **80**:337–340, Jan 1998.
- [121] C. Alfonso, J.M. Bermond, J.C. Heyraud, and J.J. Métois. The meandering of steps and the terrace width distribution on clean Si(111): An in-situ experiment using reflection electron microscopy. *Surface Science*, **262**(3):371 – 381, 1992.
- [122] K. Sudoh, T. Yoshinobu, H. Iwasaki, and Ellen D. Williams. Step Fluctuations on Vicinal Si(113). *Phys. Rev. Lett.*, **80**:5152–5155, Jun 1998.
- [123] Pierre Müller and Andrés Saúl. Elastic effects on surface physics. *Surface Science Reports*, **54**(5 - 8):157 – 258, 2004.
- [124] B. Joós, T. L. Einstein, and N. C. Bartelt. Distribution of terrace widths on a vicinal surface within the one-dimensional free-fermion model. *Phys. Rev. B*, **43**:8153–8162, Apr 1991.
- [125] Ellen D Williams. Surface steps and surface morphology: understanding macroscopic phenomena from atomic observations. *Surface Science*, 299?300(0):502 – 524, 1994.
- [126] Yang Leng. *Materials Characterization - Introduction to Microscopic and Spectroscopic Methods*. John Wiley and Sons, 2008.
- [127] Peter Eaton and Paul West. *Atomic Force Microscopy*. Oxford University Press, 2010.
- [128] S. Nakashima and H. Harima. Raman Investigation of SiC Polytypes. *physica status solidi (a)*, **162**(1):39–64, 1997.
- [129] Joseph Goldstein, Dale E. Newbury, David C. Joy, Charles E. Lyman, Patrick Echlin, Eric Lifshin, Linda Sawyer, and J.R. Michael. *Scanning Electron Microscopy and X-ray Microanalysis*. Kluwer Academic / Plenum Publishers, Third Edition edition, 2003.





# List of Figures

1.1	Intrinsic carrier concentration as function of temperature of several semiconductors. Image taken from [25]. . . . .	7
1.2	Illustration of a SiC tetrahedron (a). The carbon atom (brown) is coordinated with four silicon atoms (blue). Turning the tetrahedron by $60^\circ$ (b) results in a different orientation that make the occurrence of different stacking in the crystal possible as illustrated in (c) for 6H SiC. . . . .	9
1.3	Stackings of the most widespread polytypes of SiC. The white circles correspond to silicon and the black filled circles to carbon atoms. . .	10
1.4	The stacking of the 15R polytype observed by TEM. The circles on the left illustrate the stacking of the tetrahedrons. . . . .	11
1.5	The surfaces of on-axis SiC crystals are either silicon (blue spheres) or carbon (brown spheres) terminated thus inducing polarity to the crystal. The silicon face is the (0001) plane and the carbon face the (000 $\bar{1}$ ) plane. . . . .	11
1.6	Typical defects in crystals: a) interstitial impurity atom, b) edge dislocation, c) self interstitial atom, d) vacancy, e) precipitate of impurity atoms, f) vacancy type of dislocation loop, g) interstitial type dislocation loop, h) substitutional impurity atom. Image taken from [32]. . . . .	12
1.7	Visualisation of dislocations. (a) A perfect simple cubic crystal. In the lower right atoms are represented by black filled circles and the bondings between them by springs. (b) Introducing a half-plane in ABCD results in a edge dislocation. (c) A partial slip of the crystal creates a screw dislocation. Image taken from [33]. . . . .	14
1.8	How to determine the Burgers vector for edge and screw dislocations. (a) Burgers circuit round an edge dislocation. (b) Same circuit in a perfects crystal. The difference in the path of both circuits gives the Burgers vector. (c) Burgers circuit round a screw dislocation and (d) same circuit in a perfect crystal. The path between start and end defines the vector. Image taken from [33]. . . . .	15

## List of Figures

1.9	(a)Removing (partially) a close packed layer in a fcc crystal results here in the formation of $\frac{1}{3}[111]$ Frank partial dislocation. (b) The slip of A atoms to B positions on the line LM creates a Shockley partial dislocation with $\vec{b} = 1/6[1\bar{2}1]$ . Image taken from [33]. . . . .	15
1.10	The images show the (111) plane of a fcc crystal. (a) A Shockley partial can be created if a (111) plane partially slips e.g. from a B to C position. (b) Illustration of a stacking fault caused by a Shockley partial. Images taken from [33] and [34]. . . . .	16
1.11	Micropipe observed by AFM. The radius of the core is 370 nm. . . . .	17
1.12	Evolution of the micropipe density of Cree wafers. Image taken from [38]. . . . .	18
1.13	Phase diagram of SiC at atmospheric pressure. V denotes vapour and L liquid. Retraced image from [42]. . . . .	19
1.14	Two diagrams showing temperature ranges for growing different polytypes. Both authors agree that the hexagonal and rhombohedral polytypes occur mixed. But in (a) 3C is formed in non-equilibrium conditions contrary to (b) where nothing is remarked in addition. Images retraced from [46] and [47]. . . . .	19
1.15	(a) The original Lely method and (b) the modified Lely method or physical vapour transport (PVT) technique: (1) carbon from decomposed SiC, (2) SiC lumps, (3) deposited SiC on graphite walls, (4) SiC platelets, (5) graphite crucible, (6) powder source, (7) seed, (8) grown crystal. (c) Temperature gradient of the PVT technique. Images redrawn from [27] [18] [19]. . . . .	21
1.16	6H SiC growth spiral. . . . .	22
1.17	The fluxes in a segment $dx$ on the crystal surface. . . . .	22
1.18	The concentration profile on a spiral terrace. . . . .	24
1.19	The concentration profile on terrace with (solid) and without (dashed) Ehrlich-Schwoebel (ES) effect for $\lambda_s < \Lambda/2$ . . . . .	26
1.20	A two dimensional disc with radius $\rho$ expands by $d\rho$ . . . . .	26
1.21	At low supersaturation the growth rate of a spiral is a parabolic function of the supersaturation. Above the characteristic supersaturation $\sigma_c$ the growth rate increases linear with the supersaturation. Image taken from [48]. . . . .	30
2.1	Schematic drawing of the basic PVT setup. . . . .	32

2.2	A schematic section of the used crucible.(1) plug to fix substrate and avoid its evaporation; the small black rectangle below is the substrate (2) sample holder (3) cone to confine the flux towards the substrate (4) SiC powder (5) crucible (6) base (7) heating element (8) thermal insulation (9) spacer (10) top cover. . . . .	32
2.3	The crucible Matryoshka. The parts shown are (from left to right): Thermal insulation, heating element with top cover, powder crucible on base, spacer, cone, sample holder and plug. . . . .	33
2.4	In order to determine the defect density of the substrates, they were etched 5 minutes in KOH at 550 °C. (a) Surface of an etched substrate. (b) After image processing with <i>ImageJ</i> the defects were counted. . . . .	34
2.5	Recorded data of a typical growth process. (1) Manual heating until the pyrometer starts temperature reading (2) Automatic heat ramp (3) Deposition (4) Cool down. . . . .	34
2.6	The crucible at 2100 °C. . . . .	35
2.7	Map created from several optical images. . . . .	36
2.8	Example of a 6H SiC Raman spectrogram. . . . .	36
2.9	Taking a picture by FEG-SEM creates a non-removable carbon layer on the surface. (a) detail of an AFM image showing the carbon layer deposited by FEG-SEM (bright areas). (b) Re-scanning the same area with a lower magnification also reveals a deposited carbon layer in the FEG-SEM. Note that the images are not showing the same spiral. . . . .	37
2.10	The growth rate is almost inversely proportional to the pressure for Si- (open circles) and C-face (open triangles and squares). The exponent of the fit (black line) is -0.83 and thus close to -1. . . . .	38
2.11	Nucleation on a 6H spiral (Si-face). The distance between next neighbouring nuclei $d$ and the relative position $y_1$ and $y_2$ of the nuclei on the terrace were measured. . . . .	41
2.12	The shape of the nuclei could not be related to deposition pressure or seed polarity. (a) 6H spiral Si-face, 300 mbar. (b) 6H spiral Si-face, 150 mbar. (c) 15R spiral C-face, 200 mbar. . . . .	41
2.13	Samples used for the analysis. (a) and (b) are showing a spiral on Si-face grown at 250 mbar. (b) and (c) are images of the C-face sample grown at 400 mbar. . . . .	42
2.14	Raman spectra (laser 514 nm) of the spirals shown in Fig. 2.13. Both spectra show only peaks of the 6H polytype. . . . .	44

## List of Figures

2.15	The nuclei appear cumulated at the descending step of a terrace on the C-face. Next to the rising step less nuclei are counted. Latter is similar for the nuclei on Si-face but also at the descending step less nuclei are observed than in the centre of the terrace. . . . .	44
2.16	Schematic illustration of the Ehrlich-Schwoebel effect. (a) Top view on a fcc crystal. (b) Section of the left image with potential diagram. Image taken modified from [48]. . . . .	45
2.17	The distance of the nuclei to the rising (red, $d_1$ ) and descending (blue, $d_2$ ) edge. The inset illustrates the distances of the nuclei to the edges. . . . .	47
2.18	Histograms of the next nucleus distances on the Si- and C-face. . .	48
3.1	Simple and double spirals with $b = 1$ have one or two branches respectively and no hollow core. . . . .	52
3.2	The Raman spectra of two spirals grown on C-face 6H seeds prove the presence of the 6H (filled circles), 15R (filled squares) or 4H (filled rhombi) polytype. The 6H fingerprint is visible in both cases. Note that some peaks of different polytypes have (almost) the same wavenumber. In such a case only the wavenumber of the 6H polytype is given. All relevant peak positions can be found in the appendix (Tab. C.1). . . . .	53
3.3	Spirals with likewise sign agglomerate and may form a micropipe. On these images two or more spirals are present. . . . .	55
3.4	The Frank-Read mechanism of dislocation multiplication. Image taken from [33]. . . . .	56
3.5	Two spirals with different sign create a Frank-Read source. When the steps of two closely located spirals meet, a joint step is created which results in a loop upon crystal growth. The joint steps are indicated by arrows. . . . .	57
3.6	If many spirals are agglomerated, complex surface structures are formed. . . . .	58
3.7	The degree of polygonization clearly depends on the polytype: (a) 4H (C-face), (b) 6H double (Si-face), (c) 6H simple (Si-face), (d) 15R spiral (C-face). . . . .	59
3.8	The polygonization of a 6H double spiral on the C-face decreases continuously with increasing distance to the centre. . . . .	61
3.9	The particular stacking of the 15R polytype requires the creation of a partial dislocation on each spiral turn. . . . .	62

3.10	If the advance rate is the same for all steps of a hexagonal polygonized spiral, the length of each facet should increase continuously. . . . .	63
3.11	One possible stacking of the 4H polytype (BABC). The three top bilayers are arranged as for the cubic polytype. . . . .	64
3.12	Depending on the stacking, the diffusion rate from the corner to an A or B step might be different. Image adapted from [57]. . . . .	64
3.13	The hexagonal shape is expected for a spiral with symmetric edge diffusion barriers. For an increasing difference of this barrier the shape will pass from an irregular hexagon into a triangle. . . . .	65
3.14	DIC microscopy images of (a) a <b>Si-face</b> and (b) <b>C-face</b> crystal surface. The Si-face image was post-processed to enhance the contrast of the domains. The D indicates spiral domains while M is indicating micropipes. The diameter of the growth area is 0.7 mm. . . . .	66
3.15	Spirals are overgrown by micropipes or by domains with accumulated spirals. The AFM image (c) corresponds to the area marked by the yellow square in (b). . . . .	67
3.16	Simple 6H spirals observed on the Si-face crystal surfaces. . . . .	70
3.17	Double 6H spirals consist of two branches leaving from the centre. . . . .	71
3.18	Simple 6H spirals were only rarely observed on the C-face. . . . .	71
3.19	Most simple spirals on the C-face were identified as 15R polytype. . . . .	72
3.20	(a) The terrace width $\Lambda$ was measured on the AFM images as indicated by the white arrows. (b) The images from the DIC microscopy were used to extract the terrace width in one direction on the domain (along the white arrow). . . . .	73
3.21	Spiral profiles of simple spirals on the Si-face (open circles 25 mbar, open stars 50 mbar, open squares, 400 mbar) and of double spirals on the Si-face (open circle with dot 50 mbar, open triangle with dot 250 mbar). The curves on the C-face are obtained for simple 6H (open triangles and rhombi, 100 mbar and 400 mbar respectively) and 15R (open pentagons, 200 mbar) spirals. The solid lines are a guide for the eyes and have no physical meaning. . . . .	75
3.22	(a) When the surface diffusion length is small, the diffusion fields (red area) do not overlap. (b-c) With increasing diffusion length, the diffusion fields overlap. (d) The corresponding concentration profile to (c), <i>i.e.</i> if the surface diffusion length is larger than the terrace width. . . . .	76
3.23	If the surface diffusion length is larger than the half average terrace width, the terrace width increases due to the back stress effect. . . . .	77

## List of Figures

3.24	In the case of an Archimedean spiral the advance rate of a step segment is always the same and thus the step spacing remains constant. . . . .	77
3.25	The Ehrlich-Schwoebel barrier may be of less importance at the spiral centre (atom A) due to the stress field of the screw dislocation (1) or adatom diffusion around the centre (2). Adatoms which are not located at the centre ( <i>e.g.</i> adatom B) can only diffuse along the descending step in case of a strong ES barrier. . . . .	78
3.26	The terrace width as a function of the growth rate on the Si-face. The exponent from the power fits is -0.5 for the average of the simple spirals (filled squares), -0.27 for the maximum of the simple spirals (open triangles) and -0.17 for the maximum of the double spirals (open circles). . . . .	79
3.27	The terrace width as a function of the growth rate on the C-face. The fit of the 15R simple spirals is constant. The scale is the same as in Fig. 3.26. . . . .	81
3.28	The accuracy of the simulation is lower on (a) single than on (b) double spirals since diffusion at the centre is less important in the second case. However, outside the centre, this does not play a role. . . . .	83
3.29	Spiral shapes obtained (a) for small surface diffusion length ( $\lambda_s \ll \Lambda$ ) and (b) large diffusion length ( $\lambda_s \gg \Lambda$ ). The spiral growth is limited to a disk which corresponds to the domain size. . . . .	83
3.30	Simulated variation of the maximal terrace width $x_M$ versus the ratio of finite domain size $\rho_0$ and surface diffusion length $\lambda_s$ with supersaturation as parameter. . . . .	84
3.31	Simulated variation of the terrace width with the number of turns $N$ , with the diffusion length $\lambda_s$ as parameter. . . . .	85
3.32	(a) A 4H spiral on a C-face substrate. The top bilayer (2.5 Å) dissociated while the other bilayers remain bunched (height 7.5 Å). (b) A 6H spiral on a Si-face sample showing no dissociation. The step height is 15 Å. . . . .	86
3.33	Step profiles measured by AFM of (a) a 4H spiral, (b) a 6H micropipe and (c) a 15R spiral. Only the top bilayer dissociates and its height is always 2.5 Å. . . . .	87
3.34	The position of the dissociated bilayer is schematically illustrated for the 4H polytype. The edge of the dissociated step is observed to be around the middle of two bunched steps for all polytypes. . . . .	87

3.35	The step dissociation was observed for all polytypes (a-c), varying pressures (d-f) and deposition times (g-i). Note that all shown spirals are from different samples. . . . .	88
3.36	A dissociated spiral grown on a Lely seed. The dissociation is maintained over the whole spiral. . . . .	89
3.37	The advance rate of a step depends on the bonding configuration at the edge. Image taken from [109]. . . . .	91
3.38	X-ray diffraction pattern of a fresh and a used SiC powder. The different phases found in the diffraction pattern for SiC are not indicated individually in order to emphasize that the main difference between the powders is the SiO <sub>2</sub> content. . . . .	93
3.39	Adding SiO <sub>2</sub> powder to a used SiC powder source for the growth of a SiC crystal on the C-face results in destabilization of the steps for the (a)(b) 15R but not for the (c) 4H polytype. On the 15R polytype the bunched step decomposes into single bilayers. . . . .	94
3.40	(a) SiO <sub>2</sub> was mixed with SiC powder on top of the crucible. (b) The sample surface of SiC crystal grown on Si-face is covered by polygonized 6H spirals. (c) On the spiral surfaces islands and small triangular bilayers close to the step edges are visible. . . . .	95
3.41	Step fluctuations are only observed for single bilayers. . . . .	97
3.42	The relative position of the most dissociated steps is around 0.5 (dashed line), i.e. in the middle of a terrace. $\Lambda_r$ is the distance of the dissociated step to the rising step and $\Lambda_d$ respectively to the descending step. The green squares correspond to the 6H, the black circles to the 15R and the red triangles to the 4H polytype. . . . .	97
3.43	Distribution of the dissociated step on a terrace. The dashed line corresponds to a Gauss fit. . . . .	99
A.1	Optical arrangement of a DIC microscope in reflection mode.(1) Polarizer; (2) Nomarski prism; (3) objective lens; (4) light reflector; (5) analyzer. Image taken modified from [126]. . . . .	107
A.2	Close to the height resolution limit of the used Normaski microscope: a 6H double spiral with a step height of 7.5 Å. . . . .	108
B.1	Scheme of an AFM setup. (1) x,y and z piezo tube, (2) Cantilever and probe, (3) Laser, (4) Photodetector, (5) oscillation piezo, (6) Sample. Image taken modified from [127]. . . . .	109
C.1	Possible excitations of molecular vibrations. Image taken modified from [126]. . . . .	110
D.1	Schematic drawing of a SEM. Image taken from [129]. . . . .	112



## List of Figures

E.1	Schematic drawing of TEM. Image taken from [129]. . . . .	114
E.2	Formation of a phase contrast image by HRTEM. Image taken from [129]. . . . .	115
F.1	Schematic illustration of an X-ray diffractometer. Image taken from [126]. . . . .	116
G.1	The Laue geometry for X-ray diffraction. Image taken modified from [126]. . . . .	117
G.2	A Laue photograph of a SiC sample with the corresponding simulation.	118
R.1	Empilements des polytypes les plus communs. . . . .	145
R.2	Les surfaces des cristaux SiC non désorientés sont soit terminées par les atomes de silicium, soit par les atomes de carbone. . . . .	146
R.3	Image AFM d'une micropipe. . . . .	147
R.4	Diagramme de phase d'après [42]. . . . .	148
R.5	La vitesse de croissance est une fonction parabolique pour les sur-saturations faible. Au-dessus d'une sursaturation critique la loi est linéaire. D'après [48]. . . . .	149
R.6	Phases de croissance : (1) Préchauffage, (2) Rampe, (3) Croissance, (4) Refroidissement. . . . .	151
R.7	La croissance par PVT est limitée par le transport en phase gazeuse.	152
R.8	L'effet Ehrlich-Schwoebel est plus important sur la face carbone. . .	152
R.9	L'histogramme de la distance entre les germes les plus proches ne donne pas d'information sur la longueur de diffusion. . . . .	153
R.10	La forme de la spirale dépend du polytype. . . . .	154
R.11	La loi de croissance dépend de la polarité de germe et de type de spirale. . . . .	156
R.12	Spirale dissocié de polytype 15R sur la face carbone. . . . .	157
R.13	Position de la marche dissociée. . . . .	158

# List of Tables

1.1	Electrical properties of certain SiC polytypes [16][27][28]. . . . .	8
1.2	Most common notations for certain SiC polytypes. . . . .	10
1.3	Crystallographic properties of certain SiC polytypes [16]. . . . .	12
3.1	The exponent $n$ for the different growth relations. . . . .	80
C.1	Raman shifts of various SiC polytypes. Table taken from [128]. . . .	111



# Résumé français

## Introduction

Les semi-conducteurs sont des éléments essentiels d'une multitude de produits dans la vie de tous les jours. La technologie moderne, par exemple les ordinateurs ou les smartphones, seraient inimaginables sans puces très performantes et poussées qui reposent sur les semi-conducteurs. Le silicium est, sans aucun doute, le semi-conducteur le plus répandu actuellement. L'avantage du silicium est que le procédé de croissance et ses caractéristiques sont bien connus. Un autre avantage du silicium est son abondance et le fait qu'il possède un oxyde naturel avec des propriétés exceptionnelles. De plus, il est possible de fabriquer des substrats de grand diamètre et de haute qualité à bas coût. Cependant le silicium n'est pas toujours le meilleur semi-conducteur, notamment pour l'électronique à haute température et haute puissance pour laquelle on peut préférer des semi-conducteurs avec une bande interdite large, par exemple le carbure de silicium (SiC).

A l'inverse du silicium, la croissance de cristaux de SiC ayant un grand diamètre, une faible densité de défaut et une bonne qualité cristalline est encore un défi. Dans ce contexte on peut, par exemple, mentionner la stabilité de polytypes qui est difficile à contrôler. Bien qu'il y ait et qu'il y eût des efforts et progrès énormes dans l'amélioration du procédé de croissance, par exemple la réduction des défauts de type « micropipe », la connaissance des processus fondamentaux pendant la croissance est faible. Pourtant, ces processus pourraient être la clé pour améliorer

la qualité des cristaux de SiC.

L'objectif de cette thèse est de comprendre les mécanismes fondamentaux qui se déroulent pendant la croissance de cristaux de SiC non désorientés à partir de la phase gazeuse. La croissance procède par l'incorporation des adatoms aux spirales qui recouvrent la surface. F.C. Frank est la première personne qui a proposé l'existence de spirales sur la surface en 1949, pour expliquer la vitesse de croissance étonnamment élevée pour les sursaturations faibles. Peu après, l'existence de spirales était confirmée pour plusieurs minéraux, dont le SiC. Burton, Cabrera et Frank ont été les premiers à établir des équations pour la croissance de spirales et leur théorie, qui s'appelle aujourd'hui la théorie de BCF, est encore essentielle pour la recherche dans le domaine des spirales de croissance. Néanmoins, il y a eu plusieurs affinements de cette théorie fondamentale. Cabrera et Levine, par exemple, ont déterminé la largeur de marche de façon plus exacte que Burton, Cabrera and Frank. Un autre affinement a été l'introduction de l'effet « back-stress » qui prend en compte le fait que les champs de diffusion peuvent se chevaucher.

Après que Frank ait publié ses idées sur la croissance de spirales, la recherche dans ce domaine est devenue très populaire. Le nombre de publications par année sur les spirales a atteint son maximum pendant les années cinquante, suivi par une diminution continue. A présent, le nombre de publications par an est faible bien qu'il y ait encore beaucoup de questions non résolues concernant la croissance de spirales. L'invention du microscope à force atomique et du microscope à effet tunnel dans les années quatre-vingt a donné un moyen d'analyser les surfaces de matériaux en détail. De plus, l'augmentation de la performance des ordinateurs pendant les dernières décennies permet de simuler même sans superordinateur. La combinaison de ces deux acquis, la caractérisation de surface en détail et la simulation de ces résultats expérimentaux, permet de comprendre les processus fondamentaux concernant la surface de cristaux pendant la croissance, comme Redinger *et al.* le firent pour les barrières d'énergie associées aux marches de spirales

et d'autres formes de surfaces à marches, telles que des tertres [8]. Dans d'autres publications les auteurs se focalisent soit sur les simulations soit sur les expériences de la croissance de spirales.

Dans le Laboratoire des matériaux et du génie physique, nous avons la chance de pouvoir fabriquer et caractériser nos cristaux. De plus, les programmes de simulation créés dans notre laboratoire nous permettent d'aborder les mécanismes de croissance à la surface du SiC.

Le présent travail est organisé en trois chapitres. Dans le premier chapitre, nous donnons un historique du SiC et quelques exemples d'applications. Ensuite, les propriétés spécifiques du SiC, comme le polytypisme et les défauts, sont discutés en détail. De plus, la théorie de Burton, Cabrera et Frank est introduite et les équations nécessaires pour les discussions suivantes sont démontrées. Ces équations associent la vitesse de croissance des cristaux à la largeur de marche des spirales et la sursaturation.

Le deuxième chapitre porte sur la description du réacteur de croissance et les expériences précédentes liées à la croissance du SiC non désorienté. De plus, les paramètres de croissance et les procédures de caractérisation sont expliqués. Les résultats fondamentaux pour l'analyse de spirales sont présentés dans le chapitre suivant. Le processus contrôlant la croissance de cristaux, qui est soit le transport en phase gazeuse soit la diffusion et incorporation à la surface, est déterminé. Ensuite, la nucléation fortuite sur les marches de spirales est analysée.

Le troisième chapitre est dédié à la croissance de spirales sur le SiC. Dans la première section les différents types de spirales sont discutés. Le mode de croissance de spirales simple et double est analysé en détail. Des informations supplémentaires sur les mécanismes de croissance sont obtenues à partir de profils de spirales correspondant à des simulations numériques. La variation de largeur de marche en fonction de la vitesse de croissance, et par conséquent la sursaturation, est aussi étudiée, dans le cas du SiC, pour la première fois. La dernière partie de ce chapitre

montre une nouvelle structure pour les marches de spirales. Nous allons montrer que les marches d'une spirale peuvent se dissocier dans des conditions spécifiques. L'origine de cette dissociation est discutée.

Enfin, les résultats de cette thèse sont récapitulés avant de conclure, et quelques propositions pour les futurs travaux de recherche sont données.

## **Chapitre 1**

### **Histoire**

Jöns Jacob Berzelius a probablement été la première personne capable de synthétiser le carbure de silicium (SiC) en 1824. Le procédé pour fabriquer le SiC a été amélioré par Edward Goodrich Acheson en 1890, ce qui lui a permis de pouvoir produire du SiC en grande quantité. Baumhauer découvrit en 1912 qu'il y a une multitude de structures pour le SiC, et il appela cette variété de structures polytypisme. En 1955 J.A. Lely développa une méthode pour faire des cristaux de SiC de haute qualité. Cette percée en croissance du SiC permit de l'utiliser pour des applications électroniques. Ensuite, Tairov et Tsetkov modifièrent la méthode de Lely pour obtenir un meilleur rendement.

### **Utilisation du SiC**

Grace à sa dureté, le SiC est utilisé comme abrasif mais aussi dans les gilets pare-balles. Dans cette section nous nous focalisons sur les applications électroniques. Bien que le silicium soit le semiconducteur le plus utilisé et le mieux optimisé, il y a des applications pour lesquelles il n'est pas le mieux qualifié. En effet, la concentration de porteurs est plus faible pour le SiC et c'est pourquoi il peut opérer aux températures élevées, contrairement au silicium. De plus, le SiC est intéressant

pour les électroniques de haute puissance et de haute fréquence (fort champ de claquage et vitesse de saturation élevée).

## Polytypisme et cristallographie

Le SiC est composé de tétraèdres qui partagent leurs sommets. En principe, deux configurations inéquivalentes sont possibles pour ces tétraèdres et, par conséquent, une large variété d'empilements et de mailles peuvent se former. Baumhauer introduisit le terme polytypisme pour ce phénomène. Les propriétés physiques et cristallographiques sont influencées par le polytypisme. La bande interdite, par exemple, peut varier entre 2.3 eV pour le 3C et 3.2 eV pour le 4H.

La multitude de polytypes exige une notation pour les distinguer. La notation plus populaire aujourd'hui est celle de Ramsdell. Dans la direction de l'axe  $c$  du cristal, il y a une succession de bicouches de silicium et de carbone. Le premier chiffre de la notation Ramsdell indique le nombre de bicouches dans la maille et la lettre suivante la symétrie du cristal. Cette lettre est soit C (cubique), soit H (hexagonale), soit R (rhomboédrique). Les polytypes les plus communs sont le 3C, 4H, 6H et 15R (figure R.1).

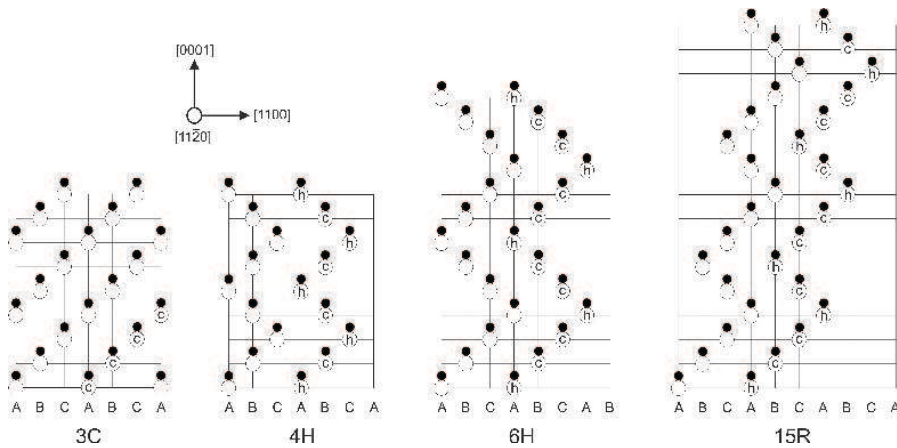


**Figure R.1:** Empilements des polytypes les plus communs.



## Résumé français

A cause de l'électronégativité différente entre le silicium (1.90 eV) et le carbone (2.55 eV), il y a une polarité dans le cristal. La surface d'un cristal non désorienté est soit terminée par les atomes Si soit par les atomes C, et par conséquent l'énergie de surface varie (figure R.2).

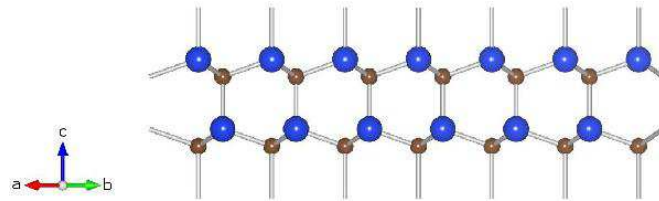


**Figure R.2:** Les surfaces des cristaux SiC non désorientés sont soit terminées par les atomes de silicium, soit par les atomes de carbone.

## Défauts

Les défauts les plus conséquents dans le SiC sont les dislocations. On distingue trois types de dislocations parfaites. Une dislocation coin est créée si un demi-plan d'atome est enlevé ou ajouté. La dislocation vis peut se former si une partie du cristal glisse. Le troisième type est la dislocation mixte qui comprend une composante coin et une composante vis. Le vecteur de Burgers de ces dislocations est toujours un multiple entier du vecteur de maille le plus court. En plus des dislocations parfaites, il existe aussi les dislocations partielles qui peuvent créer des fautes d'empilement. Si le vecteur Burgers est plus large que la constante de réseau  $c$ , un trou se forme au centre de la dislocation à cause d'un excès d'énergie élastique. On appelle ce défaut « micropipe » (figure R.3). Grâce au développement conséquent de la technique de croissance du SiC, les micropipes ne posent plus de problème aujourd'hui.

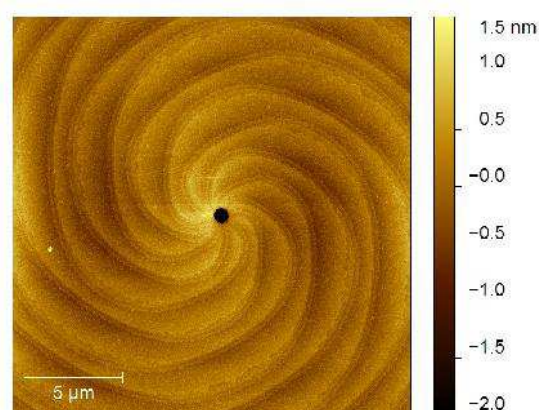


**Figure R.3:** Image AFM d'une micropipe.

## Diagrammes de phases du SiC

Le diagramme de phases montre qu'il n'existe pas de liquide congruent de SiC (figure R.4). Au-dessus de  $2680^{\circ}\text{C}$ , le SiC se décompose en graphite et en une phase gazeuse. C'est pourquoi la croissance à partir de la phase gazeuse est la méthode préférentielle.

D'autres diagrammes montrent que les polytypes apparaissent dans une gamme de température définie. Cependant, ces gammes se croisent, et plusieurs polytypes peuvent se former à une température donnée. De plus, le polytype qui se forme pendant la croissance dépend d'autres paramètres, par exemple la polarité du substrat et son polytype, la sursaturation et les impuretés.

## Transport physique en phase vapeur (« Physical vapour transport »)

La méthode Lely modifiée, aussi appelée « physical vapour transport technique » (PVT, transport physique en phase vapeur), est la méthode la plus répandue dans l'industrie aujourd'hui. Un creuset qui contient de la poudre SiC est chauffé au-delà

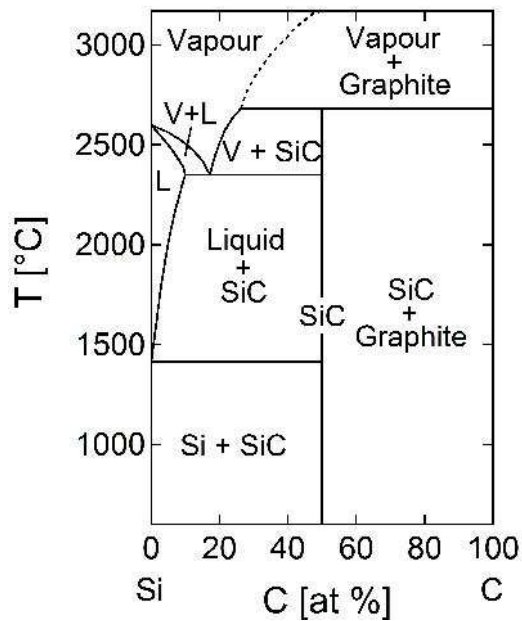


Figure R.4: Diagramme de phase d'après [42].

de 1800°C. La poudre se sublime et, à cause d'un gradient de température, les atomes et molécules gazeuses diffusent vers le substrat, où ils sont incorporés dans le cristal.

## La théorie de Burton, Cabrera et Frank

En 1949 Frank proposa que la croissance des cristaux se fasse par l'incorporation des adatoms aux marches des dislocations vis qui forment ainsi des spirales de croissance. Deux ans plus tard, Burton, Cabrera et Frank (BCF) établirent des équations de la vitesse de croissance en fonction de la sursaturation, ou de la largeur de marche. Dans cette thèse une approche simplifiée est utilisé pour obtenir les équations clé.

Tout d'abord les flux arrivant et sortant d'un segment sur la surface du cristal sont considérés en association avec la première loi de Fick. La solution de cette équation différentielle donne la concentration des adatoms à la surface. Ensuite, le flux net

vers une marche est obtenu en considérant la concentration de surface précédemment établie. Du fait de la courbure d'une marche spirale, l'effet Gibbs-Thomson est pris en compte pour corriger le flux net.

L'avancée d'une marche et aussi la vitesse de croissance est proportionnelle à ce flux. Si la longueur de diffusion à la surface est très inférieure à la largeur de marche on trouve une dépendance parabolique pour la vitesse de croissance en fonction de la sursaturation. Dans le deuxième cas, c'est-à-dire lorsque la longueur de diffusion est plus large que la largeur de marche, la loi est linéaire (figure R.5).

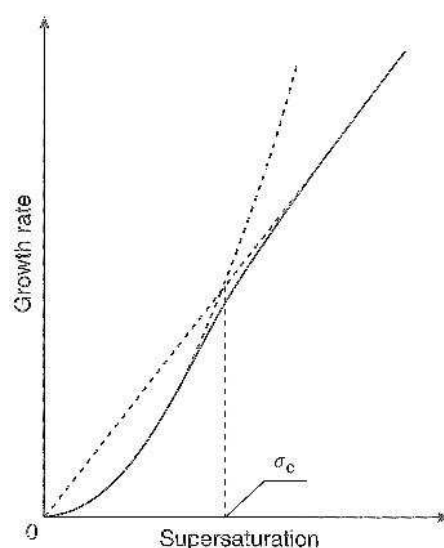


**Figure R.5:** La vitesse de croissance est une fonction parabolique pour les sursaturations faible. Au-dessus d'une sursaturation critique la loi est linéaire. D'après [48].

## **Chapitre 2**

### **Paramètres expérimentaux et conditions de croissance**

Nous avons utilisé un réacteur PVT pour la croissance des cristaux du SiC. Souvent, le substrat est collé sur un support en graphite mais dans notre réacteur le support employé peut porter le substrat sans colle. Grâce à cette méthode, on peut éviter la formation de contraintes dans le substrat due aux coefficients de dilatation thermique différents entre le support et substrat. De plus, il y a plusieurs autres bénéfices, par exemple on peut réutiliser les pièces de graphite.

Les substrats 6H et 4H « epi-ready » polis par Novasic et coupés en carrés de 0.9 mm sont utilisés pour la croissance. La densité de dislocations et micropipes, déterminée par une attaque KOH, était entre  $2.9 \cdot 10^4$  et  $3.1 \cdot 10^4 \text{ cm}^{-2}$ .

On peut différencier quatre phases pendant la croissance (figure R.6). La puissance du chauffage inductif est réglée manuellement jusqu' à 1000°C. A partir de cette température, le pyromètre peut mesurer la température. La pression est réglée au moins à 250 mbar, puis le réacteur est chauffé jusqu' à 2100°C par une rampe de 7.5°C/min. A 2100°C, la pression de croissance est réglée. La durée de la croissance varie entre 30 min et 5 h, selon la pression utilisée. Après cette phase de croissance, la pression est encore augmentée, et le réacteur de chauffage inductif est arrêté.

Les échantillons sont caractérisés par un microscope optique Leica DM LM et un microscope à contraste interférentiel Zeiss Axioskop 40 pour cartographier la surface et trouver des spirales. Ces spirales sont visualisées par un microscope à force atomique Veeco dimension 3100 en mode tapping ou contact. Le polytype des spirales est vérifié par un spectromètre Raman Jobin-Yvon/Horiba LabRam à 514 nm. L'épaisseur des échantillons est mesurée pour déterminer la vitesse de croissance. Des caractérisations supplémentaires, par exemple par un microscope électronique à balayage, sont effectuées dans certains cas.

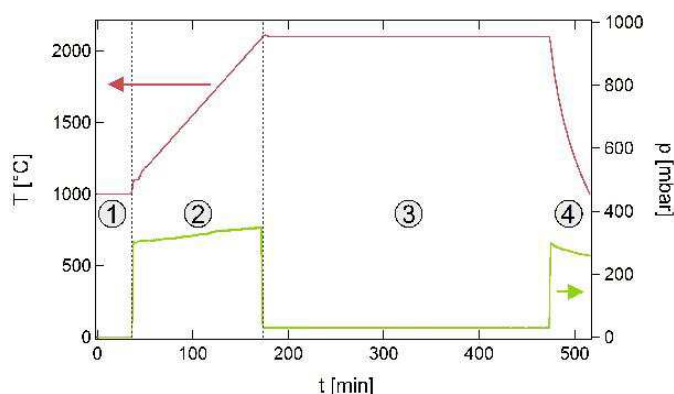


**Figure R.6:** Phases de croissance : (1) Préchauffage, (2) Rampe, (3) Croissance, (4) Refroidissement.

## Processus limitant de la vitesse de croissance

Deux processus peuvent limiter la vitesse de croissance. La sublimation de la poudre SiC et le transport en phase gazeuse est le premier processus. Le deuxième est la diffusion des adatoms à la surface du cristal et leur incorporation.

Nous avons observé la vitesse de croissance en fonction de la pression de croissance pour trouver le processus limitant. La vitesse de croissance est presque inversement proportionnelle à la pression pour la face silicium et la face carbone (figure R.7). Le processus limitant est, par conséquent, le transport en phase gazeuse. De plus, il y a un flux advectif qui influence la loi observée.

## Formation de germes

La formation de germes a été observée occasionnellement sur les cristaux. La hauteur de germes est normalement de  $2.5 \text{ \AA}$ , mais dans certains cas les germes sont assez larges pour que d'autres germes se forment sur les germes déjà existants.

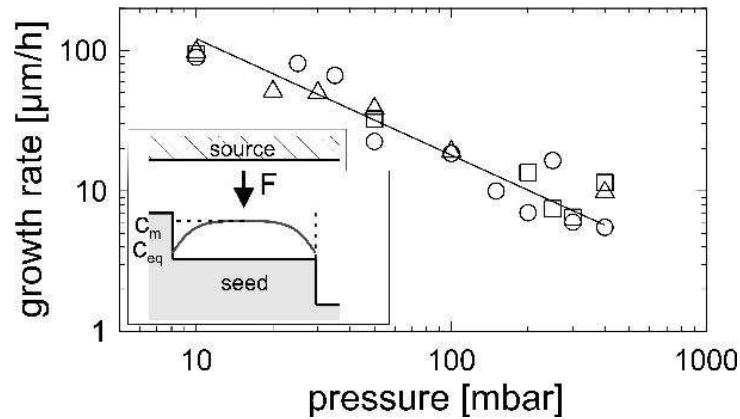


**Figure R.7:** La croissance par PVT est limitée par le transport en phase gazeuse.

Nous avons tracé le nombre de germes en fonction de leur position sur les marches (figure R.8). Sur la face silicium, le nombre de germes est faible aux extrémités des marches et constant entre les deux. Par contre, sur la face carbone, le nombre de germes est faible aux abords de la marche croissante et très large vers la marche décroissante. Entre les deux marches, le nombre est constant. En conséquence, il y a une barrière d'Ehrlich-Schwoebel uniquement sur la face carbone. Toutefois, des germes sur d'autres échantillons suggèrent qu'on peut aussi trouver cette barrière sur la face silicium, mais avec une énergie plus faible.

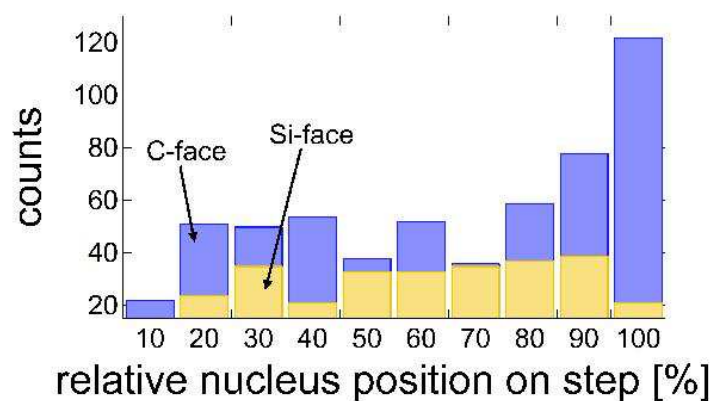


**Figure R.8:** L'effet Ehrlich-Schwoebel est plus important sur la face carbone.

On ne peut pas estimer la longueur de diffusion à la surface à partir de la

distance entre les germes, pour les cristaux fait par PVT, à cause de la désorption des adatoms (figure R.9). Une autre méthode communiquée dans la littérature est de mesurer l'avancée de bord d'un germe. Toutefois, la vitesse de croissance en mode PVT est trop large pour appliquer cette méthode.

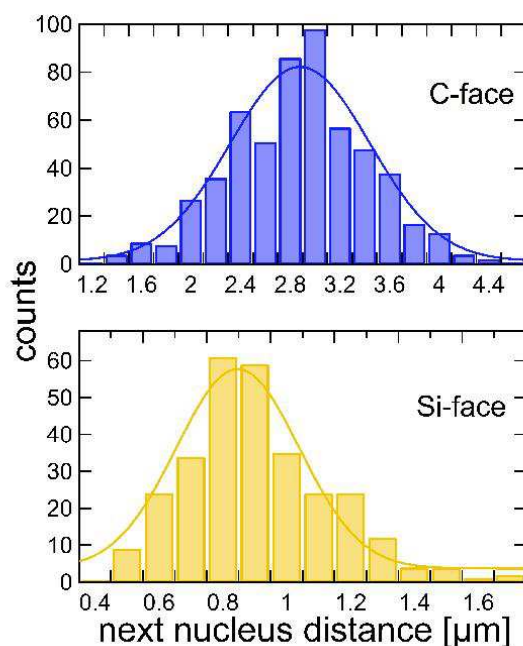


**Figure R.9:** L'histogramme de la distance entre les germes les plus proches ne donne pas d'information sur la longueur de diffusion.

## Chapitre 3

### Spirales observées

Sur nos échantillons, nous avons observé plusieurs types de spirales. Les plus importants pour l'analyse dans ce chapitre sont les spirales simple et double. Une spirale simple a une branche dont la hauteur correspond au paramètre de maille  $c$ , ou  $c/3$  dans le cas d'une spirale 15R. Les spirales doubles ont toujours deux



### Résumé français

branches et la hauteur d'une branche est  $7.5 \text{ \AA}$ , c'est-à-dire que les deux branches correspondent au paramètre de maille  $c$  de  $6H$ . On parle de spirale s'il n'y a pas de trou au centre, autrement il s'agit d'une « micropipe ». Souvent les spirales n'existent pas isolées mais mélangées.

Nous avons discuté les origines possibles de la polygonisation de spirales. Dans notre cas la polygonisation dépend de la hauteur de marche et du polytype (figure R.10). La forme de spirales  $15R$  correspond toujours à celle d'une spirale ronde, c'est-à-dire qu'elles ne sont pas polygonisées. L'empilement particulier du  $15R$  demande la création d'une dislocation partielle toutes les cinq bicouches. Nous supposons que cette dislocation influence l'énergie spécifique de marche et par conséquent la forme de la spirale.

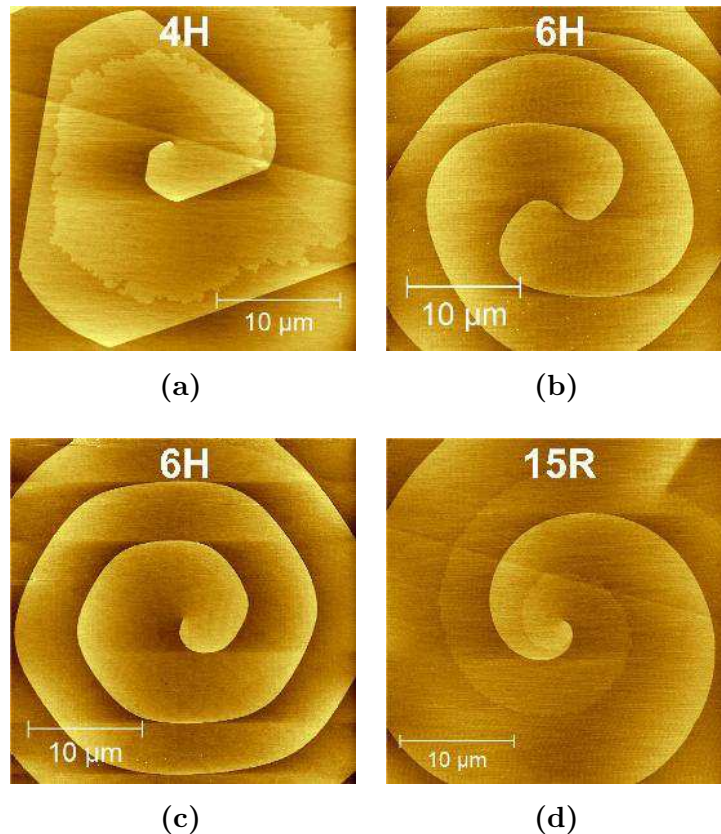


**Figure R.10:** La forme de la spirale dépend du polytype.

Pendant la croissance des cristaux de SiC nous avons observé que les micropipes recouvrent les spirales. La modification de la loi BCF montre que la vitesse de croissance d'une micropipe augmente avec le nombre de branches. Pour cette raison, il est nécessaire de limiter le temps de croissance, sinon on n'est plus capable d'observer des spirales simples.

## **Mode de croissance des spirales**

L'accès aux paramètres de croissance est limité quand on utilise la méthode PVT pour la croissance de SiC. Les seuls paramètres influençables sont la température, la pression et la géométrie du creuset. La sursaturation, qui contrôle la croissance, n'est pas accessible.

Cependant, il est possible d'estimer la sursaturation relative entre différents échantillons par l'analyse de la vitesse de croissance et la largeur de marche de spirales. De plus, on peut déterminer la loi de croissance.

Nous avons mesuré la vitesse de croissance et la largeur de marche de spirales simple et double sur la face silicium et face carbone (figure R.11). Les spirales simples sur la face silicium suivent bien la loi de BCF. La loi trouvée pour les spirales doubles sur la face carbone n'est pas la même. A cause de la vitesse anisotrope de marche, la distance entre les deux branches est plus petite que la longueur de diffusion à la surface. Les champs de diffusion peuvent se chevaucher et c'est pourquoi les spirales suivent la loi de « back stress ». Sur la face carbone, la largeur de marche en fonction de la vitesse de croissance reste toujours constante. Nous supposons que la taille de domaine limitée, l'effet back stress et une barrière Ehrlich-Schwoebel très large sont responsables de l'invariance de la largeur de marche.

Nous avons aussi analysé la variation de largeur de marche en fonction de la distance au centre. Cette analyse a suggéré que l'incorporation des adatoms au

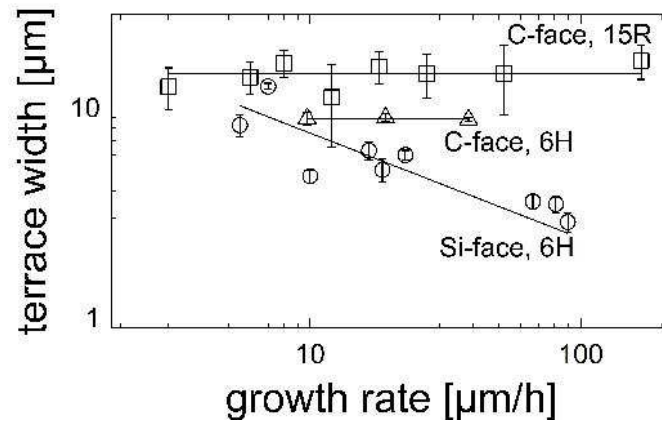


**Figure R.11:** La loi de croissance dépend de la polarité de germe et de type de spirale.

centre est probablement modifiée par le champ de contrainte de la dislocation vis. Sur la face carbone notre simulation a montré que la largeur de marche est fortement influencée par la taille du domaine.

## La dissociation de marche de spirales

Pendant la croissance de SiC, nous avons observé que la bicouche supérieure d'une marche de spirale unitaire peut se dissocier pour des paramètres de croissance spécifiques (figure R.12). Cette dissociation n'a pas encore été rapportée dans la littérature.

Nous avons observé la dissociation quand nous avons utilisé une poudre de SiC neuve et en même temps un substrat face carbone non désorienté. La bicouche dissociée se retrouve au centre d'une terrasse et la position ne change pas lorsqu'on est loin du centre. Dans la littérature il y a des publications sur l'observation de bicouche seule sur les substrats d'orientation vicinale et la formation de ces bicouches est expliquée par l'orientation des marches suivant des directions particulières. Dans notre cas, l'orientation de marche change en continu et c'est pourquoi les résultats

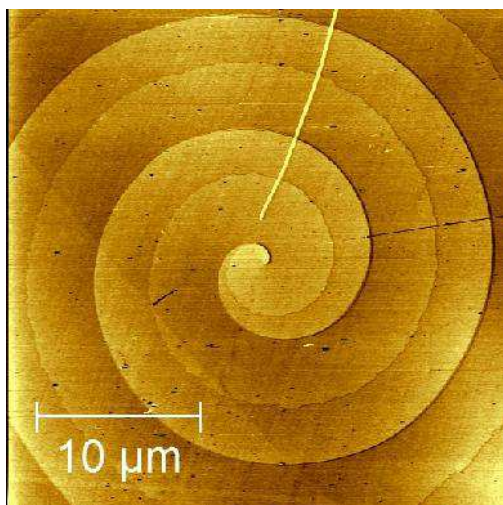


**Figure R.12:** Spirale dissocié de polytype 15R sur la face carbone.

des substrats vicinaux de la littérature ne sont pas transférables aux marches de spirales. Nous supposons que la dissociation est liée à la silice contenue dans la poudre neuve. La dissociation est probablement causée soit par l'incorporation d'adatoms, soit par le rapport C/Si modifié par la silice dans la phase gazeuse. De plus, la contrainte de dislocation vis pourrait faciliter la dissociation au centre de la spirale.

Nous supposons que les interactions élastiques entre les marches contraignent probablement la position de la bicouche dissocié au centre des terrasses (figure R.13).

Sur les images AFM nous avons observé des fluctuations prononcées pour les bicouches seules. Par contre, il n'y a pas de fluctuation pour les marches d'une hauteur de plus de deux bicouches. Pour le silicium il est connu que la rigidité d'une marche augmente avec sa hauteur. Nos observations montrent que la rigidité augmente aussi avec la hauteur de marche pour le SiC.

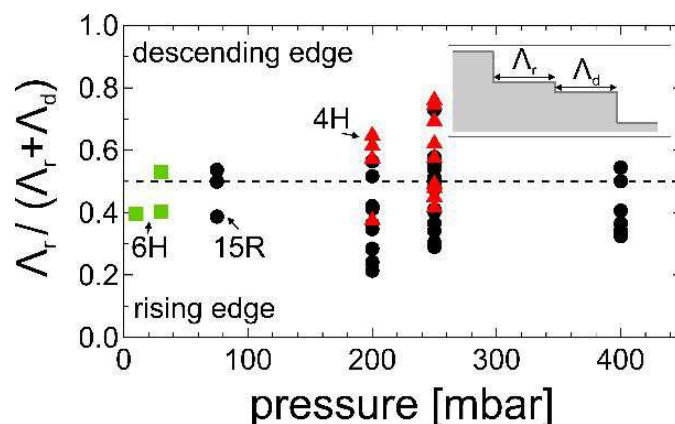


**Figure R.13:** Position de la marche dissociée.

## Conclusion

Dans cette thèse nous avons étudié la croissance de cristaux de SiC non désorientés. La caractérisation de surface des cristaux fabriqués par PVT et les simulations complémentaires donnent un nouvel aperçu des mécanismes de croissance.

Nous avons constaté que la croissance du SiC par PVT est limitée par le transport en phase gazeuse plutôt que par la diffusion en surface et l'incorporation des adatoms. Par conséquent, la densité de défauts est assez grande pour que la vitesse de croissance ne soit pas limitée par les mécanismes de surface.

La nucléation a été observée occasionnellement sur la face silicium et la face carbone. L'analyse de germes a démontré que l'effet Ehrlich-Schwoebel est plus important sur la face carbone que sur la face silicium. Grâce à l'étude de la distribution de ces germes nous avons pu conclure que la longueur de diffusion sur la face carbone est plus grande qu'une demi-largeur de marche ( $\lambda_s > 3.12 \mu\text{m}$ ) pour les paramètres de croissance utilisés. Sur la face silicium, au contraire, nous avons trouvé que la longueur de diffusion est plus petite que la demi-largeur de marche ( $\lambda_s < 3.28 \mu\text{m}$ ). Bien que nous n'ayons pas trouvé la valeur exacte de la longueur de diffusion, l'ordre de grandeur déterminé peut être utile pour les simulations et expliquer divers résultats.

Nous avons étudié les modes de croissance de spirales du SiC sur la face silicium et face carbone en fonction de la sursaturation, ce qui n'avait jamais été fait de manière systématique et pour les deux faces. Les résultats expérimentaux montrent que le mode de croissance dépend non seulement de la polarité du germe mais aussi du type de spirale. Les spirales simples sur la face silicium suivent parfaitement la loi de BCF alors que le mode de croissance est différent pour les spirales doubles sur la même face à cause de l'effet « back stress ». Les largeurs de marches sont plus petites pour ces spirales et c'est pourquoi les champs de diffusion se chevauchent et la loi de croissance en spirale est modifiée.

Sur la face carbone, la largeur de marche reste constante pour toutes les vitesses de croissance. C'est la première fois qu'une telle indépendance est observée pour des spirales n'étant pas des « micropipes », c'est-à-dire pour les spirales sans trou au centre. Les simulations suggèrent qu'une taille de domaine limité, un effet Ehrlich-Schwoebel fort et l'effet « back stress » réduisent la dépendance de la largeur de marche par rapport à la vitesse de croissance. Toutefois, selon les simulations, la largeur de marche n'est pas totalement indépendante de la sursaturation, et par conséquent de la vitesse de croissance. C'est pourquoi les simulations ne peuvent pas expliquer complètement nos résultats expérimentaux.

L'analyse de la largeur de marche de spirales en fonction de la vitesse de croissance ne donne pas accès à la sursaturation dans le réacteur. Cependant, les résultats sur la face silicium montrent que la vitesse de croissance augmente avec la sursaturation. Pour cette raison nous pourrions déterminer pour quel échantillon la sursaturation est plus grande en comparant les largeurs de marches.

Enfin, nous avons observé une nouvelle dissociation de marches de spirales en une bicouche et une marche de bicouches regroupées en paquet. Cette dissociation est obtenue quand on utilise une poudre neuve et un germe face carbone. L'origine de cette dissociation n'est pas encore comprise mais nous supposons que l'incorporation des impuretés joue un rôle très important. Nous supposons que la position de la

## *Résumé français*

marche dissociée est restreinte au centre d'une terrasse par les forces élastiques entre les marches.

Nos études ont révélé de nouveaux mécanismes de la croissance de spirales sur le SiC. Pourtant, nous ne pouvons pas encore expliquer tous les phénomènes observés de manière satisfaisante. Nos résultats ouvrent donc des perspectives intéressantes de travail théorique.

L'indépendance de la largeur de marches par rapport à la sursaturation sur la face carbone demande une étude approfondie. Nos simulations ont montré que la taille de domaine influe fortement sur la largeur de marche. Si on choisissait seulement des spirales isolées sur un domaine très large, on pourrait probablement encore mieux vérifier si la largeur de marche est vraiment indépendante de la sursaturation.

Un autre sujet non résolu est l'origine de la dissociation. Les résultats expérimentaux suggèrent que la silice présente dans la poudre joue un rôle important pour ce phénomène. Pour vérifier cette supposition on pourrait mélanger la poudre utilisée avec des fractions de plus en plus importantes de silice. La dissociation devrait devenir observable pour une certaine fraction de silice si notre supposition est pertinente. De plus, il serait intéressant de vérifier si toutes les marches peuvent être dissociées lors de l'augmentation de la fraction de silice.

Des simulations pourraient par ailleurs montrer quantitativement si les forces élastiques entre les marches restreignent bien la position des bicouches uniques dissociées au centre des terrasses formées entre deux marches constituées de regroupements de bicouches.





## Abstract

Silicon carbide is a promising semiconductor for high temperature and power electronics. Its growth process has been refined continuously in the last years but there is still little knowledge on the surface processes taking place during growth. This thesis is dealing with these processes by analysing the initial growth of on-axis crystals.

The growth rate limiting step of the physical vapour transport technique is determined. The study of nuclei occasionally observed gives insight on the present Ehrlich-Schwoebel barriers and allows furthermore to estimate the order of magnitude of the surface diffusion length.

For the first time the growth laws of spirals on both Si- and C- face SiC surfaces are systematically analysed. Simulations are performed in order to check the influence of a limited domain size and overlapping diffusion fields on the spiral shapes and growth laws.

A novel spiral step structure is observed on C-face spirals. The top bilayer dissociates under certain and reproducible conditions. The experimental parameters are reported and further analysis of this new step structure is performed.

## Résumé

Le carbure de silicium est un semi-conducteur prometteur pour les applications en électronique haute température et haute puissance. La croissance de SiC a été améliorée continuellement pendant les dernières années mais la connaissance des processus à la surface pendant la croissance est encore faible. Dans cette thèse ces processus sont étudiés par l'analyse de la croissance initiale de cristaux non désorientés.

Le processus qui limite la vitesse de croissance est déterminé. L'étude des germes observés occasionnellement permet d'avoir un aperçu des barrières Ehrlich-Schwoebel existantes et, de plus, d'estimer l'ordre de grandeur de la longueur de diffusion à la surface.

Pour la première fois les lois de croissance de spirales sont systématiquement analysées sur la face silicium et la face carbone du SiC. L'influence d'un domaine limité et du chevauchement de champs de diffusion sur la forme des spirales et les lois de croissance est analysée par des simulations.

Sur les spirales de la face carbone, une nouvelle structure de marches est observée. La bicouche supérieure se dissocie à certaines conditions définies et reproductibles. Les conditions expérimentales sont clairement identifiées et une analyse de cette nouvelle structure est effectuée.